Charm Production in Diffractive Deep-Inelastic Scattering at HERA

Benedict Waugh

1997

A thesis submitted to the University of Manchester for the degree of Doctor of Philosophy in the Department of Physics and Astronomy in the Faculty of Science.

Contents

Abstract

A measurement of the cross section for production of the charmed $D^{*\pm}$ meson in diffractive deep-inelastic e^+p interactions is presented. The measurement was made using data recorded by the H1 experiment at HERA in 1994 during collisions between protons at an energy of 820 GeV and positrons at 27.5 GeV. The cross section is found to be significantly larger than the prediction of a model in which the diffractive exchange is a quark-dominated object, and favours a model in which the momentum of the exchange is carried largely by gluons.

The prospects for more detailed investigation of diffractive deep-inelastic charm production, using the detector upgrades and larger integrated luminosities planned for the future, are discussed. A Monte Carlo simulation is used to explore the possibility of measuring the diffractive charm structure function $F_2^{D(3)c}$.

No portion of the work referred to in this thesis has been submitted in support of an application for another degree or qualification of this or any other university or other institute of learning.

Chapter 1

Introduction

Since the end of the 1960s, deep-inelastic scattering of leptons on stationary targets has been of great importance in elucidating the structure of the proton and neutron. The point-like electron or muon serves as a 'clean' probe, the final state being easier to interpret than that resulting from a hadron-hadron collision. Successive generations of accelerators have provided lepton beams at higher and higher energies, allowing smaller and smaller scales to be probed, but the attainable energy has been limited by the problem of energy loss through synchrotron radiation. The *ep* collider HERA, which began running in 1992, sidesteps this difficulty by using a high-momentum beam of protons instead of a stationary target. The result is a leap of an order of magnitude in centre-of-mass energy, increasing the accessible Q^2 by approximately two orders of magnitude and pushing the lower limit in x down by a similar factor.

One surprising feature of the HERA data is the existence of a significant fraction of deep-inelastic events in which there is a large angle between the proton remnant and the nearest particle – a *rapidity gap*. These events are termed *diffractive*, and seem to be related to similar processes which occur in photoproduction and have been observed in hadron-hadron interactions for some time. The presence of a gap indicates that a colourless object is exchanged, so there is no string of colour flux linking the two parts of the hadronic final state. These exchanges are successfully described in hadron-hadron interactions by Regge theory, according to which the dominant effect at high energies is exchange of the *pomeron* – an object with the quantum numbers of the vacuum. Despite the success of Regge theory, and its application to total cross sections and hence to the rise of F_2 at small x, there is no clear picture of how the pomeron arises from QCD, the fundamental theory

of strong interactions. Diffractive deep-inelastic scattering offers a way of clarifying the situation by probing the partonic structure of the exchanged object.

It is interesting to look at the gluon content of the pomeron, especially as several of the proposed QCD-based models of the pomeron suggest that its structure is dominated by gluons, and there has already been some support from experimental results for this idea. One process sensitive to the gluon content is the production of heavy quarks, such as charm. This is investigated in this thesis by using the decay chain $D^{*+} \to D^0\pi^+ \to (K^-\pi^+)\pi^+$ to tag charm quarks. The limited statistics available in the data from 1994 allow only an accuracy of about 50% on the cross section for $D^{*\pm}$ production, but this is sufficient to rule out a pomeron consisting only of quarks.

In chapter 2, an overview is given of the physics processes occurring in ep collisions at HERA, and of the ways in which proton structure is investigated. Chapter 3 discusses diffractive interactions in more detail. Chapter 4 describes the H1 detector, concentrating on the parts that are particularly relevant to this analysis. The selection of diffractive deep-inelastic events is described in chapter 5, and the measurement of the cross section for the production of $D^{*\pm}$ mesons in such events is described in chapter 6. Chapter 7 discusses the prospects for future measurements of diffractive deep-inelastic charm production using the large increases in luminosity expected in the next few years of HERA running as well as the ongoing upgrades of the H1 detector.

Chapter 2

Electron-Proton Scattering at HERA

The chief purpose of the HERA accelerator is the study of the structure of the proton. This chapter gives a review of the physics of proton structure and lepton-nucleon collisions. The discussion of diffractive interactions is left to chapter 3. For a more in-depth treatment of the physics discussed in this chapter, see for example [1]. Various topics specific to HERA are also covered in [2].

The idea that hadrons – such as the proton – are composite rather than elementary particles was originally proposed as a way of making sense of the plethora of observed hadron species in terms of a simpler substructure. The quark model, in which hadrons are composed of spin-$\frac{1}{2}$ constituents (*quarks*) was proposed in 1964 by Gell-Mann [3] and, independently, by Zweig. This model developed out of the approximate SU(3) symmetry (the 'eightfold way') describing the strong interactions of the baryons and mesons known at the time.

In Gell-Mann's 1964 model, there were three varieties (*flavours*) of quark – up, down and strange (u, d and s). However, the existence of a fourth flavour – charm (c) – was predicted by Glashow, Iliopoulos and Maiani, and confirmed by the discovery in 1974 of the ψ and ψ' mesons. The unexpected discovery in 1977 of a fifth – bottom (b) – quark led in turn to the expectation of a sixth – top (t), the existence of which was confirmed in 1995 by the CDF and D0 collaborations at the Tevatron $p\bar{p}$ collider.

Although quarks were at first thought of as 'purely mathematical entities' [3], experiments on inelastic lepton-nucleon scattering from 1968 onwards pro-

vided evidence for the existence of point-like physical objects within the proton and neutron. HERA is the descendant of those early experiments and provides a much more detailed view of the structure of the proton.

2.1 Deep-Inelastic Scattering

2.1.1 Proton Structure: Structure Functions

The structure of the proton (and neutron) can be investigated using lepton-nucleon scattering. The leptons are point-like (at least up to the resolution of current measurements) and provide a useful probe of the structure of an extended object such as the proton, the final state being simpler to interpret than in a proton-proton collision, where both participating particles are extended objects.

The electron[1] interacts with the proton or one of the constituents of the proton by exchange of an electroweak vector boson – a photon or Z^0 in the neutral-current process $ep \to eX$, or a $W^{\pm}$ in the charged-current process $ep \to \nu X$. Figure 2.1(a) is a schematic diagram of an ep collision. The inclusive neutral- or charged-current process can be characterized by three kinematic quantities defined as follows:

$$s = (k+p)^2 \tag{2.1}$$

$$Q^2 = -q^2 \tag{2.2}$$

$$x = \frac{Q^2}{2p \cdot q} \tag{2.3}$$

These have the following interpretations:

- s is the square of the centre-of-mass energy of the ep system;
- Q^2 is the virtuality of the exchanged boson, and determines the length scale $\lambda \sim 1/\sqrt{Q^2}$ at which the proton is probed;
- x is a dimensionless variable; its interpretation in the quark-parton model will be mentioned later.

Other quantities also prove useful, such as

$$W^2 = (p+q)^2 \tag{2.4}$$

[1] In this thesis, references to the beam lepton as *electrons* apply also to positrons, except where otherwise stated.

$$\nu = \frac{q \cdot p}{m_p} \tag{2.5}$$

$$y = \frac{q \cdot p}{k \cdot p} \tag{2.6}$$

These variables are interpreted as follows:

- W is the centre-of-mass energy of the boson-proton system;
- ν is the energy of the boson in the rest frame of the proton;
- y is the fraction of the electron's energy carried by the boson in the rest frame of the proton.

However, only three variables are independent.

The exchange of a vector boson of mass M introduces a propagator of the form

$$\frac{1}{Q^2 + M^2} \tag{2.7}$$

into the scattering amplitude. Thus the cross section for ep scattering is dominated by low-Q^2 photon exchange. The heavier Z^0 and $W^{\pm}$ only make a significant contribution when Q^2 is around M_W^2 or larger, and charged-current interactions form only a small part of the total cross section. The rest of this chapter will concentrate largely on neutral-current processes, since detailed studies of charged-current physics will require larger integrated luminosities than have so far been achieved.

When the virtuality Q^2 of the exchanged boson is large compared to m_p^2, the proton is probed at a small scale; the boson interacts with one of the constituents of the proton rather than the whole thing. This is *deep-inelastic scattering* (DIS).

Using the single-photon approximation, in which contributions from multiple photon exchange are neglected, the cross section for the inclusive neutral-current DIS process (summed over all final states) may be expressed as

$$\frac{\mathrm{d}^2\sigma_{ep\to eX}}{\mathrm{d}x\mathrm{d}Q^2} = \frac{4\pi\alpha_{em}^2}{xQ^4}\left[xy^2F_1(x,Q^2) + (1-y)F_2(x,Q^2)\right] \tag{2.8}$$

where F_1 and F_2 are known as the *structure functions* of the proton. For spin-$\frac{1}{2}$ partons, the contribution from the exchange of longitudinally polarized photons is zero, and F_1 and F_2 are connected by the *Callan-Gross* relation

$$2xF_1 = F_2, \tag{2.9}$$

which is supported fairly well by the data. Because the structure functions describe the inclusive process, they can be measured even if only the scattered lepton is

detected, and not the hadronic final state. Although structure functions say nothing about the nature of the final state, they nevertheless provide a lot of useful information about the structure of the nucleons.

Experiments using lepton beams to measure the nucleon structure functions in DIS were first carried out in 1968 at SLAC [4, 5, 6] and DESY [7], using beams of electrons. More recently, a series of experiments – EMC [8, 9], BCDMS [10, 11] and NMC [12] – have used a beam of muons at up to 280 GeV from the CERN SPS, and a 460 GeV muon beam has been used in the E665 experiment at Fermilab [13]. In each case, a fixed target of hydrogen, deuterium or other material has been used. A much larger centre-of-mass energy is made possible by a colliding-beam experiment, and HERA has been built with the measurement of the proton structure function F_2 over an extended range in x and Q^2 as one of its main objects.

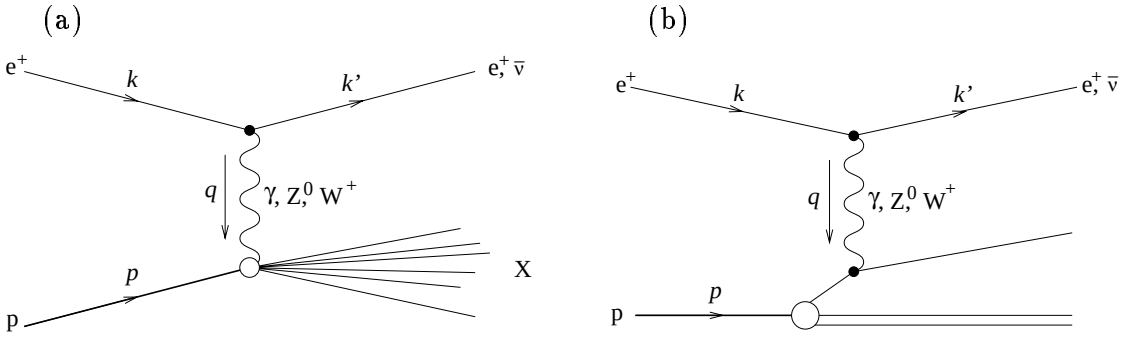

Figure 2.1: A schematic diagram of a deep-inelastic ep interaction (a) in general and (b) in the quark-parton model. The labelled arrows indicate the four-momenta of the particles.

The Quark-Parton Model

It is found that the structure function F_2 is fairly insensitive to the scale Q^2 [14], indicating that the photon is scattering from point-like objects. This scale independence is known as *Bjorken scaling* [15]. The experimental support for the Callan-Gross relation (2.9) implies that these *partons* have a spin of $\frac{1}{2}$. In the *quark-parton model* (QPM) [16, 17], proposed by Feynman, they are identified with the quarks postulated by Gell-Mann and Zweig. When probed by a highly virtual photon, the quarks behave like free objects, and DIS may be treated as the elastic scattering of electrons off quarks. In fact, quarks are never observed in their free

state, but only as bound states of several quarks, antiquarks or both (qqq, $\bar{q}\bar{q}\bar{q}$, $q\bar{q}$), i.e. hadrons. However, the hadronization process, whereby the struck quark and the proton remnant in a DIS event form the observed hadronic final state, takes place over a longer time and may be considered as independent of the underlying eq interaction. According to this model, as long as the mass of the quark can be neglected, the Bjorken variable x may be interpreted as the fraction of the proton's momentum carried by the struck quark in a frame in which the proton's momentum is infinite.

The quark-parton model relates the nucleon structure function F_2 straightforwardly to the momentum distribution of the nucleon's constituent quarks:

$$F_2(x) = \sum_q e_q^2 x f_q(x) \tag{2.10}$$

where the sum is over the quark flavours, e_q is the charge of the quark flavour q and $f_q(x)\mathrm{d}x$ is the expected number of quarks of flavour q carrying a fraction of the proton's momentum between x and $x + \mathrm{d}x$. Because the quarks are assumed to be point-like, (2.10) has no dependence on the scale Q^2. Using (2.10) and the experimental results for the structure functions F_2^p and F_2^n of the proton and neutron, and assuming the quark-model uud and udd structure of the proton and neutron respectively, the average momentum fraction x carried by each quark flavour can be calculated. It is found that the quarks only account for a total of about half of the momentum of the proton (see e.g. [8]):

$$\sum_q \langle x \rangle = \sum_q \int_0^1 x f_q(x)\mathrm{d}x = \frac{9}{5}\int_0^1 [F_2^p(x) + F_2^n(x)]\mathrm{d}x \approx 0.5. \tag{2.11}$$

Quantum Chromodynamics

If the parton model is to make sense, the rest of the momentum of the proton must be carried by neutral constituents, which do not couple to the photon and are therefore invisible to DIS. This puzzle was solved in the 1970s by the introduction of *quantum chromodynamics* (QCD), the theory of the strong interaction between quarks. The strong force is carried by gluons – neutral vector bosons that carry the 'missing' half of the momentum of the proton.

Another problem with the simple quark-parton model is the fact that the scale-invariance of F_2 is only approximate: at small values of x, F_2 increases with Q^2, while at large x it decreases. This too is explained by QCD. As Q^2 increases, the proton is probed at a smaller scale, and the radiation of gluons by quarks be-

comes important, as well as the splitting of gluons into quark-antiquark and gluon-gluon pairs (see figure 2.2). This means that at large Q^2 a large population of low-momentum (small-x) partons is seen, while the large-x valence quarks lose momentum by radiating gluons. This shift towards small x explains why F_2 falls at large x and grows at small x. The QCD-based DGLAP equations [18, 19, 20] provide a successful description of the way F_2 evolves with increasing Q^2.

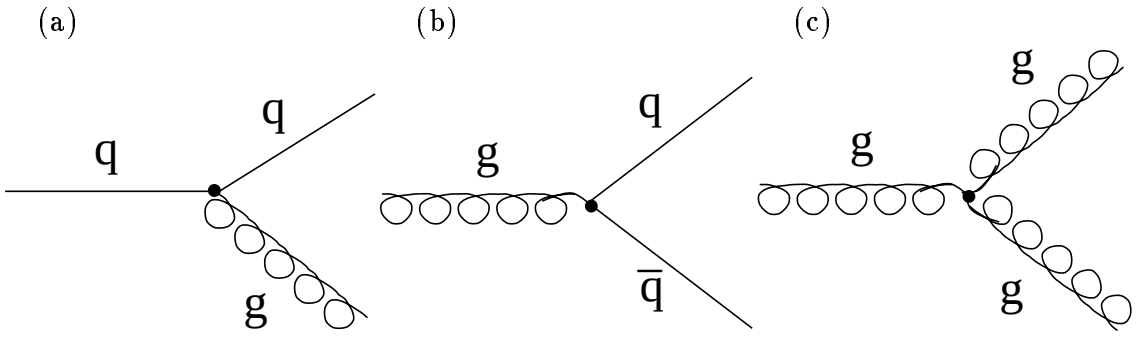

Figure 2.2: Some processes involved in the evolution of partons to small x in QCD.

The fact that gluons themselves carry colour (the charge associated with the strong force) and can thus exchange further gluons with one another, leads to running of the strong coupling parameter α_s in the opposite direction to that of the electromagnetic coupling α_{em}. At large momentum transfers (short distances), α_s is small and the interaction is relatively weak. This has the consequence that quarks probed with a high-Q^2 photon behave as if they are not influenced by the other partons in the proton. This behaviour, *asymptotic freedom*, is responsible for the success of the simple quark-parton model. At small momentum transfers (long distances), α_s is large. In fact it is so large that the energy required to separate a quark from the proton remnant is larger than that required to produce a new quark-antiquark pair. Thus the space between the struck quark and the proton remnant is populated with hadrons, but an individual, free quark is never produced. This *confinement* is the reason that only colourless states are ever observed.

Where the relevant momentum scale is large enough (larger than about 1 GeV^2) that α_s is much less than unity, perturbation theory may be used to predict cross sections from QCD. When no such 'hard scale' is present, perturbation theory is not applicable, and there is no way of making precise predictions. Instead, various phenomenological methods are used.

The simple quark-parton-model diagram in figure 2.1(b) is supplemented in QCD by higher-order processes such as boson-gluon fusion (BGF) and QCD

Compton radiation (QCDC), as illustrated in figure 2.3. In these processes, the system produced by the photon-parton interaction cannot be treated as massless, and the Bjorken variable x is no longer simply the momentum fraction carried by the struck quark.

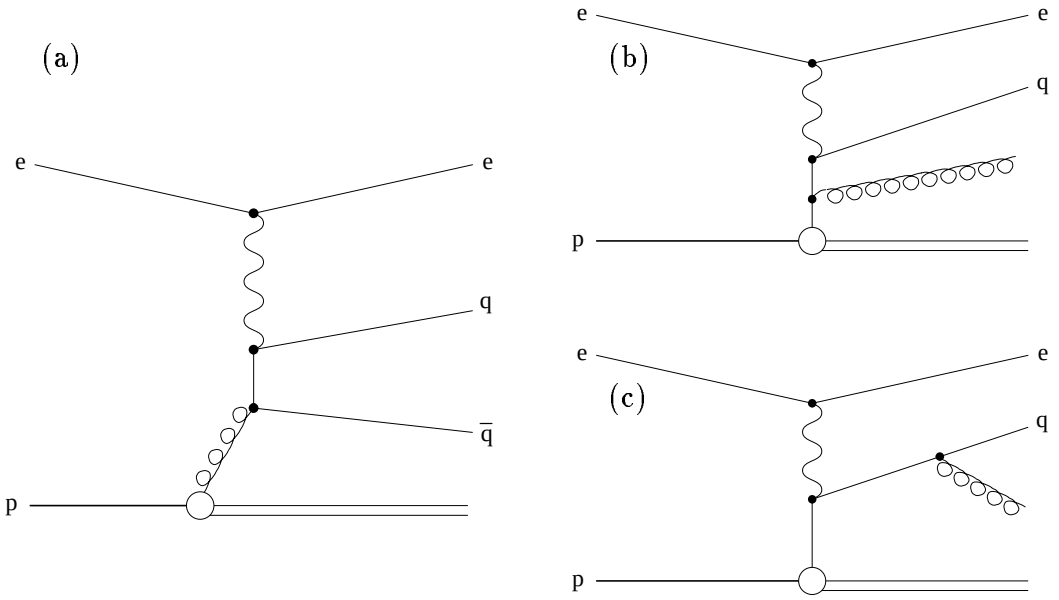

Figure 2.3: Higher-order QCD contributions to ep scattering: (a) Boson-Gluon Fusion (BGF); (b) and (c) QCD Compton (QCDC).

Structure-Function Measurements at HERA

The large centre-of-mass energy in ep collisions at HERA extends the range of Q^2 accessible for structure-function measurements up to about 4×10^4 GeV^2 (see figure 2.4). Precise measurements at such high values of Q^2 will have to wait for a much larger integrated luminosity than has so far been obtained, but there is already some evidence for a significant excess of events over the prediction of the Standard Model at very high Q^2. The accessible range also extends to much smaller values of x, down to below 10^{-5}, than were reached by previous experiments.

The steep rise of F_2 with decreasing x has been found to continue down to the smallest values of x that have been reached. This is in agreement with the prediction of DGLAP evolution, but it is expected that at some stage this rapid rise will slow down due to 'shadowing', where effects such as gluon recombination $gg \rightarrow g$ become significant. The value of x where this occurs depends on the model used: it may be very low if small-x partons are distributed uniformly within the

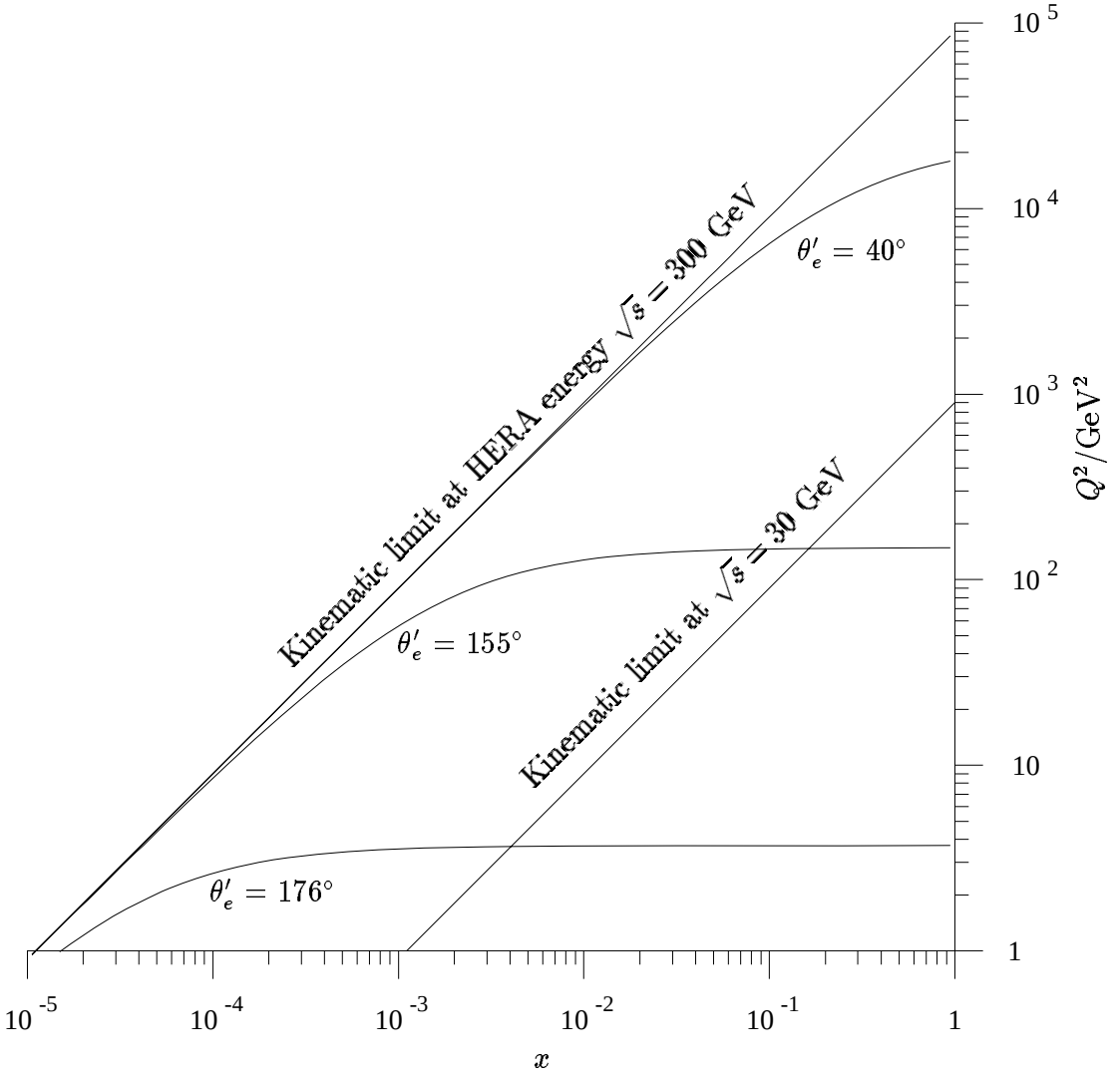

Figure 2.4: The range of x and Q^2 accessible in DIS at HERA and at earlier fixed-target experiments, where the centre-of-mass energy was an order of magnitude smaller. Contours of constant electron scattering angle θ'_e (relative to the proton beam direction) are shown.

proton, but within the range accessible at HERA if these partons are concentrated in small regions ('hot spots') around the valence quarks. In practice, it is difficult to tell whether hot-spot effects are significant from the behaviour of F_2 alone, since predictions at small x are based on evolution from measurements at larger x and contain significant uncertainties.

The gluon content of the proton can be measured using the scaling violations observed in F_2. At small x, F_2 is dominated by the contribution from sea quarks, created by pair production from gluons. The increase of F_2 with Q^2 is therefore dependent on the gluon distribution $xg(x)$. A next-to-leading-order QCD fit has been carried out [21], allowing the parameters describing the valence and sea quark distributions as well as the gluon distribution to vary.

In charged-current interactions, where the exchanged boson is a $W^{\pm}$, the scattered lepton in the final state is a neutrino and is not detected. The signature of such events is 'missing' transverse momentum: some momentum is carried away by the neutrino, leaving the observed final state with an apparently unbalanced transverse momentum. The charged-current cross section and its dependence on Q^2 have been measured and used to obtain a value for the W mass [22].

2.1.2 The Hadronic Final State

Although structure functions can say a lot about the structure of the proton and about QCD using only the inclusive DIS cross section, this approach throws away a lot of information which is contained in the hadronic final state. At HERA, it is possible to measure almost the entire hadronic final state, enabling useful measurements of energy flow, jet production and charm production, along with other processes.

Jet Production

According to the quark-parton model, the struck quark fragments into a jet of hadrons with a transverse momentum $p_\perp$ balancing that of the scattered electron, while the proton remnant, with no significant $p_\perp$, forms a separate jet. This is known as a $(1+1)$-jet event (one jet plus the proton remnant). Higher-order QCD processes result in some events with several high-momentum partons and hence several jets in the final state. BGF and QCDC processes (see figure 2.3), which are first order in α_s, can result in $(2+1)$-jet events (two jets plus the proton remnant). The ratio of

numbers of $(2+1)$- and $(1+1)$-jet events is therefore sensitive to the coupling α_s. The existence of multi-jet events and the agreement of Monte Carlo predictions with the observed jet distributions and profiles provide support for the QCD model. The ratio of numbers of events with different numbers of jets enables α_s to be measured and compared with the value found in e^+e^- scattering.

The rate of BGF events is proportional to the density of gluons in the proton, and a fit using next-to-leading-order QCD has been used to extract the gluon distribution $xg(x)$ from the observed (2+1)-jet events. This method can be used at larger values of x than are reached by the fit to F_2.

The behaviour of the parton densities at small values of x can be investigated [23] using events in which a large fraction of the proton's momentum goes into a jet in the forward direction, while the momentum carried by the struck parton is very small. Such an event occurs when the proton emits a gluon with a comparatively large momentum fraction x_j, which then radiates a gluon ladder, culminating in a quark at small x entering the hard subprocess. This process is sensitive to the evolution of gluons from large to small x, without depending on the less well known parton densities in the proton at small x. To reduce the effect of 'ordinary' DGLAP gluon radiation, and thus make the measurement sensitive to new effects such as shadowing and hot spots, the transverse momentum of the forward jet is required to be close to Q^2.

Energy Flow

In the quark-parton model, the struck quark and the proton remnant fragment independently; the current (struck-quark) jet has the same direction and momentum as the quark it comes from. The expected result in the detector is therefore two patches of energy deposition separated by a gap. This situation is modified in QCD, where the two jets are not completely independent. A string of colour-field flux joins the struck quark and the proton remnant; this string fragments into hadrons as it is stretched by the outgoing partons, filling the gap between the jets with energy flow.

The direction of the struck quark can be reconstructed using the direction and energy of the scattered electron. The amount of energy deposition can then be plotted against direction relative to the struck quark, as shown in [24]. The resulting histogram shows two peaks, corresponding to the two jets, but the current

jet is shifted by about 0.5 units of pseudorapidity[2] towards the direction of the proton remnant, and there is a substantial energy flow covering the interval between the current jet and the proton remnant, as expected from QCD.

Charm Production

The large mass of the charm quark compared to the lighter (u,d,s) quarks makes a difference to the way it is produced in ep interactions. Because the proton contains no charm quarks in its valence structure, the largest contribution to charm production comes from boson-gluon fusion. Thus the rate of production of charm is sensitive to the density of gluons in the proton, and provides a measurement of $xg(x)$ independent of that from the inclusive structure function F_2. The measured charm structure function F_2^c [25] is close to that expected from the fit to F_2, but slightly larger at small Q^2 (12 GeV^2).

Charm events, in which a $c\bar{c}$ pair is produced, may be divided into *open-charm* and *hidden-charm* events. In production of open charm, there is a large momentum difference between the quark and antiquark, which fragment independently – typically into a D and a $\bar{D}$ meson. If the quark and antiquark are close together in momentum space, they may form a bound state – a J/ψ or one of its excited states – which has a net charm of zero, so the charm is 'hidden'. The cross section for elastic production of J/ψ mesons in leading-order perturbative QCD is proportional to the square of the gluon density. This provides another way of measuring $xg(x)$, with the hard scale necessary for perturbative QCD to be applied being provided by the mass of the J/ψ. Both in DIS and in photoproduction ($Q^2 \approx 0$), this cross section rises steeply with W, consistent with the large gluon density at small x. This result is inconsistent with the expectation of a model assuming a soft pomeron (see chapter 3).

2.2 Photoproduction

Since the differential cross section for photon-mediated ep interactions contains a factor $1/Q^4$ due to the photon propagator, the total cross section for ep scattering is dominated by interactions at very low Q^2. The $Q^2 \to 0$ limit of DIS, where the exchanged photon is 'quasi-real' (nearly on its mass shell) is called *pho-*

[2]The pseudorapidity η is defined as $-\ln(\tan\frac{\theta}{2})$, where θ is the polar angle with respect to the direction of the proton beam.

toproduction. It is possible to treat this process as the emission of a photon by the electron followed by the independent interaction of the photon with the proton. The flux of quasi-real photons from the electron can be calculated using the Weizsäcker-Williams approximation [26, 27] and used to extract the γp cross section from that for the measured ep process.

A real photon can interact in a *direct* process, in which it behaves as a point-like QED photon as in DIS, but it can also fluctuate into a hadronic state by the process $\gamma \rightarrow q\bar{q}$ before interacting with the proton, in which case it is said to be *resolved* (see figure 2.5). This leads to a large class of events which are in many ways similar to hadron-hadron collisions. The largest contribution to the hadronic part of the photon wave function comes from low-mass vector mesons with the same quantum numbers as the photon – the ρ, ω and ϕ. The *vector-meson dominance model* (VDM) [28] treats the photon as a superposition of the bare photon with these three mesons contributing with factors depending on their mass and on their effective coupling to the photon. The generalized VDM [29] additionally takes into account the heavier mesons (ρ', J/ψ, Υ etc.), and the extended VDM [30] allows for a continuum of unbound states as well.

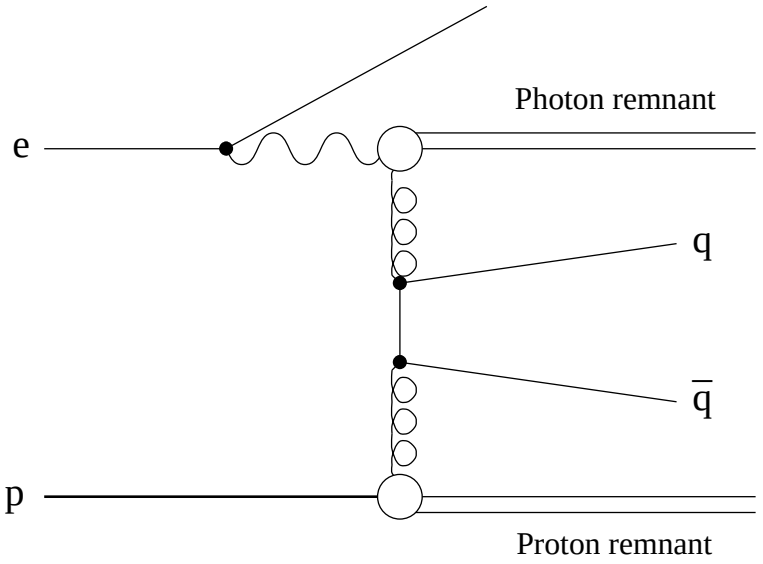

Figure 2.5: A leading order diagram for resolved photoproduction.

Photoproduction can also be divided into *hard* and *soft* processes. Although Q^2 is small, a hard scale is provided in some events by a large transverse momentum between outgoing partons (showing up as jets after hadronization), allowing predictions to be made using perturbative QCD. The leading-order diagrams (figure 2.3) are BGF (which is sensitive to the gluon content of the proton) and QCDC. There

is no completely unambiguous distinction between next-to-leading-order direct processes and leading-order resolved ones, but the hard subprocess provides a convenient dividing point. Once this distinction has been drawn, resolved processes can be used to measure the structure function of the photon, which is defined in the same way as the structure function of a hadron. The photon structure function has been measured for real photons [31] and preliminary results have been obtained by ZEUS for photons with small but measurable virtuality ($0.1\ \text{GeV}^2 < Q^2 < 0.6\ \text{GeV}^2$) [32].

In the majority of photoproduction events, there is no hard scale; this is soft photoproduction, where perturbative QCD cannot be applied. The only predictions are those supplied by phenomenological models such as Regge theory, which is discussed in chapter 3. These soft processes are interesting both in their own right and because of their influence on measurements of the theoretically more tractable hard processes. Not only do soft interactions form a large background to deep-inelastic events, but they are important in multiple interactions and in hadronization, making the interpretation of hard processes more complicated.

Chapter 3

Diffractive Scattering and the Pomeron

Events with a large rapidity gap – a region free of hadrons between the proton remnant and the current region – have been observed both in photoproduction [33, 34, 35, 36] and in DIS [37, 38] at HERA. Such events are explained as being due to the exchange of a colourless object, so that there is no string of colour field connecting the two parts of the hadronic final state and filling the gap by hadronization. Similar *diffractive* events have been observed for decades in hadron-hadron collisions, but there is no agreed mechanism for them in terms of QCD. They are, however, well described by Regge theory – the phenomenological model of colourless exchanges between hadrons, which predates QCD. DIS at HERA offers a new way of probing the partonic structure of the diffractive exchange and thus distinguishing between the various models that have been proposed.

This chapter begins with a discussion of hadron-hadron interactions and their description in terms of Regge theory. Then the connection with lepton-hadron interactions is explored, along with the ways in which diffractive interactions are investigated at HERA, and some of the models which have been suggested to make sense of the results.

Regge theory and its application to hadronic interactions are described in more detail in [39, 40].

3.1 Hadron-Hadron Interactions

Cross sections for hadron-hadron scattering contain a large contribution from elastic processes with a small four-momentum transfer. These are soft interactions; the relevant value of the coupling α_s is too large for perturbative QCD to be used. The best description of such processes is still provided by pre-QCD phenomenological models based on general considerations such as crossing symmetry and the analyticity of scattering amplitudes.

At high energies, scattering amplitudes are dominated by exchange terms, which vary smoothly with energy, free of the resonance structure which dominates at lower energies. The objects exchanged in elastic interactions (and in all long-range interactions, due to colour confinement) are colour singlets. Crossing symmetry is used to relate the exchange of these states in the t-channel reaction to the formation of the same state as a resonance in the corresponding s-channel reaction (see figure 3.1). The scattering amplitude for the t-channel process is obtained by analytically continuing the amplitude for the s-channel reaction into a different region of s and t.

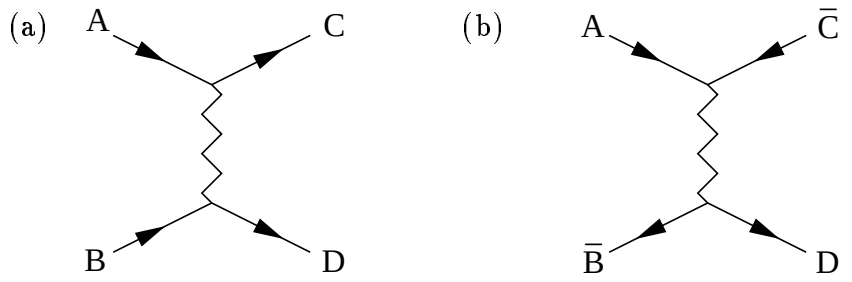

Figure 3.1: An illustration of the relationship between (a) the t-channel reaction $AB \to CD$ and (b) the corresponding s-channel reaction $A\bar{C} \to \bar{B}D$.

The simplest approach is to consider only the exchange of the lightest meson consistent with conservation of the relevant quantum numbers; this is the *one-particle exchange* (OPE) model. The exchange brings a propagator of the form

$$\frac{1}{m^2 - t} \tag{3.1}$$

into the scattering amplitude, where m is the on-shell mass of the exchanged particle and t is the square of the four-momentum transfer. Since t is negative, the largest contribution comes from the lightest possible exchanged particle. Thus the OPE model provides a reasonable description in cases where exchange of one particle

dominates. In 1935 Yukawa used this model, in conjunction with measurements of the range of the force between nucleons, to predict the existence of the π^0 meson. However, for a more accurate and general description of cross sections for hadronic scattering, it is necessary to take into account all contributing exchanges.

Experiments on the scattering of pion beams by hydrogen targets revealed patterns in the resonances produced. When the spin of each resonance (or bound state) is plotted against the square of its mass, resonances with identical quantum numbers (other than spin) are found to lie approximately on straight lines, called *Regge trajectories* (see figure 3.2). This behaviour can be rationalized for mesons using a simple QCD-inspired model in which a meson consists of a quark and an antiquark connected by a string of gluons with energy proportional to its length. In such a system, the angular momentum of the meson is proportional to the square of the total energy. In general, each trajectory contains particles of either odd or even spin, but the ρ and f_2 trajectories, shown in figure 3.2, are degenerate, and lie on a single line.

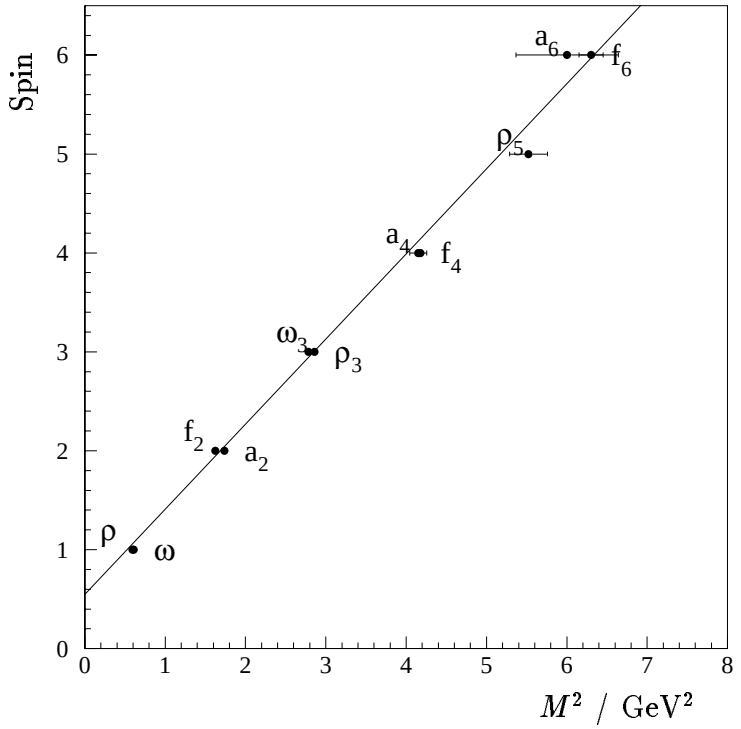

Figure 3.2: The degenerate Regge trajectories containing the ρ^0 and f_2.

Regge theory [40] is used to add up the contributions from all mesons on a trajectory. The straight line $\alpha(m^2)$ relating the spin α of each particle to its mass

m is relabelled

$$\alpha(t) = \alpha_0 + \alpha' t \tag{3.2}$$

where t, the four-momentum squared, is equal to the mass of a meson where t is positive and α is an integer, and to the squared four-momentum transfer in an exchange where t is negative. The contributions are added up using a method in which angular momentum is treated as a complex quantity [41], resulting in a scattering amplitude

$$A(s,t) \sim f(t) \left(\frac{s}{s_0}\right)^{\alpha(t)} \tag{3.3}$$

and a differential cross section for the two-body process $AB \to CD$

$$\frac{d\sigma}{dt} = F(t) \left(\frac{s}{s_0}\right)^{2\alpha(t)-2}. \tag{3.4}$$

The total cross section for AB interactions is related by the optical theorem to the imaginary part of the forward ($t = 0$) amplitude for elastic AB scattering. Using the Regge scattering amplitude, it is found to be

$$\sigma_{tot}(AB) \sim \left(\frac{s}{s_0}\right)^{\alpha_0 - 1}. \tag{3.5}$$

All known meson trajectories have intercepts α_0 less than 0.6. If these mesons were the only exchanged objects responsible for the behaviour of hadronic scattering, the elastic and total cross sections would decrease with increasing centre-of-mass energy $\sqrt{s}$. This is indeed the case at low energy ($\sqrt{s} < 10$ GeV), but at high energy a slow increase with s is seen. This corresponds to exchange of a trajectory with an intercept α_0 greater than one, matching none of the known mesons, and in the Regge picture is identified with the exchange of objects carrying even spin and the quantum numbers of the vacuum. This is the *vacuum* or *Pomeranchuk* trajectory, also known as the *pomeron* ($I\!P$). Scattering processes involving the exchange of the quantum numbers of the vacuum are termed *diffractive*, because the shape of the differential cross section plotted against the angle of the scattered proton resembles the diffraction pattern seen when a coherent beam of light is obstructed by a small obstacle. Diffractive processes include not only elastic scattering, but also processes in which one or both of the incoming hadrons are excited into a higher-mass state and break up. This is *diffractive dissociation.*

The positive slope α' of the Regge trajectories means that the dependence of the elastic cross section on t becomes steeper as the centre-of-mass energy of the reaction is increased. In other words, the forward diffractive peak becomes narrower; this phenomenon is called *shrinkage* and has been observed in hadron-hadron interactions [42].

As the pomeron has the quantum numbers of the vacuum, it is expected to couple equally to any particle and to its antiparticle. Thus the ratio of the elastic pp and $\bar{p}p$ cross sections should be equal to unity at high enough energies, where pomeron exchange dominates, and a similar result holds for the total cross sections. This result is given by the *Pomeranchuk theorem* [43] and is borne out by the data.

Donnachie and Landshoff [44] have fitted total cross sections for a variety of hadronic interactions using the sum of a meson contribution (which dominates at low energy) and a pomeron contribution (which dominates at high energy), assuming a universal pomeron. They find good agreement with the experimental results, and obtain a value of $\alpha_0 = 1.0808$ for the pomeron intercept and $\alpha_0 \approx 0.5$ for the meson intercept. They also note that the cross sections for πp and pp scattering are in a ratio of about 2:3, hinting that the pomeron may obey an *additive quark rule*, coupling to individual valence quarks rather than to the hadron as a whole.

Support for the idea of a direct coupling of the pomeron to valence quarks also comes from studies of diffractive proton dissociation at the CERN Intersecting Storage Rings (ISR) [45, 46]. For example, the reaction $pp \to (\Lambda^0 \phi K^+)p$, where the $\Lambda^0 \phi K^+$ system emerges along the beam direction with almost the energy of the incoming proton, can be interpreted as the dissociation of one of the protons as it collides with a pomeron emitted by the other proton: $p\mathbb{P} \to \Lambda^0 \phi K^+$ [45]. A clear pattern is seen in the final state when it is viewed in the zero-momentum frame of the dissociative system. The Λ^0, which contains two of the valence quarks of the incoming proton, is peaked in the forward direction, parallel to the direction of the proton. The K^+, which contains one of the valence quarks of the incoming proton, is peaked in the backward direction, parallel to the incoming pomeron. The ϕ, with its valence-quark content coming entirely from hadronization, has only a little momentum and is not peaked in either direction. This behaviour is attributed to an interaction in which the pomeron couples to a single u valence quark in the proton, ejecting it and leaving behind a spectator quark pair.

It is still not clear what the pomeron *is* in terms of QCD, despite its success in describing hadron-hadron scattering. The simplest relevant QCD process is exchange of a pair of gluons, and it has been suggested the Pomeranchuk trajectory is a line linking glueball states. A resonance with the right quantum numbers ($J^{PC} = 2^{++}$), showing evidence of a significant gluon content, has been seen at a mass of 1900 MeV by the WA91 and WA102 collaborations [47, 48].

Ingelman and Schlein [49], treating the pomeron as an object with a partonic structure, like a hadron, predicted the occurrence of hard scattering between a

gluon from the pomeron emitted by one hadron and a parton from the other hadron, resulting in an event with two high-momentum jets. They recommended looking at this process as a way of gaining insight into the structure of the pomeron. The existence of these events was confirmed by UA8 [50, 51].

3.2 Photoproduction

As explained in section 2.2, the real photon behaves much like a hadron in its interactions with the proton. Cross sections for photon-hadron interactions behave much like those for hadron-hadron interactions, but are smaller by a factor of order α_{em}. Using the vector-meson dominance model to describe the coupling of the QED photon to hadronic states, Regge theory can therefore be applied to photoproduction.

The exclusive (quasi-elastic) photoproduction of vector mesons, $\gamma p \to Vp$, is closely related to the truly elastic process $Vp \to Vp$ and shows the same energy dependence. The energy dependence of the cross sections measured for exclusive photoproduction of light vector mesons (ρ, ω, ϕ) is compatible with that expected from the Donnachie-Landshoff pomeron intercept. However, elastic photoproduction of the heavier J/ψ meson is found to show a significantly steeper energy dependence [52, 53], corresponding to a larger pomeron intercept. This may be related to the harder scale introduced by the mass of the charm quark, which makes perturbative effects more significant.

The total photoproduction cross section $\sigma(\gamma p)$ has been measured [33, 54] and these results are also compatible with the energy dependence expected from the Donnachie-Landshoff pomeron intercept [44].

A significant proportion of the photoproduction cross section consists of diffractive dissociation (see figure 3.3), in which the hadronic final state consists of two systems – one arising from the photon and the other from the proton – not connected by any colour string. Such events are distinguished in the detector by a *rapidity gap* – an angular region free of energy deposits between the proton remnant or elastically scattered proton and the rest of the hadronic final state – and have been studied at H1 [36].

Hard processes in which the final state includes two back-to-back jets have been observed in diffractive photoproduction [34, 35], supporting the idea that the

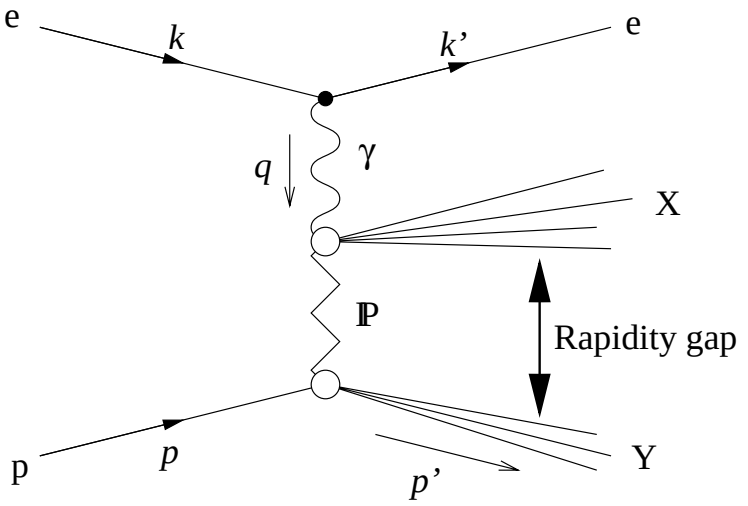

Figure 3.3: A schematic diagram of the process leading to formation of a rapidity gap.

pomeron can be interpreted as a partonic system.

3.3 Deep-Inelastic Scattering

Deep-inelastic events with a rapidity gap in the forward direction have been observed by both ZEUS [37] and H1 [38] (see figure 3.4). These indicate a colour-singlet exchange between the virtual photon and the proton, which is scattered elastically or dissociates into a low-mass state and is lost in the beam pipe. It is natural to assume that the mechanism is related to that responsible for similar events in photoproduction and is diffractive in nature.

The scattered proton, which has a very small transverse momentum $p_\perp \approx \sqrt{t}$, could not be detected using the H1 detector in its 1994 configuration. Instead, the presence of a rapidity gap extending up to the beam pipe is used as a signature of diffractive exchange. This is quantified using the variable η_{max}, defined as the pseudorapidity

$$\eta = -\ln\left(\tan\frac{\theta}{2}\right) \tag{3.6}$$

of the most forward energy deposit of more than 400 MeV. A small η_{max} indicates a large rapidity gap. The number of events with large rapidity gaps is much greater than predicted by a 'standard DIS' Monte Carlo generator, which produces large

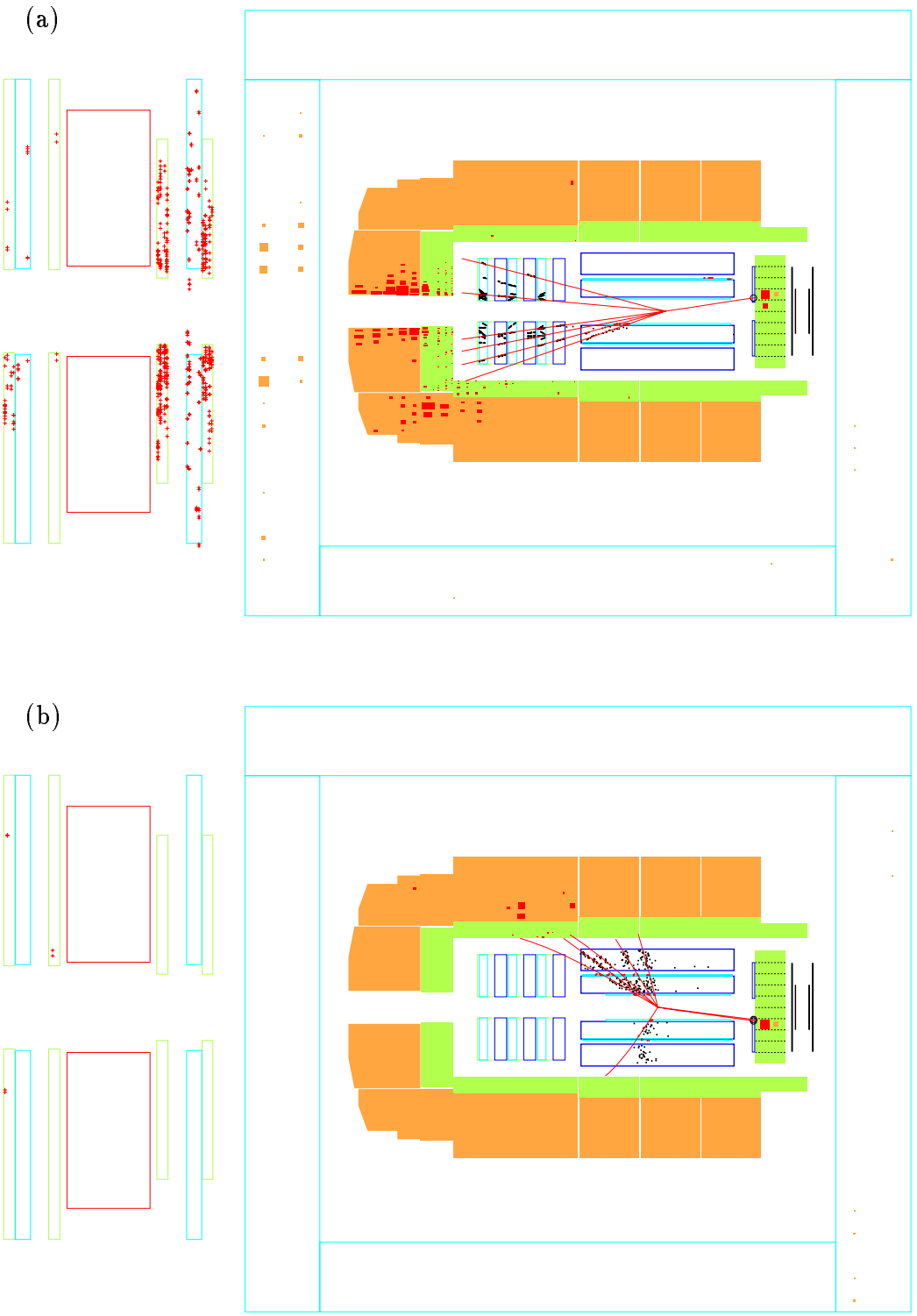

Figure 3.4: (a) A 'standard' deep-inelastic event with no rapidity gap, as seen in the H1 detector. (b) A deep-inelastic event with a rapidity gap, as seen in the H1 detector.

rapidity gaps only as rare statistical fluctuations in the hadronization process (see figure 3.5).

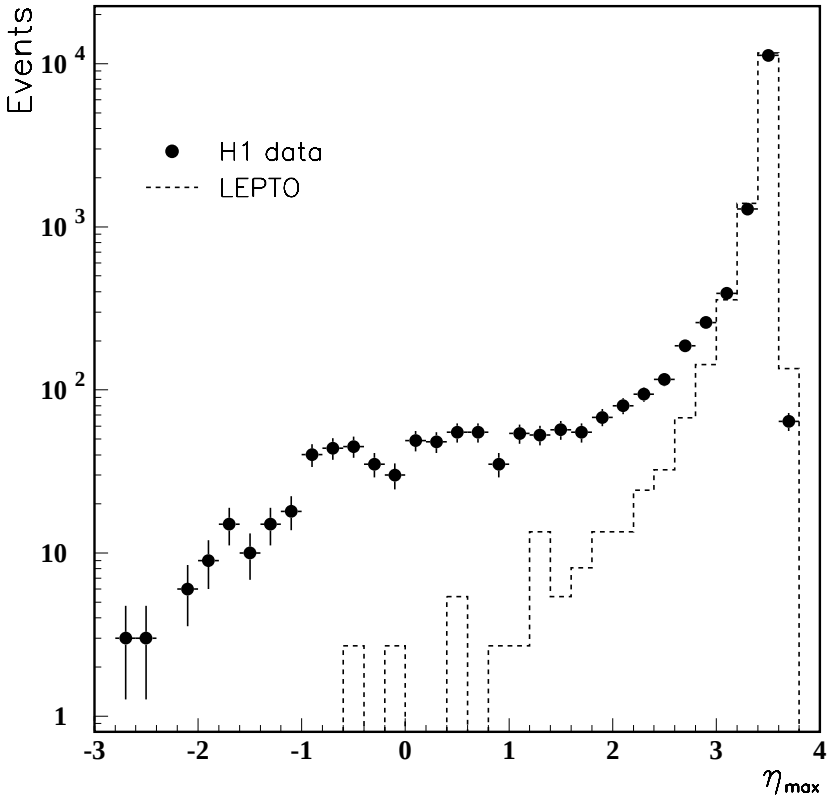

Figure 3.5: Distribution of measured η_{max} for DIS events, compared with the expectation of a 'standard DIS' model (LEPTO). Taken from [38].

The clear separation of the hadronic final state into two systems X and Y, as labelled in figure 3.3, allows three further kinematic quantities to be defined, in addition to those used in standard DIS (section 2.1.1):

$$t = (p - p')^2 \tag{3.7}$$

$$\beta = \frac{Q^2}{Q^2 + M_X^2} \tag{3.8}$$

$$x_{I\!P} = \frac{Q^2 + M_X^2}{Q^2 + W^2}. \tag{3.9}$$

The Mandelstam variable t is the squared four-momentum carried by the colour-singlet exchange (the pomeron in the Regge picture). The variables β and $x_{I\!P}$ are analogous to x and y. Like x for the proton, β is the fraction of the momentum of the pomeron going into the hard subprocess (interacting with the virtual photon). In the limit $t \to 0$, $x_{I\!P}$ is the fraction of the momentum of the proton carried away by the pomeron.

The contribution of diffractive events with an elastically scattered proton can be quantified by defining a diffractive structure function $F_2^{D(4)}$, analogous to the inclusive proton structure function F_2:

$$\frac{d^4\sigma_{ep\to epX}}{dxdQ^2dx_{I\!P}dt} = \frac{4\pi\alpha^2}{xQ^4}\left\{1 - y + \frac{y^2}{2[1 + R^{D(4)}(x, Q^2, x_{I\!P}, t)]}\right\} F_2^{D(4)}(x, Q^2, x_{I\!P}, t). \tag{3.10}$$

In practice, t cannot be measured since the scattered proton is not detected, so the measured cross section is actually an integral over t up to $|t| \approx 1$ GeV^2. This limit is determined by the requirement that the proton remnant is not detected. The ratio of the cross sections for diffractive processes due to longitudinally and transversely polarized photons, $R^{D(4)}$, is not well measured and its value makes only a small difference to $F_2^{D(4)}$, so it is set to zero for the measurement made by H1 [55, 56] of the structure function $F_2^{D(3)}$, defined by

$$\frac{d^3\sigma_{ep\to epX}}{dxdQ^2dx_{I\!P}} = \frac{4\pi\alpha^2}{xQ^4}\left\{1 - y + \frac{y^2}{2}\right\} F_2^{D(3)}(x, Q^2, x_{I\!P}). \tag{3.11}$$

Some models, such as that of Ingelman and Schlein [49], feature a factorizable diffractive structure function

$$F_2^{D(3)} = {F_2}^{I\!P}(\beta, Q^2) \cdot f_{I\!P/p}(x_{I\!P}) \tag{3.12}$$

where ${F_2}^{I\!P}$ is the structure function of the pomeron and the *flux factor* $f_{I\!P/p}$ describes the pomeron content of the proton. This makes sense in a picture where the pomeron is a hadronic object that is emitted by the proton and then probed by the virtual photon in a hard interaction. Although initial results [55] were consistent with factorization, a more recent study using higher statistics [56] shows that factorization in this simple form does not hold. This may simply be because there is a contribution at larger $x_{I\!P}$ from meson exchange; the results are consistent with the sum of two individually factorizable components – one from a meson trajectory and one from pomeron exchange. However, it may be that even the purely diffractive (pomeron-exchange) component does not factorize due, for example, to multiple pomeron exchange, or to a failure of the picture of the pomeron as a particle-like object.

The nearest practically measurable quantity to the pomeron structure function $F_2^{I\!P}$ is the integral of the diffractive structure function $F_2^{D(3)}$ over the available range of $x_{I\!P}$:

$$\tilde{F_2^D}(\beta, Q^2) = \int_{x_{I\!P_L}}^{x_{I\!P_H}} F_2^{D(3)}(\beta, x_{I\!P}, Q^2) dx_{I\!P}. \tag{3.13}$$

The results obtained by H1 [56] are shown in figure 3.6. Even if factorization does not hold to high precision, $\tilde{F_2^D}$ provides a measure of the 'average' deep-inelastic

structure of the diffractive exchange. If $F_2^{D(3)}$ is treated as the sum of two factorizable components, $\tilde{F_2^D}$ may be extracted from the separated pomeron component, or by using the total $F_2^{D(3)}$ in a region where $x_{I\!P}$ is small enough for the meson component to be small. The two methods give compatible results. The 'pomeron structure function' $\tilde{F_2^D}$ shows a logarithmic rise with Q^2, like the proton structure function F_2, consistent with a partonic structure for the pomeron. The fact that this rise with Q^2 is present up to fairly large values of β suggests a structure of valence gluons; hadrons, with their valence quark structure, show a decrease with Q^2 at high x, due to the valence quarks losing momentum by radiating gluons.

If the pomeron is treated as a hadronic object, its quark and gluon content can be obtained using a QCD-based fit to the diffractive structure function $\tilde{F_2^D}$ [56]. The result is a structure in which 80% of the momentum of the pomeron is carried by gluons, which are strongly peaked near $\beta = 1$ at $Q^2 = 2.5$ GeV^2, the starting scale used for the DGLAP evolution. In other words, at this scale the momentum of the pomeron is often carried almost entirely by a single gluon. At higher Q^2, QCD evolution spreads the distribution more evenly over the available range in β. The β distributions at two different values of Q^2 are shown in figure 3.7.

The exclusive production of vector mesons has also been studied in DIS [57, 58]. Because the photon involved is now a long way off its mass shell, the vector-meson dominance model is no longer applicable, but the concept of pomeron exchange can still be used. The cross section for J/ψ production grows significantly faster than the soft pomeron prediction, and is consistent with the harder behaviour expected from a perturbative QCD calculation. The situation is less clear in the case of the lighter ρ meson. ZEUS [57] find results compatible with hard, perturbative behaviour, while H1 [58] find a rate of increase intermediate between the soft and hard predictions, suggesting that this is a region where soft pomeron behaviour is no longer seen, but perturbative QCD is not yet applicable.

The total cross section for scattering of virtual photons on protons at high centre-of-mass energy W is another interesting quantity to compare with pomeron-based and perturbative predictions. The high-W region corresponds to small x in the more usual way of expressing total DIS cross sections, the structure function $F_2(x, Q^2)$. If the $\gamma^* p$ cross section follows a power law $W^{2\alpha_0 - 2}$ then the structure function should follow a power law $F_2 \propto x^{1-\alpha_0}$ as $x \to 0$. The observed behaviour [21], with α_0 increasing from ~ 0.2 to ~ 0.4 as Q^2 increases from 1.5 GeV^2 to 800 GeV^2, is incompatible with the soft Donnachie-Landshoff pomeron. As in the case of exclusive production of vector mesons in DIS and exclusive photoproduc-

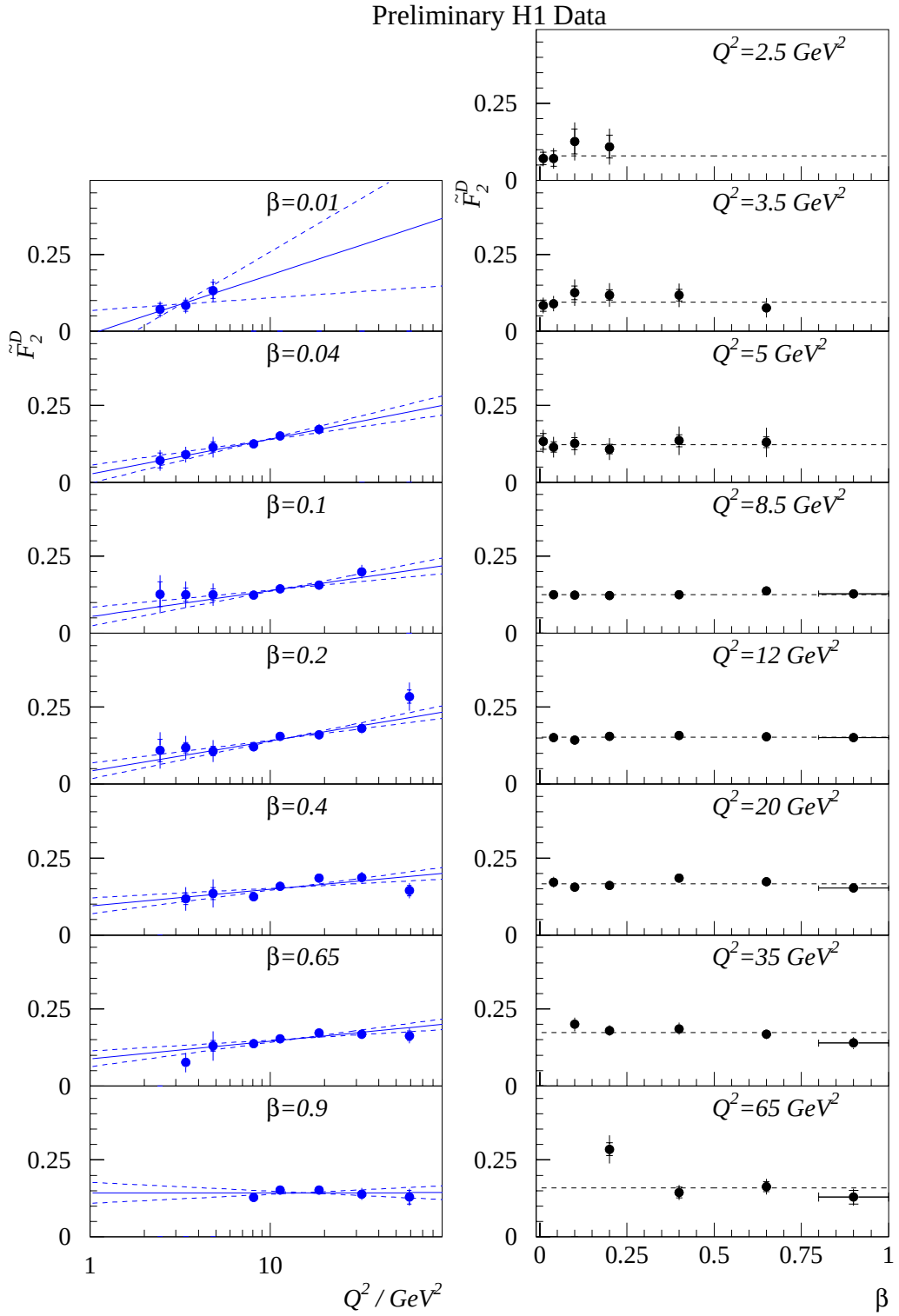

Figure 3.6: The structure function $\tilde{F}_2^D(\beta, Q^2)$ as a function of Q^2 for different values of β (left) and as a function of β for different values of Q^2 (right). Taken from [56].

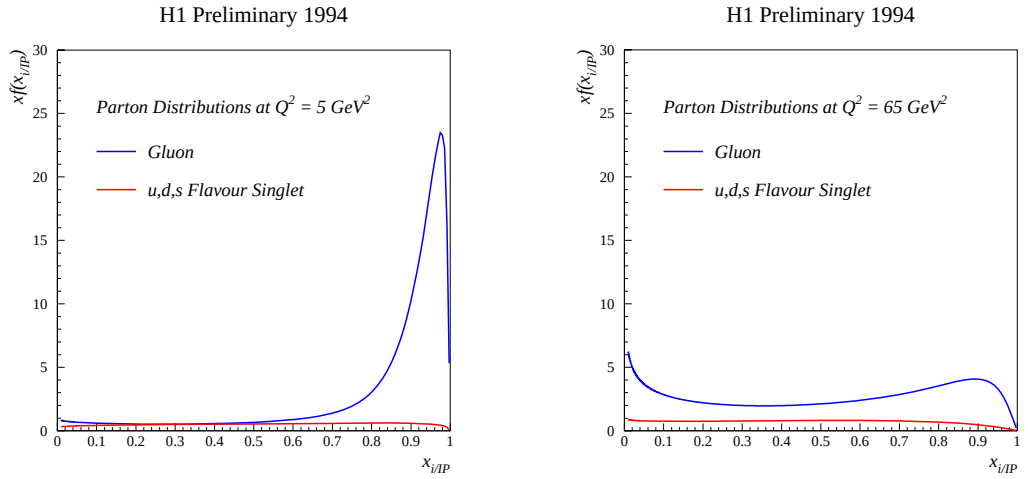

Figure 3.7: Gluon and quark distributions in the pomeron, extracted from a QCD-based fit to $F_2^{D(3)}$: (a) at low Q^2, showing the large contribution from gluons near $\beta = 1$; (b) at higher Q^2, after evolution to smaller β. Taken from [56].

tion of J/ψ mesons, the steeper energy dependence may be related to perturbative effects.

3.4 Models of Hard Diffraction

3.4.1 Factorizable Models

A lot of work on the phenomenology of diffractive interactions is based on the idea of *factorization*, meaning that the cross section for a hard diffractive process (such as jet production in hadron-hadron collisions or DIS at HERA) is treated as the product of a non-perturbative (soft) factor describing the emission of a pomeron by the proton, and a perturbative factor describing the hard interaction of a parton from the pomeron with a virtual photon or a parton from the other hadron. If this approach is valid, there must be a universal structure function for the pomeron, $F_2^{I\!P}$, which applies in DIS, in hard photoproduction and in hadron-hadron interactions. The pomeron structure function can be related to a set of hypothetical quark and gluon distributions in the pomeron in the same way as the proton structure function F_2 is related to the quark and gluon content of the proton. In this picture, the pomeron is treated more or less as a particle, although it is only

detected as a t-channel exchange, with a negative four-momentum squared.

This approach was suggested by Ingelman and Schlein [49], who used it to predict the production of jets in diffractive pp scattering, later confirmed at UA8 [50, 51]. They used two different pomeron structures, both dominated by gluons but with a hard distribution $xG(x) = 6x(1-x)$ in one case and a soft distribution $xG(x) = 6(1-x)^5$ in the other. Using the particle-like picture of the pomeron, they imposed a momentum sum rule $\int_0^1 xG(x)dx = 1$ to fix the normalization of the gluon distribution.

Other theorists use a similar approach – assuming factorization and trying to predict the pomeron structure function – but do not accept the other assumptions of the Ingelman-Schlein model. Donnachie and Landshoff argue that the partonic structure of the pomeron is dominated by quarks, citing as evidence the point-like coupling of the pomeron to valence quarks observed in soft hadronic interactions [59]. In their model the pomeron behaves like a $C = +1$ isoscalar photon and, as in the case of the photon, its point-like component means that its parton distributions do not obey a simple momentum sum rule.

Gehrmann and Stirling [60] investigate the necessity for such a point-like component to the structure of the pomeron by comparing two parametrizations. In each case, the pomeron contains valence quarks and gluons with a distribution $xf(x) \propto x(1-x)$, with the normalization of each determined by a fit to the data. The DGLAP equations are used to evolve the structure to values of Q^2 above the starting scale of 2 GeV^2. In the first model, this constitutes the entire structure of the pomeron, while in the second model there is an additional point-like component from pomeron-photon fusion via a quark loop. In the first case, the overall normalization is varied to fit the data, following the argument that, as the pomeron is not a real particle, the normalization of the flux factor, or equivalently of the structure function, need not be the same in hard processes as in soft ones. In the second case, the Donnachie-Landshoff flux factor is used without rescaling. Both models provide a reasonable fit to the data available at the time, but the Q^2 evolution predicted is significantly different in the two cases. With a direct coupling providing quarks at large β by splitting ($I\!P \to q\bar{q}$), there is an increase in the structure function with Q^2 at all values of β. Without this contribution, although there is some compensation from an increased gluon content, the structure function falls with Q^2 at large β.

The production of charm provides a powerful method of distinguishing between the two models of Gehrmann and Stirling and thus detecting a possible point-like component of the pomeron. In the first model, charm is produced by

photon-gluon fusion and takes place mainly at fairly small values of β. In the second model, in which the ratio of light quarks to gluons in the hadronic part of the pomeron structure is approximately twice as large, charm is mainly produced by the direct fusion process $I\!P\gamma^* \to c\bar{c}$ and occurs at larger values of β.

Kniehl, Kohrs and Kramer [61] also make predictions both with and without a point-like component to the pomeron. They calculate the angular and transverse-momentum distributions of jets produced in diffractive photoproduction and compare their results with data from H1 and ZEUS. They claim some support for a point-like contribution, although more accurate measurements using larger statistics are necessary to distinguish with more confidence between the models.

3.4.2 QCD Multi-Gluon Exchange

Factorization is not universally accepted to be a valid assumption in modelling diffractive processes. Some theorists have instead used perturbative QCD to model the exchange of two or more gluons, forming an overall colour singlet, without treating the pomeron as an object that is emitted by the proton before being probed by a hard interaction.

The simplest QCD diagram corresponding to exchange of a pomeron is the exchange of two gluons, as proposed by Low [62] and Nussinov [63]. This has been extended by Nikolaev and Zakharov [64], who find that while the exchange of two unconnected gluons leads, perhaps surprisingly, to some features similar to a particle-like pomeron, this does not extend to all processes. In particular, they find that there is a different effective pomeron flux factor for production of each quark flavour, with heavy flavours contributing mainly at low $x_{I\!P}$. This is incompatible with the picture of a universal pomeron. The production of each quark flavour is sensitive to its mass, with diffractive events making up 10–20% of u, d and s production, but only 1% of charm production. The yield of charm is significantly smaller in this calculation than is expected from a model with a particle-like pomeron.

Higher-order QCD contributions to diffractive exchange are expected to be dominated by a *gluon ladder*, illustrated in figure 3.8. This is the diagram described by the BFKL equation [65, 66], and is known as the *BFKL pomeron*. In the Regge picture, it corresponds to a fixed singularity [66]:

$$\alpha(t) = 1 + \frac{12\alpha_s \ln 2}{3}. \tag{3.14}$$

An experimental signature for BFKL pomeron behaviour is a tail of diffractive events

at large momentum transfer t. The BFKL equations describe a *hard* pomeron; its intercept is about 1.4, which is significantly higher than that of the soft Donnachie-Landshoff pomeron. It therefore predicts a much steeper energy dependence, as is indeed observed in those processes where a hard scale is present. The rise of F_2 at small x requires a pomeron intercept of about this size, although it can equally well be described by the DGLAP evolution equations, so it does not provide evidence specifically for BFKL dynamics.

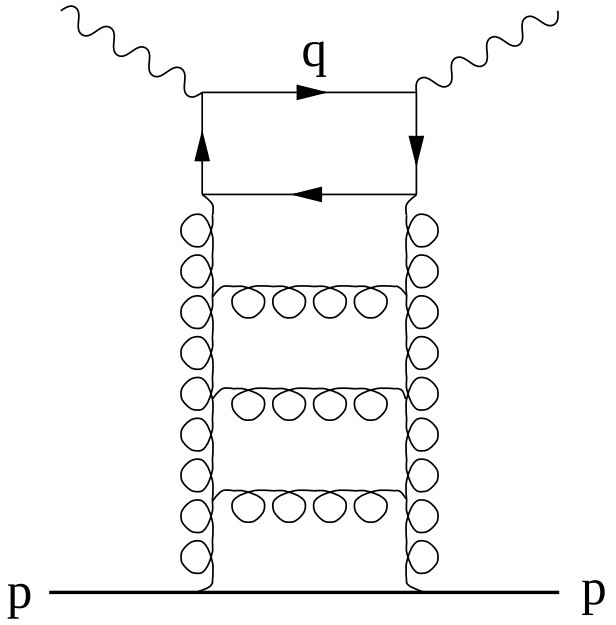

Figure 3.8: A gluon ladder, corresponding to pomeron exchange in the BFKL treatment.

3.4.3 Soft Colour Interactions

Buchmüller and Hebecker [67] do not assume the existence of the pomeron as a colour-singlet object emitted by the proton prior to the hard interaction. Instead, both diffractive and non-diffractive DIS are considered to be due to scattering of the electron on small-x gluons in the proton. In this model, the virtual photon interacts by fusing with a gluon to produce a quark-antiquark pair, which is initially in a colour-octet state. This quark-antiquark pair then changes colour randomly by soft interactions with the colour field of the proton. It may end up as a colour singlet, in which case it will fragment independently of the proton remnant, leaving a rapidity gap in the final state. This process, in which almost the entire momentum of the 'pomeron' is carried by a single gluon, fits in well with the shape – sharply

peaked near $\beta = 1$ – of the gluon distribution obtained from the QCD fit to $\tilde{F_2^D}$ [56].

If the quark-antiquark pair changes colour rapidly enough as it passes through the colour field of the proton, the probability that it will end up as a colour singlet is simply given by the ratio of numbers of singlet and octet colour states. The ratio of diffractive and total cross sections at small x is then predicted to be

$$R_D = \frac{\sigma_D}{\sigma_{tot}} \simeq \frac{1}{9}. \tag{3.15}$$

This prediction agrees well with the observed ratio of about 10%. An approximate scaling relation linking the diffractive and inclusive structure functions is also predicted by this model:

$$F_2^D(x, Q^2, x_{I\!P} = \xi) \simeq \frac{0.04}{\xi} F_2(x = \xi, Q^2). \tag{3.16}$$

This also agrees reasonably well with the data. This model also predicts a diffractive structure function that can be factorized into a part depending on $x_{I\!P}$ and a part depending on β and Q^2, although these are not interpreted in terms of a particle-like pomeron.

Similar in spirit to the Buchmüller-Hebecker model is the *soft colour interaction* (SCI) mechanism proposed by Edin, Ingelman and Rathsman [68, 69]. Again, the underlying hard interaction is the same in all DIS, and it is subsequent soft interactions that lead to a colour-singlet current system in some events. Several refinements are added that are not present in the Buchmüller-Hebecker model. Rather than just using the leading-order matrix element for the hard interaction, higher-order corrections are simulated by incorporating parton showers. An explicit model of the soft colour interactions is introduced: each pair of coloured partons in the partonic final state may interact, exchanging colour but not changing their momenta. The probability of this occurring cannot be calculated, but is described using an adjustable parameter. Hadronization is simulated using the Lund string model, and the entire SCI model is implemented as a Monte Carlo generator (LEPTO 6.5 [70]), enabling detailed comparisons with data. The model provides a reasonable description not only of rapidity-gap events, but also of energy flow in the forward region in non-diffractive DIS, where other models tend to produce too little energy.

3.4.4 Charm Production

Charm quarks are predominantly produced by the BGF process, so the rate of charm production in diffractive DIS is sensitive to the gluon content of the exchange involved: a gluon-dominated pomeron would result in a greater yield of charm than a quark-dominated one. The distribution of these events in β and Q^2 is sensitive to the details of the pomeron structure, with a larger contribution expected at large β if there is a point-like component present, as explained in section 3.4.1. The distribution in $x_{I\!P}$ provides a way of testing some models based on perturbative QCD (see section 3.4.2), which predict a breaking of Ingelman-Schlein factorization, with charm events more strongly peaked at small $x_{I\!P}$ than light-quark production.

3.5 Summary

Regge theory provides a very successful description of soft diffractive processes. A simple parametrization, corresponding to exchange of a soft pomeron, fits total cross sections as well as cross sections for forward elastic scattering in a wide range of hadron-hadron interactions and in photoproduction. However, this parametrization fails to describe interactions in which a hard scale is involved, such as deep-inelastic scattering and the exclusive photoproduction of the J/ψ meson. The cross sections for these reactions show a significantly steeper rise with energy than the soft pomeron would lead one to expect.

There is evidence, such as the production of high-momentum jets in diffractive photoproduction, for a partonic structure to the pomeron. Several different models have been proposed. In some, the pomeron is similar to an ordinary hadron. In others, pomeron exchange is equivalent to a set of Feynman diagrams containing gluon ladders, and its behaviour can be predicted by perturbative QCD when there is a hard scale present. It may even be that deep-inelastic diffraction can be explained as standard DIS followed by soft interactions in which the struck partonic system evolves into a colour singlet.

While there are indications in various processes for a pomeron that has a point-like character, and may comprise a leading gluon accompanied by one or more soft gluons to make up the colour balance, there is a need for further investigation to resolve the issue. Charm production is one process with an important role to play in this area. The goal is an explanation, in terms of QCD, of both soft and

hard diffractive interactions.

Chapter 4

The H1 Detector at HERA

4.1 The HERA Electron-Proton Collider

HERA (the Hadron-Electron Ring Accelerator) is the first, and to date the only *ep* collider to be built. Construction was authorized in April 1984 and completed in November 1990. The two general-purpose detectors H1 and ZEUS were then installed and the first *ep* collisions were recorded in late 1992.

By using a high-momentum beam of protons instead of a stationary hydrogen target, a much larger centre-of-mass energy is achieved. The beam energies used in 1994 – 27.5 GeV for the electrons and 820 GeV for the protons – correspond to a centre-of-mass energy of 300 GeV, compared to about 30 GeV for the previous generation of fixed-target experiments. The accessible kinematic range in deep-inelastic scattering is extended upward by about two orders of magnitude in Q^2 to approximately 4×10^4 GeV^2 and downward by a similar factor in x to below 10^{-5} (see figure 2.4).

The large asymmetry in the beam energies is made necessary by the limit on the electron beam energy imposed by energy losses through synchrotron radiation. The result is that the *ep* centre of mass is boosted in the proton direction with a Lorentz factor γ of 2.8 in the laboratory frame. This makes an asymmetric detector design necessary, with detector components concentrated in the forward (proton) direction, where the outgoing particle multiplicity is greatest. The angle of the scattered electron is amplified by the boost, so that the electron enters the main part of the detector for moderate values of Q^2, from ~ 4 GeV^2 to ~ 100 GeV^2, as well as for high-Q^2 events, above 100 GeV^2.

The HERA ring (figure 4.1) has a circumference of 6.3 km and comprises two separate accelerators for the two beams. Protons are accelerated in a linear accelerator, then in DESY 3 and PETRA 2, reaching 40 GeV before injection into HERA. They are then accelerated to their final energy of 820 GeV before electrons are injected. Electrons are accelerated in a separate linear accelerator, then in DESY 2 and PETRA 2, reaching an energy of 12 GeV before being injected into HERA and accelerated to 27.5 GeV (the design energy is 30 GeV). Once the beams have reached their final energies, collimators are moved in close to the beam, and the beam orbits are adjusted to bring the beams into collision at the interaction points in the North and South Experiment Halls. The North and South Halls are occupied respectively by the H1 and ZEUS experiments.

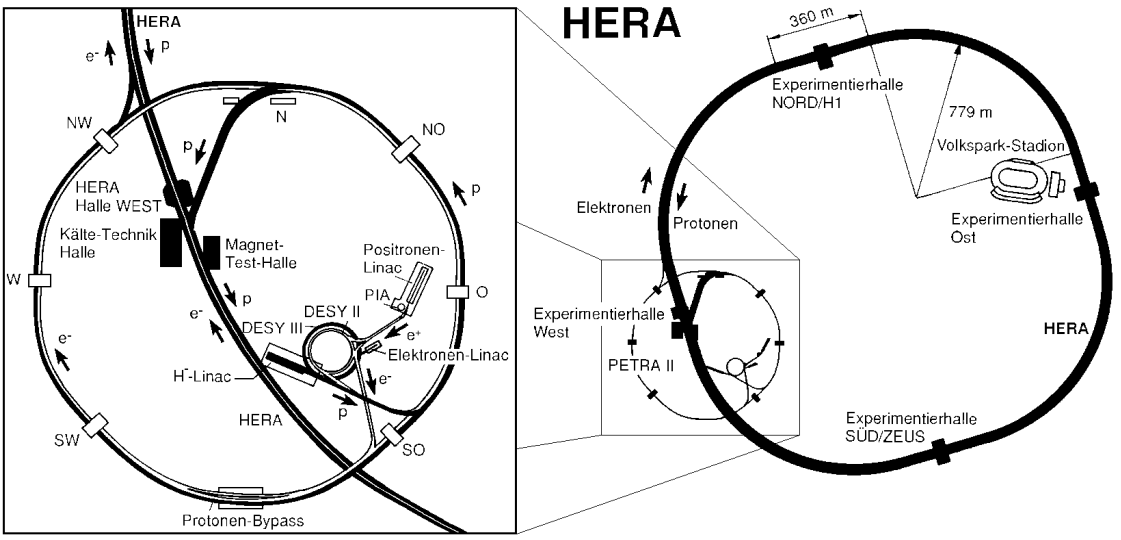

Figure 4.1: The HERA ring and its pre-accelerators.

The other two experiment halls on the HERA ring are used for fixed-target experiments. The East Hall houses the HERMES experiment, built to measure the spin-dependent nucleon structure functions [71]. HERMES uses the HERA electron beam, which is naturally polarized through the Sokolov-Turnov effect, as a probe of a polarized gas target. HERMES started taking data in the summer of 1995 and has made a preliminary measurement of the neutron spin structure function. The HERA-B experiment, under construction in the West Hall, uses the HERA proton beam on a wire target to produce B hadrons for the study of CP violation.

The beams are not continuous, but consist of bunches spaced 96 ns apart. In 1994, 153 electron and proton bunches were filled and brought into collision in the H1 and ZEUS detectors. A smaller number of unpaired *pilot* bunches were used

for studies of beam-induced background.

Since July 1994, positrons have been used in place of electrons. The main advantage of this is the reduced rate of beam-gas interactions: a positively charged beam repels positive ions from the path of the beam, while a negatively charged beam attracts them. The beam lifetime at high currents is longer than it was for electrons. The cross section for neutral-current interactions, in which the intermediate boson is a photon or Z^0, is unchanged. However, the cross section for charged-current interactions is halved due to the different numbers of u and d quarks in the proton, which can couple to an incoming W^- or W^+ respectively.

4.2 Overview of the H1 Detector

A major consideration in the design of the H1 detector was the identification and energy measurement of electrons for the study of neutral-current interactions. It is also important to be able to measure tracks and energy flow, particularly in jets, where the local track multiplicity is high. Therefore a jet chamber and a highly segmented calorimeter are used. The calorimeter, as well as the jet chamber, is positioned inside the solenoid to minimize the amount of dead material in front of it. The calorimeter is made as nearly hermetic as possible for measurements of energy flow and of missing energy, as found in charged-current events. The asymmetry in the beam energies requires an asymmetric detector, and the high bunch-crossing and background rates mean that a sophisticated triggering system is necessary.

The H1 detector is described in detail in [72, 73]. The description given here is a summary, concentrating on the parts of the detector that are particularly relevant to this analysis. The main parts of the detector (figures 4.2 and 4.3) are, in order of increasing distance from the interaction point:

- the tracking system, which detects charged particles leaving the interaction point and measures their momenta;
- the calorimetry system, which measures the energy of charged and neutral particles;
- the solenoid, which provides a 1.15 T magnetic field, enabling the momentum of particles to be measured from the curvature of their tracks;
- the muon-detection system, which identifies penetrating particles travelling

through the tracking and calorimetry systems without giving up a large fraction of their energy.

Positions within the H1 detector are given using a right-handed Cartesian coordinate system (illustrated in figure 4.2) with the origin at the nominal interaction point, the z axis in the direction of motion of the proton beam, the x axis horizontal and the y axis vertically upwards. Alternatively, the polar and azimuthal angles θ and ϕ can be used, where $\theta = 0$ is the direction of motion of the proton beam (also known as the *forward* direction), and $\phi = 0$ is on the x axis and $\phi = \frac{\pi}{2}$ on the y axis.

4.3 Tracking

The H1 tracking system (figure 4.4) is divided into two independent detectors: the central and forward tracking detectors (CTD and FTD). Each is optimized for the angular region that it covers. The tracking detectors lie within the solenoid, in a region with an approximately uniform magnetic field of 1.15 T parallel to the beam axis. By accurately reconstructing tracks in the $r\phi$ plane, the transverse momentum $p_\perp$ of charged particles can be measured. Drift chambers are used for track reconstruction; proportional chambers, with their faster response, are used for triggering of events with charged tracks originating near the event vertex.

The Central Tracker

The central tracker [2] [1] (figure 4.5) covers the region $20° < \theta < 160°$. Track reconstruction in this region is based on two concentric drift chambers: the central jet chambers CJC1 (inner) and CJC2 (outer). Each is divided azimuthally into a number of drift cells (30 in CJC1, 60 in CJC2) with anode and field-shaping wires parallel to the beam axis. The cells are angled at about 30° to the radial direction so that the ionization electrons, influenced by the magnetic field of the solenoid as well as the electric field in the cell, drift approximately perpendicular to high-momentum tracks. This gives the best drift-time resolution. The tilt also means that *mirror tracks*, resulting from the left-right ambiguity in a drift cell, do not point to the vertex or to the corresponding track segments in other cells, and are thus more easily distinguished from genuine tracks.

[1] Numbers in boxes refer to the labels in figure 4.2.

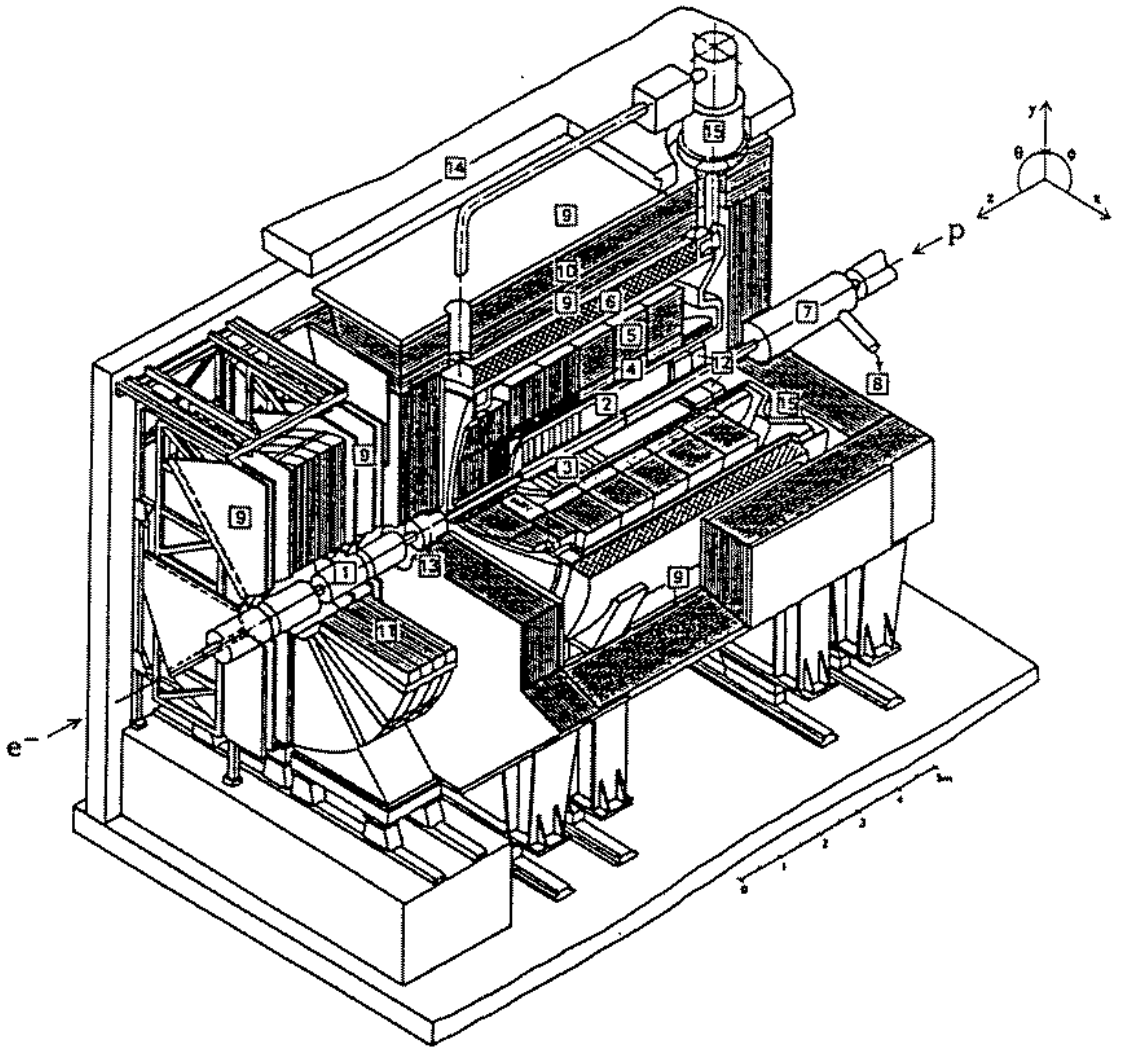

1	Beam pipe and beam magnets	9	Muon chambers
2	Central tracking detector	10	Instrumented iron return yoke
3	Forward tracking detector	11	Forward muon toroid
4	Electromagnetic calorimeter	12	BEMC
5	Hadronic calorimeter	13	Plug calorimeter
6	Solenoid	14	Concrete shielding
7	Compensating magnet	15	Liquid argon cryostat
8	Helium supply for 7		

Figure 4.2: Cut-away view of the H1 detector.

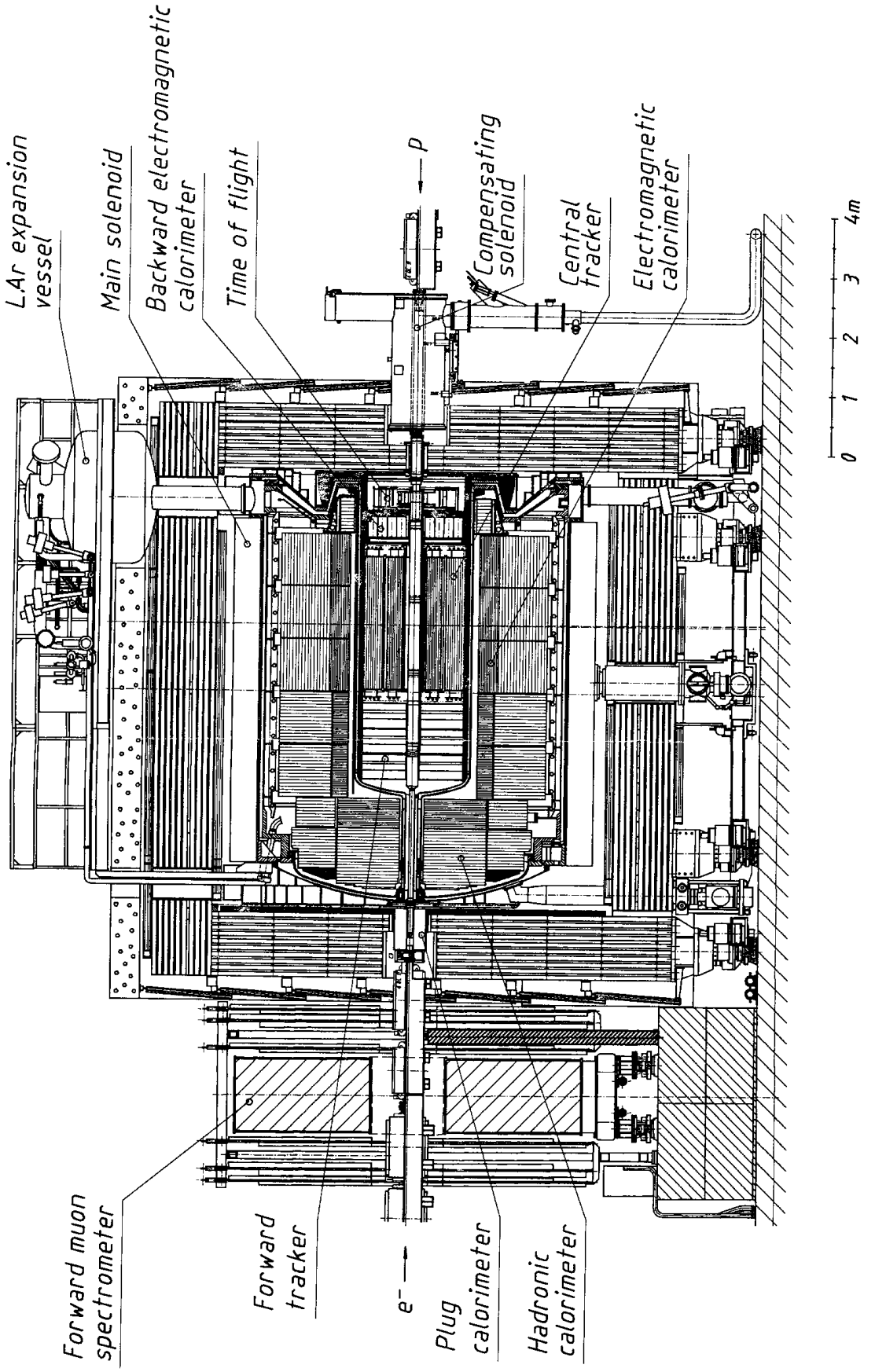

Figure 4.3: Longitudinal section of the H1 detector.

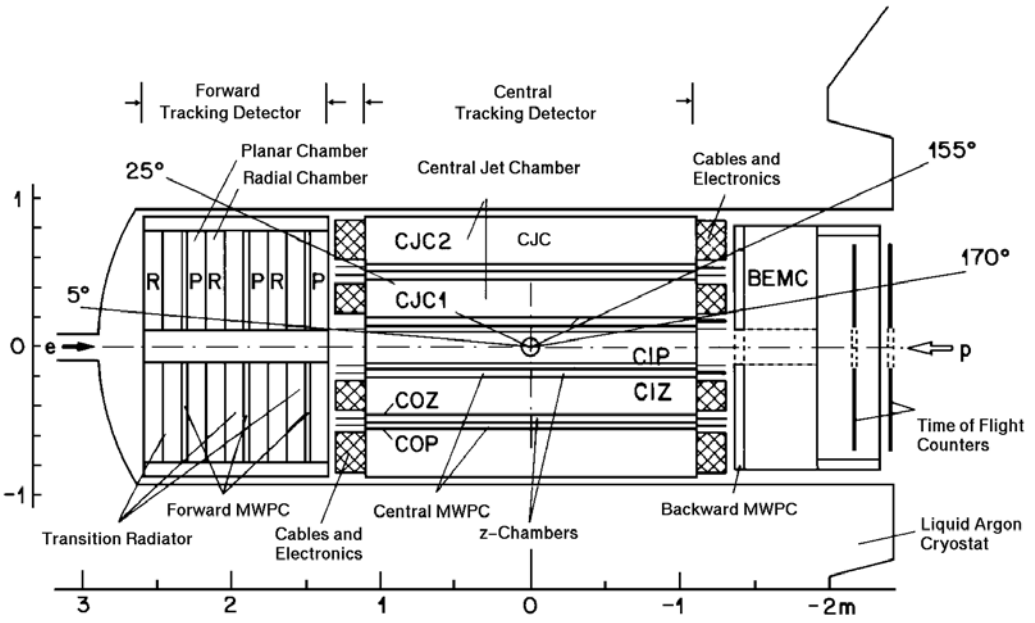

Figure 4.4: Longitudinal section of the H1 tracking system.

The sense wires (anodes) alternate with pairs of wires at ground potential. These *potential wires* largely decouple the field around the sense wires from the drift field, so that the voltages of the drift and sense wires can be optimized almost independently. The potential wires also reduce cross-talk between anodes.

A measurement of the z coordinate of a hit is obtained from the CJC using charge division, with a resolution of about 22 mm ($\sim 1\%$ of the wire length). To give a more accurate measurement of z (with a resolution of about 300 μm), and hence of θ, additional drift chambers are located before and after CJC1: the central inner and outer z chambers (CIZ and COZ). These have wires arranged azimuthally around the beam pipe, so that z is the drift coordinate and ϕ is determined with coarser resolution by charge division. The cross sections of the CIZ and COZ are respectively 16- and 24-sided regular polygons. Each is divided in z into drift cells (15 and 24 in the CIZ and COZ respectively), each containing four sense wires.

Immediately before the CIZ and after the COZ are located respectively the central inner and outer proportional chambers (CIP and COP). These give a signal very quickly after the bunch crossing and are used by the first level trigger (see section 4.8) to recognize events with tracks originating from a vertex in the interaction region. The CIP and COP each consist of three concentric cylinders separating two layers of anode wires parallel to the beam axis. Signals are read out

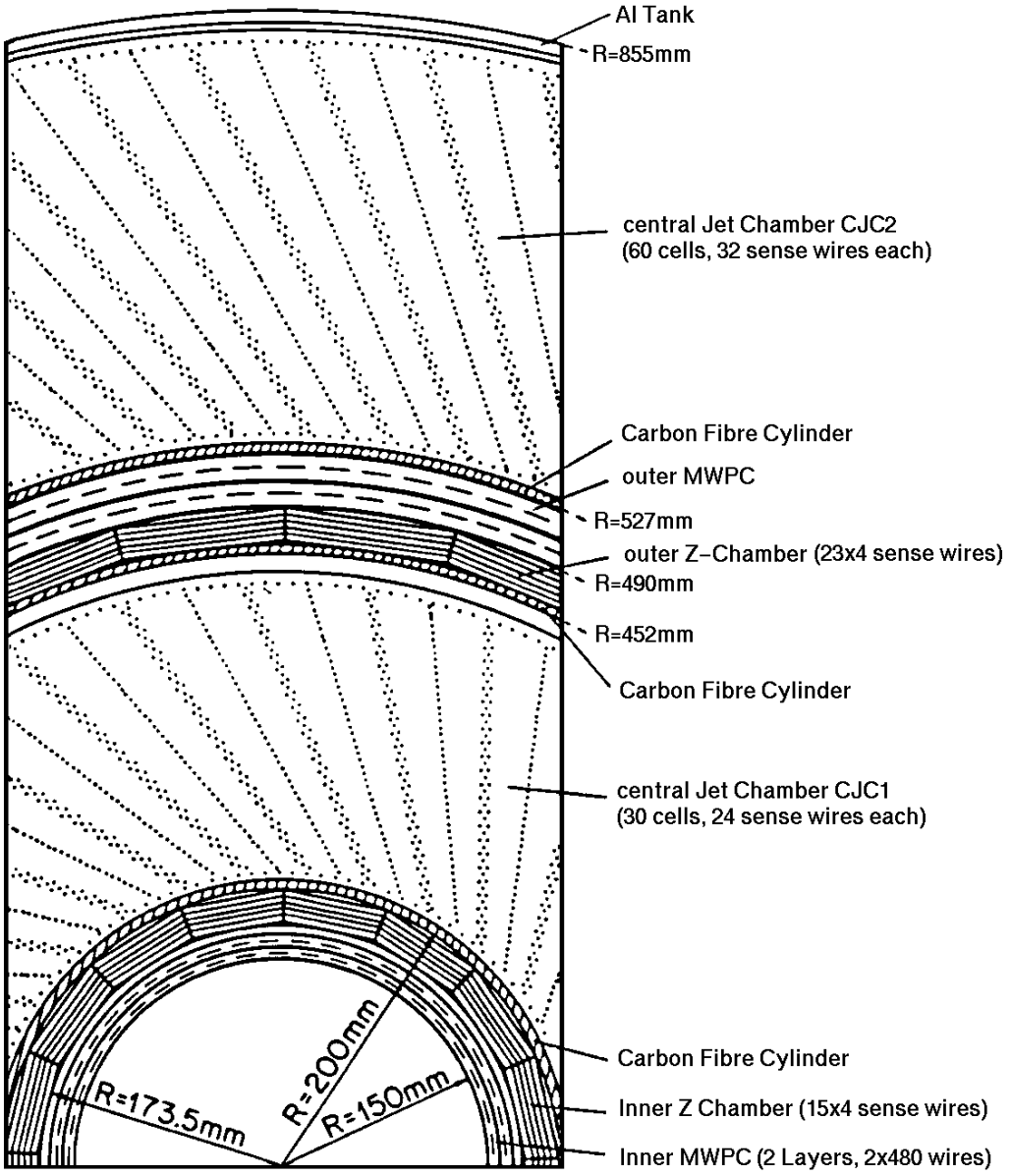

Figure 4.5: Transverse section of the central tracking system.

from the segmented outer cathode of each layer.

The Forward Tracker

The forward tracker [3] covers the region $5° < \theta < 25°$. The shallow angle of forward tracks means that they are best measured using several planes of detectors perpendicular to the beam axis, spaced out in z. The forward tracker consists of three similar supermodules (see figure 4.4), each 422 mm long in z, with the first starting at $z = 1290$ mm. Each supermodule consists of, in order of increasing z:

- three layers of planar drift chambers with different orientations for track reconstruction;
- a forward proportional chamber (FPC) for triggering;
- a passive transition radiator;
- a radial drift chamber, which in addition to tracking information provides some particle identification by detecting transition radiation as well as ionization from the charged particle itself.

Each layer of planar chambers consists of 32 parallel cells, each 57 mm wide in the drift direction and 32 mm thick in z, containing four sense wires spaced 6 mm apart in z. The sense wires alternate with pairs of potential wires, as in the CJC. The three layers of planar chambers within a supermodule are oriented at 60° to one another in ϕ, providing uniform resolution in x and y.

Each FPC layer consists of two planes of vertical anode wires, sandwiched between three cathode planes. The signals are read out using azimuthal strips in the cathode planes, giving the best resolution in the radial coordinate and hence in θ. The cathode plane is divided radially into 20 strips, with widths increasing geometrically from 18 mm for the innermost to 37 mm for the outermost strip. The outer four cathode rings are divided into sectors each covering 22.5° in ϕ, while the rest of the rings are divided into sectors covering 45° each. To improve the spatial resolution, the cathode strips in the second plane are displaced by half a strip width radially and by half a strip length azimuthally with respect to those in the first plane.

Each layer of radial chambers consists of 48 drift cells, each covering 7.5° in ϕ and containing 12 sense wires radiating out from the beam pipe, spaced 10 mm

apart in z, alternating with potential wires. The potential wires lie in a plane bisecting the cell, while the sense wires are staggered alternately 287 μm to each side of this plane. Several cathode strips are arranged on the walls of the cell to provide a uniform drift field. The gas used was changed after 1994 to one containing xenon, which has a large photoionization cross section, making it suitable for detecting the X-rays produced in the transition radiators. The transition radiators themselves comprise layers of polypropylene alternating with a mixture of helium and ethane gas. A thin mylar window separates the gas volumes of the transition radiator and the radial chamber, while allowing X-rays to pass through.

The Backward Proportional Chamber

The backward proportional chamber (BPC) is situated immediately in front of the BEMC (see section 4.4). It is the only tracker covering the backward region and is particularly important for detecting the scattered electron in low-Q^2 DIS events. It provides a good measurement of the point of entry of the electron into the BEMC and enables electrons to be distinguished from photons (which give a similar shower in the BEMC, but no hit in the BPC).

The BPC consists of four planes of anode wires alternating with five cathode planes. The wires are horizontal, vertical and at $\pm 45^\circ$ in the four layers. The cathodes are not segmented; signals are read out from the anode wires.

4.4 Calorimetry

The calorimeters in H1 are situated inside the solenoid in order to minimize the amount of dead material in front of them, which would otherwise degrade the energy measurement. Several different calorimeters are used to provide a good angular coverage and efficient identification of the scattered electron.

The Liquid Argon Calorimeter

The main system for measuring energy flow in H1 is the liquid argon calorimeter (LAr), which covers the range $4^\circ < \theta < 153^\circ$. The liquid argon technique was chosen for its stability, homogeneity and ease of calibration, and because the calorimeter can be finely segmented, enabling the separation of e- and π-initiated

showers. It is divided radially into two parts: the electromagnetic section [4] and the hadronic section [5]. Each section consists of alternate layers of liquid argon and metal absorbing plates. The metal plates are connected to the high-voltage supply, generating a field of 625 V/mm in the liquid argon gaps, which causes electrons released in ionization of the argon to be collected on the positive plates, producing a pulse which is amplified and read out by an analogue electronic system. The absorbing plates in the electromagnetic section are lead sheets 2.4 mm thick, sandwiched between sheets of fibreglass for mechanical support. For the much larger plates in the hadronic section, stainless steel is used because of its greater rigidity; the total thickness of the steel in each sampling layer is 19 mm. The total thickness of material traversed by a particle in the LAr depends on its direction, but is in the range 20–30 radiation lengths (X_0) in the electromagnetic section and 5–8 interaction lengths (λ) in total.

The LAr is non-compensating: its response is about 30% smaller for hadronic showers than for electromagnetic ones. However, its fine granularity makes it possible to differentiate between the two types of shower and apply a correction factor to compensate for this difference. The energy resolution has been measured in electron and pion test beams and the results found to be consistent with the observed behaviour in H1. The resolution for electrons was found to be $\frac{\sigma_E}{E} \approx \frac{11\%}{\sqrt{E}} \oplus \frac{15\%}{E} \oplus 1\%$ and for pions $\frac{\sigma_E}{E} \approx \frac{46\%}{\sqrt{E}} \oplus \frac{73\%}{E} \oplus 3\%$, where E is in GeV.

The Backward Electromagnetic Calorimeter

The Backward Electromagnetic Calorimeter (BEMC) [74] [12] (figure 4.6) detects electrons scattered at angles of 4–17°, thus covering the region of low-Q^2 DIS – approximately 4 GeV^2 $< Q^2 <$ 100 GeV^2. The BEMC is a segmented lead-scintillator calorimeter. It is divided into 88 stacks, each comprising 50 pairs of alternate layers of plastic scintillator and lead. Read-out is via wavelength shifters (WLS) extending along the sides of the stacks and feeding into photodiodes at the rear of the detector. Two opposite sides of each square or trapezial stack are covered by long WLS, extending the full length of the stack. The last 15 layers are also read out using shorter WLS on the remaining two sides; the division of the signal between the layers provides a measure of the longitudinal profile of the energy deposition.

The thickness of the BEMC is 21.7 radiation lengths, which is only about one interaction length. A hadron typically leaves only 45% of its energy in the BEMC, but the BEMC output can be combined with the tail-catcher behind it to give a hadronic energy resolution of $\frac{\sigma_E}{E} \approx \frac{80\%}{E}$. The resolution for electromagnetic

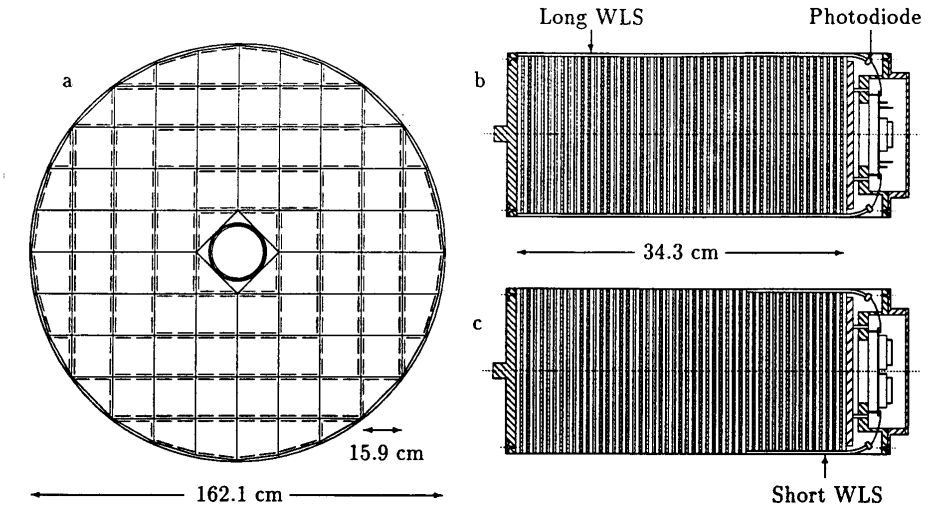

Figure 4.6: The BEMC: (a) Transverse view of the BEMC barrel, showing the division into stacks. The orientation of the long WLS in each stack is shown. (b) Longitudinal section of a stack. (c) Longitudinal section of a stack in a plane perpendicular to (b).

energy is found by analysing the kinematic peak of the scattered electrons to be $\frac{\sigma_E}{E} \approx \frac{10\%}{\sqrt{E}} \oplus \frac{39\%}{E} \oplus 2\%$.

The Plug Calorimeter

The plug calorimeter [13] fills the gap in acceptance between the edge of the LAr at $\theta \approx 3.5°$ and the beam pipe at $\theta \approx 0.6°$. It is used to reduce the amount of transverse momentum lost through particles escaping undetected close to the direction of the beam pipe, and to aid in identifying diffractive events by detecting energy flow in the very forward direction, near the diffracted proton or proton remnant.

The plug contains eight layers of silicon detectors, alternating with layers of copper. Its design energy resolution of about $150\%/\sqrt{E}$ is limited by energy leakage and by the relatively high amount of dead material separating it from the interaction point. The actual resolution is worse than this and has been degraded by radiation damage of the silicon detectors.

The Tail-Catcher

The pad electrodes attached to eleven of the sixteen layers of limited streamer tubes in the instrumented iron return yoke (see section 4.5) are also used as a tail-catcher for the calorimeter system. This provides a measure of the amount of energy leaking out of the other calorimeters due to late-developing hadronic showers.

4.5 Muon Detection

Muons can be identified by the fact that they travel long distances in matter without showering. This is because they are heavier than electrons, which means that they do not lose as much energy by bremsstrahlung. Thus a particle which leaves a trail of ionization in detectors placed outside the calorimeters, having traversed many radiation lengths of material, is likely to be a muon.

The Instrumented Iron

The iron yoke which carries the returning magnetic flux from the solenoid is instrumented with limited streamer tubes (LSTs), which make up the central muon system, covering the range $6° < \theta < 172°$. The iron is segmented into ten layers, interleaved with layers of LSTs. Additional LSTs are located before and after the iron to give a total of sixteen LST layers.

The LSTs are oriented in the z direction in the barrel and in the x direction in the end-caps. They have a cross section of 10×10 mm and give a resolution of 3–4 mm in the coordinate perpendicular to the wires. Five of the layers are also equipped with cathode strips perpendicular to the wires, giving a resolution of 10–15 mm in the second coordinate. The remaining eleven layers have cathode pads, giving a two-dimensional point with a resolution of about 10 cm. The wires and strips are read out by a digital system, while the pads are read out by the same analogue system as the LAr calorimeter. The signals from the pads are used to provide a measurement of the tails of hadronic showers leaking out of the LAr calorimeter and BEMC (see section 4.4), as well as forming part of the muon system. Track reconstruction in the forward muon system starts with the wires; then information from the strips is added to form a track in three dimensions. The pads are used if necessary to resolve ambiguities.

The Forward Muon Detector

The instrumented iron is supplemented in the forward direction by the Forward Muon Detector (FMD) (figure 4.7), which measures the momentum of high-energy muons in the range $3° < \theta < 17°$. The kinematics of HERA events mean that there are many high-energy muons in this region, as well as a large background from other high-energy particles and secondary scattering from the beam pipe, magnets and associated material. The FMD can only detect muons with a momentum above about 5 GeV, since a significant amount of energy (typically 3 GeV) is lost by a muon in the material between the interaction point and the FMD.

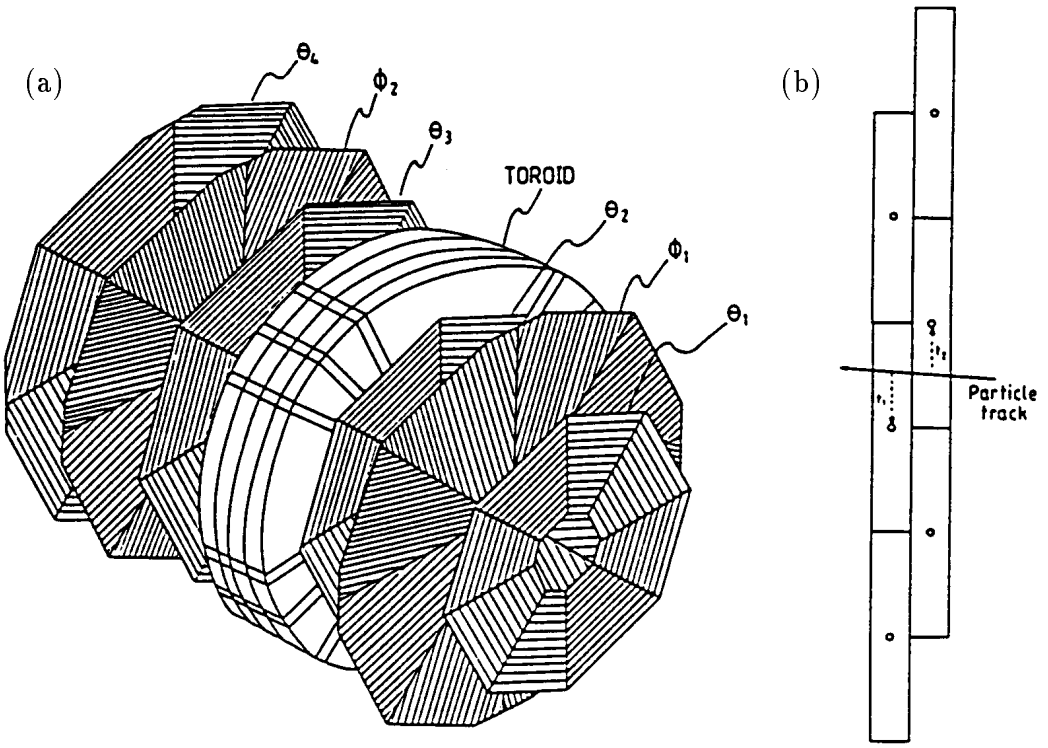

Figure 4.7: The Forward Muon Detector: (a) Schematic view, showing the orientation of the drift cells in each plane. (b) Cross section of a double layer of drift cells.

The FMD comprises six planes of drift chambers – three on each side of a toroidal magnet. Each plane consists of a double layer of 12-cm-wide cells, staggered by half a cell width to enable left-right ambiguities to be resolved (as shown in figure 4.7(b)). Four of the planes – numbers 1, 3, 4 and 6 – are arranged with cells oriented azimuthally around the beam pipe in order to measure θ accurately. The

other planes – numbers 2 and 5 – are arranged with cells pointing out radially from the beam pipe in order to measure ϕ accurately. In each case, charge division is used to obtain a less precise measurement of the other coordinate.

Tracks are formed in several stages. Firstly, hits in the two layers of a plane are combined to form pairs, provided that the hits in a pair point roughly towards the interaction point. The drift-coordinate ambiguity is resolved at this stage. Secondly, hit pairs are combined to form *segments* in the pre- and post-toroid layers separately. (Unpaired hits may also be used at this stage.) A pre-toroid and a post-toroid segment are then combined to form a track. The difference in direction between the pre- and post-toroid segments, due to bending in the toroid, is a measure of the momentum of the muon. This momentum determination works up to about 200 GeV, where the track is too straight for the direction of the bending, and hence the charge of the muon, to be determined.

The FMD has also proved to be sensitive to secondary particles produced by scattering of the proton remnant on the beam pipe and surrounding material. This makes it useful in recognizing diffractive events in which the proton scatters elastically or nearly elastically.

4.6 Luminosity Measurement

The luminosity of the colliding beams, which must be known in order to make any measurement of the cross section for a process, is measured at H1 using the Bethe-Heitler process $ep \to ep\gamma$, the cross section for which is known very accurately. The photon and the scattered electron in the final state are detected using detectors designed specifically for this purpose. The positions of the electron tagger (ET) and the photon detector (PD) are shown in figure 4.8.

The electron tagger is situated at $z = -33.4$ m; the scattered electron leaves the beam pipe through a window at $z = -27.3$ m after being deflected from the beam axis by a bending magnet. The photon passes through a window at $z = -92.3$ m, where the proton beam pipe bends upwards, and hits the photon detector at $z = -102.9$ m. The photon detector is preceded by a layer of lead to protect it from synchrotron radiation, and a veto counter to reject events in which a photon has converted in the lead.

The electron tagger and photon detector are two similar calorimeters, each

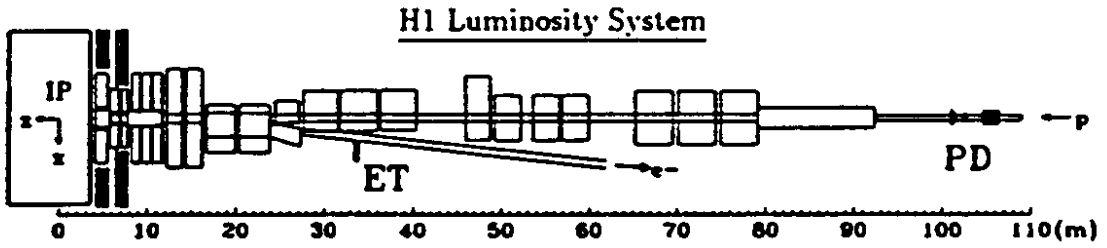

Figure 4.8: The luminosity system, showing the position of the electron tagger (ET) and photon detector (PD).

consisting of an array of crystal Cherenkov counters. They are calibrated continuously during data-taking using the fact that the sum of the energies of the photon and the scattered electron is equal to the energy of the electron beam. The veto counter is a water Cherenkov detector.

The largest background to the Bethe-Heitler process is bremsstrahlung from residual gas in the beam pipe: $eA \rightarrow eA\gamma$. This effect is measured using the unpaired electron pilot bunches, which are subject to scattering on gas molecules, but not on the proton beam. The formula used is

$$\mathcal{L} = \frac{R_{tot} - (I_{tot}/I_0)R_0}{\sigma_{vis}} \tag{4.1}$$

where $\mathcal{L}$ is the luminosity, R_{tot} and R_0 are respectively the total rate of tagged events and the rate from pilot bunches, and I_{tot} and I_0 are respectively the total current of the electron beam and the current carried by the pilot bunches. The visible cross section σ_{vis} includes factors from the acceptance and efficiency of the luminosity system. The acceptance depends sensitively on the beam crossing angle, which varies slightly from run to run. A correction is made for this effect in the on-line measurement, and more accurately in the off-line measurement.

The luminosity can be measured using two different methods. For the on-line luminosity measurement, which must be available in real time for beam monitoring and for tuning to optimize luminosity, the most important consideration is a rapid measurement with a small statistical error. For this, a coincidence method is used: the photon and electron must both be detected. For the off-line measurement, where it is important to reduce the systematic error due to the dependence of the acceptance on the beam crossing angle, only the photon detector is used, but a higher energy threshold is applied.

Apart from measuring the luminosity, the luminosity system is also used in studying photoproduction. An electron scattered at a small angle ($Q^2 < 0.01$ GeV^2) may be detected by the electron tagger; the photon detector and veto counter are used to reject events where a photon is also found. The measurement of the electron energy by the tagger allows kinematic reconstruction of the event.

4.7 Scintillators

The Time-of-Flight Counters and Veto Walls

The time-of-flight (ToF) counters and veto walls are sheets of scintillator which, with their fine time resolution, provide a way of distinguishing between ep events and beam-induced background, and are used by the L1 trigger. The backward ToF (BToF) counter consists of two planes at $z = -1.95$ m and $z = -2.25$ m, each covering about 127×127 cm in the xy plane. The forward ToF (FToF) [75] counter is a similar, but smaller arrangement at $z \approx 7$ m. There are two veto walls: an inner wall of 100×90 cm at $z = -6.5$ m and an outer wall of 5×4 m at $z = -8.1$ m. Particles associated with background induced upstream of the detector by the proton beam hit the BToF at the same time as the proton beam passes. Particles associated with an ep interaction pass at the same time as the electron beam, 13 ns later. The time resolution of a few nanoseconds provided by the scintillators is sufficient to distinguish between the two. The purpose of the veto wall is to detect penetrating charged particles (mainly muons) associated with the proton beam. The FToF functions in a similar way to the BToF, allowing separation of ep events from background induced by the electron beam.

The Proton-Remnant Tagger

The proton-remnant tagger (PRT) (figure 4.9) consists of seven scintillators arranged around and between the electron and proton beam pipes at a position $z = 24$ m, downstream from the centre of H1. A proton that dissociates at the interaction point to form a low-mass state will produce several remnant particles at small angles to the incident proton direction. The PRT is designed to detect this proton remnant and so distinguish such events from those in which the proton is scattered elastically.

Each scintillator (0–6) in figure 4.9 actually consists of two parallel sheets

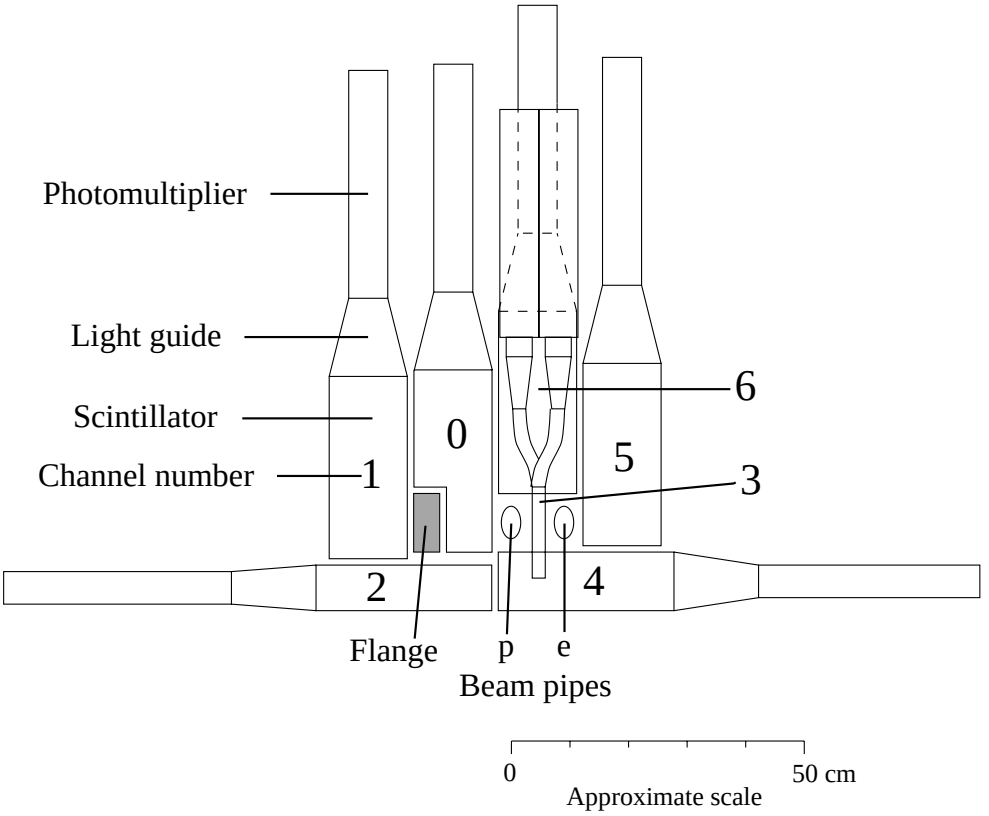

Figure 4.9: Schematic diagram of the proton remnant-tagger (PRT), looking towards the interaction point.

of plastic scintillator with separate photomultipliers and pulse-height discriminators. The signals from such a pair of channels are fed into a coincidence detector, which only registers a signal if both produce a pulse within 15 ns of each other and a *gate* signal is received, indicating that the signal is within the time window expected for a proton remnant from an *ep* interaction in the detector.

4.8 Triggering and Read-out

The task of the trigger is particularly demanding for a detector at HERA, where the bunch-crossing rate is extremely high at 10.4 MHz. That means that bunches of electrons and protons intersect in the centre of the H1 detector once every 96 ns, and a decision must be made each time on whether to read out the detector.

The process of reading out the detector takes about 1 ms, which means that once the decision has been made to read out an event, the detector will miss any further events taking place in the next 10^4 bunch crossings. It is therefore important to have a trigger that will make a fast decision, rejecting a large proportion of bunch crossings before reading out begins.

Detector output related to a given bunch crossing does not become available until several bunch crossings later. The maximum drift time in some drift chambers is about 1 μs; the integration time for preamplifiers ranges up to 1.5 μs; and even the time taken by a signal to propagate along a cable from one end of the detector to the other is not negligible in comparison with the bunch-crossing interval.

These restrictions mean that a pipelined read-out system must be used in order to preserve all subdetector information until the first-level trigger reaches a decision. The decision signal, L1KEEP, is available 24 bunch crossings after the corresponding *ep* interaction. Some additional time is required for this signal to reach the subsystems, so pipelines range from 27 to 35 bunch crossings in length. Figure 4.10 illustrates the flow of data in the trigger and read-out system.

The first-level (L1) trigger is based on a number of different trigger systems, each based on one subdetector or a set of subdetectors (e.g. the central and forward proportional chambers). Each trigger system produces a set of *trigger elements*, based on the pattern of signals from the subdetectors, indicating for example a vertex reconstructed by the proportional chambers, a charged track in the CTD,

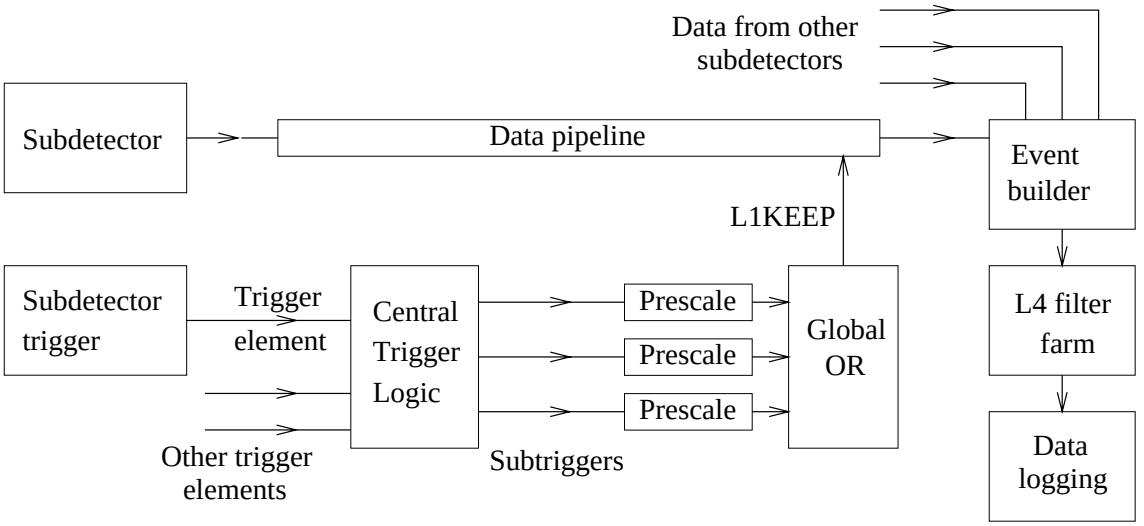

Figure 4.10: Data flow in the H1 trigger and read-out system.

or a muon in the instrumented iron or FMD. The BEMC trigger elements, which recognize the scattered electron in low-Q^2 DIS and are particularly important in this analysis, are described in more detail in section 5.2. The central trigger logic (CTL) combines several trigger elements to produce each of 128 *subtriggers*, tailored to particular physics channels. Some subtriggers fire so frequently that the dead time of the read-out would become too high if the event were read out every time, so they are *prescaled*: only every Nth trigger, where N can be adjusted, is allowed to pass. This introduces a large but precisely known correction factor into the efficiency for the subtrigger in question.

Some subtriggers are not designed for physics analysis, but are *monitor* triggers. They are used to study the efficiency of the *physics* triggers – those used directly for analysis. There is also a random trigger, which does not depend on any other trigger elements, and is used for studies of detector noise.

Once a positive L1KEEP signal has been received, the subdetector pipelines are stopped and the process of reading out the data from them begins. This takes 1–2 ms, although the next two levels of trigger electronics – L2 and L3 – will in future be able to reject an event within this time, aborting the read-out after 20–800 μs and thus further reducing the dead time.

The fourth-level trigger – the L4 filter 'farm' – consists of software running on a set of up to 32 MIPS R3000 processors. It has the data from all subdetectors available to make its decision and can reconstruct tracks, calorimeter clusters etc. using some of the subroutines of the off-line event-reconstruction package H1REC.

The L4 farm applies cuts to reject beam-gas, beam-wall and cosmic-ray events. It also rejects events triggered by noise in the subdetector triggers, using reconstructed quantities to verify the L1 trigger decisions. The algorithm used in 1994 is described in [76]. Approximately 70% of events accepted by L1 – mainly beam-gas interactions and events with a vertex outside the central region – are rejected by the L4 farm.

4.9 Event Reconstruction

Event reconstruction involves combining the raw data from the subdetectors, i.e. individual hits in wire chambers and calorimeter cells, to form tracks and clusters of deposited energy. Reconstruction is performed by an 18-processor SGI Challenge computer in a 'quasi-online' way: the process runs continuously, but is typically a few hours or days behind the data acquisition during luminosity running. An event takes on average 1.5 s to reconstruct on one processor, so the computer can match the nominal data-logging rate of 10 Hz. The reconstructed data is written to magnetic tape, and a subset of the data, in a reduced *data summary tape* (DST) format, is written to disk, where it is easily accessible for off-line analysis.

4.10 Simulation

It is important when analysing data from a particle physics experiment such as H1 to be able to model and understand the behaviour of the detector. The efficiency for detecting and reconstructing a particular particle or type of event must be known in order to measure the cross section, and it is estimated using a computer simulation. Such a simulation takes as its input a list of particles produced at the interaction point in a Monte Carlo generated event, together with the direction and momentum of each one. The output should be as close as possible to the data that would be read out should such an event actually take place in the detector.

The H1 detector simulation program, H1SIM, consists of three stages. The first stage uses the GEANT package [77] to model the processes by which particles produced in an ep interaction interact with the detector as they travel out from the interaction point. The output of this stage is a list of detector components crossed, with the coordinates of the entry and exit points and the amount of energy deposited. This is the most time-consuming part of the simulation, taking typically 200 s for a low-Q^2 DIS event.

The next stage, DIGI, takes the output of the GEANT step and converts it into hits in the same data format as is used for data from the real detector. This can then be used as input for the event reconstruction package H1REC to produce reconstructed Monte Carlo events, which can be processed by the same analysis software as is used for data. The separation of the GEANT and DIGI stages means that the simulation can be repeated for different detector conditions by steering DIGI appropriately, without repeating the time-consuming GEANT step.

The third stage, TRIG, simulates the response of the H1 trigger system, using input from the previous stages of H1SIM. The output of this stage is a list of trigger elements which would fire if such an event occurred in the H1 detector.

Chapter 5

Event Selection

5.1 The Data Sample

The data used in this analysis were recorded during the 1994 running period when HERA was colliding positrons at 27.5 GeV with protons at 820 GeV. Only events recorded during periods when the high-voltage and read-out systems of all necessary subdetectors were working are used. This means the central tracker, the liquid argon calorimeter, the BEMC, the BPC, the plug calorimeter, the forward muon detector, the proton-remnant tagger, the time-of-flight scintillators and the luminosity system. The integrated luminosity remaining after these restrictions have been applied is 2.23 pb^{-1}.

5.2 Triggering of DIS Events

The events used in this analysis were triggered by the low-Q^2 DIS subtriggers, based on the backward electromagnetic calorimeter (BEMC, described in section 4.4). Most events were triggered by the standard BEMC DIS subtrigger, s0, which depends on the BEMC single-electron trigger (BSET) and the time-of-flight systems, and is described below.

5.2.1 The BEMC Single-Electron Trigger

The analogue signals from the long wavelength shifters in each BEMC stack are added together to give a signal for the whole stack. This gives a rather coarser granularity than is achieved at a later stage in the cluster reconstruction, but it is sufficient for triggering. The stacks do not all have the same response, since the various stack shapes have different optical properties, so they are equalized to the same energy scale by applying an adjustable gain to each one. Adjustable delays are used to synchronize the signals.

The signal from each stack is compared with two different thresholds. The higher threshold, $HT \approx 2.3$ GeV, rejects fake hits generated by noise and selects stacks with a significant deposit of energy to act as 'seeds'. Each seed stack is combined with those neighbouring stacks with signals above the lower threshold, $LT \approx 1.3$ GeV, to form a cluster.

There are three trigger elements based on the energy of these clusters; if the total energy of the clusters in an event exceeds one of the three thresholds $CL1$, $CL2$ or $CL3$, the corresponding trigger element is set. There are also trigger elements based on the number of clusters (exactly one cluster or more than one) and the total energy of all stacks above the noise threshold LT. The total energy of the clusters and the energy of all stacks above LT are also digitized and sent to the central trigger logic for use by other calorimeter-based subtriggers.

One major source of background in these trigger elements is the nuclear counter effect – the process whereby an ionizing particle enters one of the photodiodes and gives rise to a signal directly, rather than by showering in the lead-scintillator stack. A major cause of this is synchrotron radiation. Nuclear-counter events can be recognized by the fact that there tends to be a large signal from one photodiode in a stack, but no significant signal from the other photodiodes. The majority of this background comes from the innermost 16 stacks, nearest the beam, which are hit by the most synchrotron radiation. These are equipped with dedicated electronics to detect such *single-diode events*. The smaller number of single-diode events in the outer stacks are rejected by the L4 farm.

5.2.2 The Time-of-Flight Triggers

The `ToF_IA` (interaction) and `ToF_BG` (background) trigger elements depend on the timing of signals from the backward time-of-flight system (BToF, described in section 4.7). A coincidence detector combines signals from the two scintillator planes, and the resulting signal can cause one of the two trigger elements to fire, depending on its timing. The background time window starts 18 ns before the peak of the background distribution and lasts for 25 ns; the interaction time window starts 1 ns after the end of the background window and lasts for 13 ns. The background peak comes mainly from beam-gas and beam-wall interactions, while the peak in the interaction window is mainly due to synchrotron radiation.

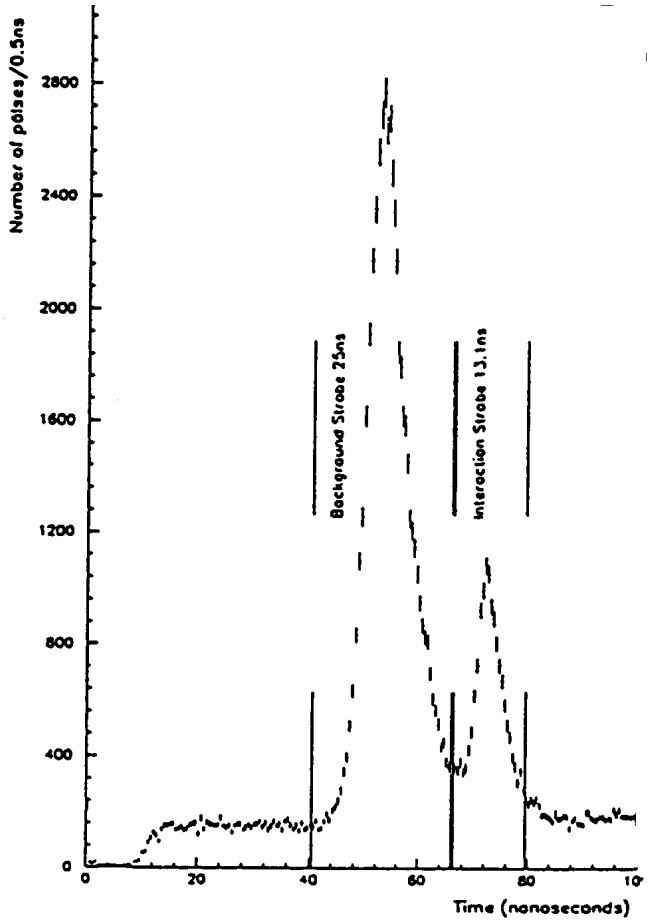

Figure 5.1: Time distribution of hits in the BToF. Taken from [73].

The forward time-of-flight (FToF) trigger elements work in a similar way. The interaction time window covers the period from 10 ns before to 10 ns after the centre of the proton peak, when particles associated with the proton beam pass

through the FToF. The background time window is 35 ns in length, starting as the interaction window ends and extending to the beginning of the electron peak.

5.2.3 Combining the Trigger Elements

Subtrigger s0 is formed from a combination of six trigger elements as follows:

```
BSET_CL2 and (not (BSET_EQ1IN and BSET_SDE)) and
  (not ToF_BG) and (FToF_IA or (not FToF_BG)).
```

To be selected by this subtrigger, an event must cause the trigger element `BSET_CL2` to fire, meaning that the total energy of all clusters in the BEMC exceeds the threshold $CL2$, which is approximately 7 GeV (value at 50% efficiency). The trigger element `BSET_EQ1IN` selects events with exactly one cluster in the inner sixteen stacks, while `BSET_SDE` selects events in which a single-diode signal is detected in at least one of these stacks. The requirement `not (BSET_EQ1IN and BSET_SDE)` thus rejects events where there is only one cluster in the inner part of the BEMC and this cluster is flagged as background from the nuclear counter effect.

Subtrigger s0 also require that there is no signal from the BToF in the background time window, and it rejects an event if there is a signal in the FToF background window but none in the interaction window.

For events in the kinematic range used in this analysis and having a scattered positron of energy greater than 10 GeV, the efficiency of this subtrigger has been determined using data to be greater than 99% [21]. Thus no correction needs to be made for trigger inefficiency, and the systematic error from this source is negligible in comparison with the dominant errors detailed in chapter 6.

During a small fraction of the 1994 running period, a prescale was applied to subtrigger s0, this being equivalent to a reduced efficiency for these periods. However, since events triggered by other subtriggers are also accepted for this analysis, the actual drop in the overall trigger efficiency is small, especially when averaged over the entire running period.

5.3 Selection of DIS Events

5.3.1 The Event Vertex

Detectors at HERA suffer from a high rate of background events from interactions of the proton beam with gas molecules and with the walls of the beam pipe upstream of the detector. These events produce large numbers of tracks that do not point to a vertex in the centre of the detector. To reduce this background, events without a reconstructed vertex in the central region are rejected. The cut used is

$$|z - \bar{z}| < 30 \text{ cm}, \tag{5.1}$$

where $\bar{z} = 5$ cm is the mean vertex position.

5.3.2 The Positron Candidate

Positron candidates are identified in H1 using the BEMC for low-Q^2 DIS (about 4 GeV^2 $< Q^2 <$ 100 GeV^2) and the liquid argon calorimeter (LAr) for higher Q^2. A pion can sometimes produce an energy cluster which looks like the signature of a positron, so various cuts are applied to reject such events. The candidate with the highest energy is taken to be the best, since the background from pions peaks at low cluster energy. For the purposes of this analysis, an event is only accepted if the best positron candidate is in the BEMC and passes the following cuts:

- Energy of the cluster:
  The reconstructed energy of the positron candidate, E'_e, must be greater than 10 GeV.

- Position of the cluster in the BEMC:
  Clusters that are very close to the inner edge of the BEMC, with the risk that some of the energy of the shower may be missed, are rejected by the cut $|x_{BPC}| + |y_{BPC}| > 18$ cm, where x_{BPC} and y_{BPC} are the coordinates of the BEMC positron candidate when projected into the plane of the BPC. Clusters in the central region of the BEMC, which suffers from high background, are rejected by the cut $r_{BPC} > 16$ cm, where $r_{BPC} = \sqrt{(x^2_{BPC} + y^2_{BPC})}$.

- Size of the cluster:
  The lateral profile of a cluster in the BEMC can be used to discriminate against

pion-induced background. Positrons produce localized showers, concentrated in one or two stacks, while hadronic showers tend to be broader. The cut used is $R_C < 3$ cm, where R_C is the energy-weighted cluster radius:

$$R_C = \frac{1}{E_C} \sum_{i=1}^{n} E_i \cdot |\boldsymbol{r}_i - \boldsymbol{r}_c| \tag{5.2}$$

where E_C and $\boldsymbol{r_c}$ are respectively the energy and centre of gravity of the cluster, and E_i and $\boldsymbol{r_i}$ are respectively the energy and centre of gravity of the deposit in the ith of the n stacks forming the cluster.

- Hit in the BPC:
  There must be a hit in the BPC within 3 cm of the centre of gravity of the BEMC cluster. This reduces the background from photons, which produce an electromagnetic shower in the BEMC without leaving a signal in the BPC.

- Angle of the scattered positron:
  The reconstructed polar angle of the scattered positron from the event vertex must lie in the range $155° < \theta < 173°$.

5.3.3 Kinematic Reconstruction

The kinematic range within which the event acceptance is high enough for a cross-section measurement to be made is determined by the available range in the energy and scattering angle of the positron. This range is determined by the cuts described above. The acceptance of these cuts is shown as a function of the kinematic parameters Q^2 and y in figures 5.2 and 5.3 respectively. Two additional cuts are applied to the reconstructed kinematic variables in order to restrict events to the region where the acceptance is reasonably high:

$$10 \text{ GeV}^2 < \quad Q^2 \quad < 100 \text{ GeV}^2 \tag{5.3}$$

$$0.06 < \quad y \quad < 0.6. \tag{5.4}$$

The range in Q^2 is determined by the acceptance and behaviour of the BEMC. Above $Q^2 \approx 100$ GeV^2, the scattered positron misses the BEMC, hitting the liquid argon calorimeter instead. Below $Q^2 \approx 10$ GeV^2, genuine positrons in the BEMC begin to be diluted by increasing numbers of 'fake' positrons – largely pions from the many photoproduction events. The upper limit on y is set by the cut on the energy E'_e of the scattered positron. For y larger than about 0.6, this energy is typically less than 10 GeV. The lower limit on y is not determined by the acceptance of the DIS event selection, but by the requirement that there be a $D^{*\pm}$ in the central region of

the detector (see chapter 6). The smaller the value of y, the more the hadronic final state is boosted along the proton direction and the less likely it is that any $D^{*\pm}$ produced will lie within the acceptance of the central tracker.

The kinematic quantities Q^2 and y are reconstructed using the Σ method [78], which works accurately over a large range. The formulae used are as follows:

$$\Sigma = \sum_h (E_h - p_{z,h}) \tag{5.5}$$

$$y_\Sigma = \frac{\Sigma}{\Sigma + E(1 - \cos\theta'_e)} \tag{5.6}$$

$$Q^2_\Sigma = \frac{E^2 \sin^2\theta'_e}{1 - y_\Sigma} \tag{5.7}$$

$$x_\Sigma = \frac{Q^2_\Sigma}{s y_\Sigma} \tag{5.8}$$

Figure 5.4 illustrates the resolution achieved using the Σ method on Monte Carlo events generated by RAPGAP with hadronization simulated using the colour-dipole model (CDM). The RMS resolution is 20% in y and 17% in Q^2.

5.4 Selection of Diffractive Events

The signature of a diffractive event is a 'rapidity gap' – a region of pseudo-rapidity between the proton-remnant system and the rest of the final state in which no hadrons are produced, as explained in chapter 3. In this analysis, the aim is to select diffractive events in which the proton is elastically scattered or forms only a low-mass state. In such events, the rapidity gap extends a long way in the forward direction – almost up to the proton beam direction. There are several detectors in this region, which are used to detect energy flow and thus veto non-diffractive or proton-dissociation events. The choice of the various thresholds for activity in these detectors is discussed in more detail in [80].

5.4.1 The Forward Detectors

The Liquid Argon Calorimeter (LAr)

The quantity η_{max} is defined as the pseudorapidity of the most forward calorimeter cluster of at least 400 MeV, this threshold being chosen as a compromise

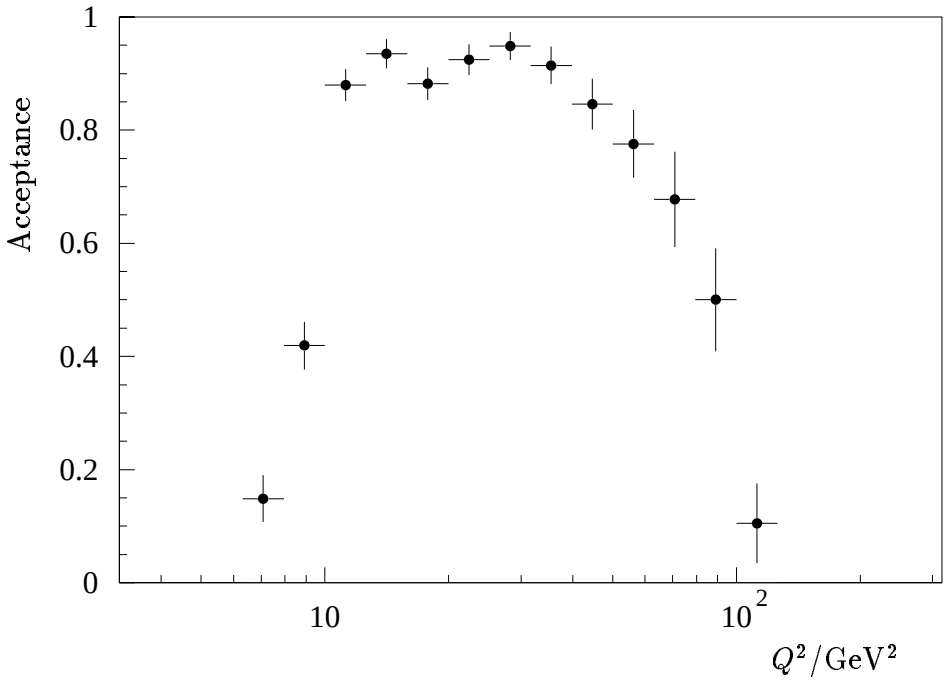

Figure 5.2: Acceptance of DIS event cuts plotted against Q^2 for diffractive events in the range $0.06 < y < 0.6$ containing one $D^{*\pm}$ in the region $|\eta| < 1.25$ and $p_\perp > 1$ GeV.

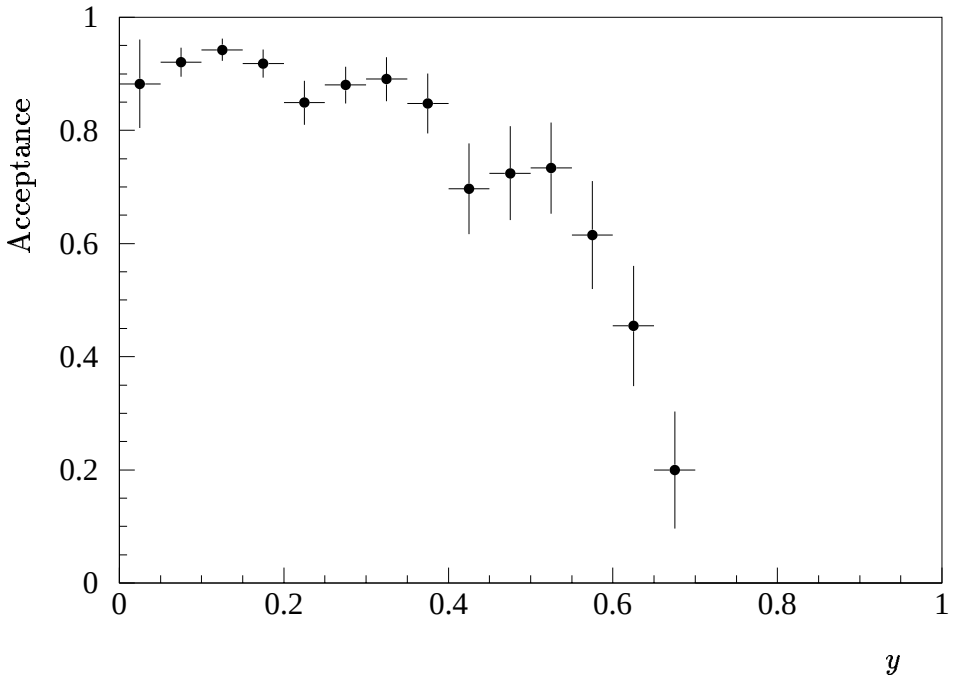

Figure 5.3: Acceptance of DIS event cuts plotted against y for diffractive events in the range 10 $\mathrm{GeV}^2 < Q^2 < 100$ GeV^2 containing one $D^{*\pm}$ in the region $|\eta| < 1.25$ and $p_\perp > 1$ GeV.

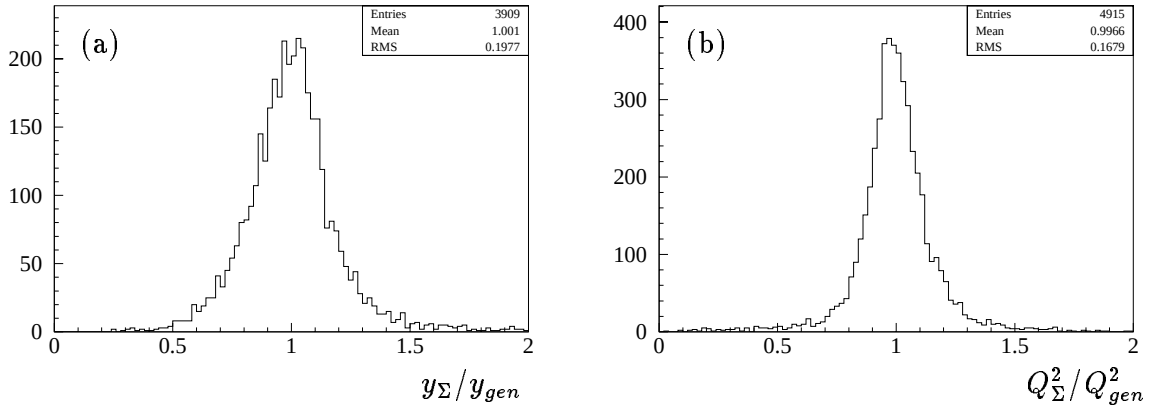

Figure 5.4: The resolution of the Σ method for events generated by the RAPGAP Monte Carlo [79]: reconstructed divided by generated values. (a) Resolution in y for events in the range 10 GeV$^2 < Q^2 <$ 100 GeV^2, $x_{I\!P} < 0.05$ and $|t| < 1$ GeV^2. (b) Resolution in Q^2 for events in the range $0.06 < y < 0.6$, $x_{I\!P} < 0.05$ and $|t| < 1$ GeV^2.

between efficiency and noise rejection. Clusters can be detected up to $\eta_{max} \approx 3.5$, at the forward edge of the LAr. The cut used is

$$\eta_{max} < 3.2. \tag{5.9}$$

The Proton-Remnant Tagger (PRT)

The PRT was designed specifically in order to veto proton-dissociation events by detecting particles in the very forward direction. Due to readout problems, only the first three channels are used in this analysis. If a hit is present in any of these three channels, the event is rejected.

The Plug Calorimeter

The plug calorimeter extends the acceptance of the calorimetry system in the forward region beyond the end of the liquid argon calorimeter. Although its energy resolution is not as good as that of the liquid argon calorimeter, it is still useful as a veto on events with significant amounts of energy in this region. A threshold of 7.5 GeV is chosen as a compromise between efficiency and noise rejection. If more than this amount of energy is detected in the plug, the event is rejected.

The Forward Muon Detector (FMD)

The FMD is designed to detect and measure high-energy muons in the forward direction. However, it has also proved to be sensitive to particles from the proton remnant that scatter from the beam pipe and surrounding material. If more than one pair of associated hits is detected in the pre-toroid part of the FMD, the event is rejected.

5.4.2 Kinematic Reconstruction

The fraction of the proton's momentum carried by the colourless exchange, $x_{I\!P} = (Q^2 + M_X^2)/(Q^2 + W^2)$, is reconstructed with a slightly better resolution using the alternative form

$$x_{I\!P} = \frac{\sum_{X+e'}(E + p_z)}{2E_p}, \tag{5.10}$$

where the sum is over the scattered positron and the hadronic final state, excluding the diffracted proton. The resolution achieved is illustrated in figure 5.5. The hadronic final state is reconstructed using a combination of tracks and calorimeter information. The rapidity of the hadronic system X is largely dependent on the value of $x_{I\!P}$, so there is a strong correlation between $x_{I\!P}$ and η_{max}. The cut $\eta_{max} < 3.2$ restricts the accessible range of $x_{I\!P}$ to approximately $x_{I\!P} < 0.05$, so a cut of $x_{I\!P} < 0.05$ is applied and the cross section is quoted for this range. The requirement of a small $x_{I\!P}$ and a clear rapidity gap ensures that the measurement covers the kinematic region where diffraction dominates, and any contribution from meson exchange is expected to be small.

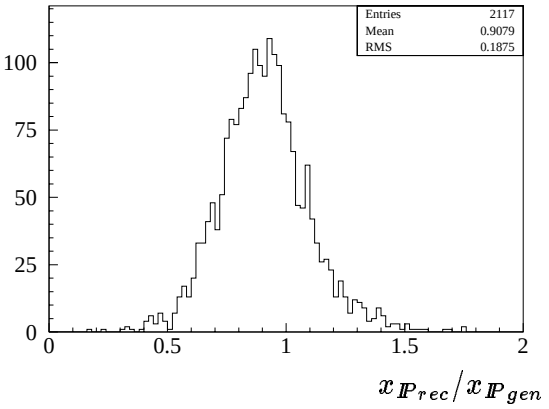

Figure 5.5: The resolution of the $x_{I\!P}$ reconstruction for events generated by RAPGAP: reconstructed divided by generated $x_{I\!P}$ for events in the range $0.06 < y < 0.6$, $10\ \text{GeV}^2 < Q^2 < 100\ \text{GeV}^2$, $|t| < 1\ \text{GeV}^2$ and $\eta_{max} < 3.2$.

Chapter 6

Measurement of the $D^{*\pm}$ Cross Section

6.1 Reconstruction of $D^{*\pm}$ Decays

The D^{*+} meson[1] is reconstructed in this analysis using the decay chain

$$D^{*+} \rightarrow D^0 \pi^+_{slow} \rightarrow (K^- \pi^+) \pi^+_{slow}. \tag{6.1}$$

The fact that the final state consists entirely of charged particles makes reconstruction using the tracking detectors relatively simple, and the low multiplicity – only three tracks – means that the inefficiency of the trackers introduces only a small correction to the cross section, and that the corresponding systematic error is also small.

The difference of 145.4 MeV between the D^{*+} and D^0 masses is only slightly larger than the π^+ mass. Thus the π^+ from the D^{*+} decay has only a small momentum (40 MeV) in the D^{*+} rest frame, and it is labelled π^+_{slow} in this thesis. Its momentum in the laboratory frame is therefore strongly correlated with the momentum of the D^{*+}, but smaller by a factor of approximately $M_{\pi^+}/M_{D^{*+}} = 0.07$. This tight kinematic constraint means that there is a strong correlation between the reconstructed invariant masses of the D^{*+} and the D^0, so the mass difference

$$\Delta M = M(K^- \pi^+ \pi^+_{slow}) - M(K^- \pi^+) \tag{6.2}$$

is better resolved than the individual masses [81]. The combinatorial background – fake D^{*+} candidates made up from unrelated tracks – increases with ΔM, so it

[1] Charge conjugate states are implicitly included in the rest of this chapter.

is suppressed by the smallness of the mass difference. The peak in ΔM therefore provides a clear signal for charm production and is used to estimate the number of $D^{*\pm}$ mesons produced.

Only the central tracker is used for the reconstruction of tracks in this analysis. Tracks are only used if they fall within the θ and $p_\perp$ range where the CJC is efficient: all three tracks must lie in the range

$$25^\circ < \theta < 155^\circ. \tag{6.3}$$

A requirement

$$p_\perp > 200 \text{ MeV} \tag{6.4}$$

is applied to the candidates for the K^- and π^+ from the D^0 decay. This is well into the plateau of the curve of efficiency against $p_\perp$ for the CJC, and is high enough to reject a certain amount of combinatorial background from low-momentum tracks.

In choosing the cut on the $p_\perp$ of the slow pion π^+_{slow}, it is still important to keep to the efficient region. However, this cut determines the threshold in $p_\perp$ below which a D^{*+} can not be detected, and thus has a significant effect on the number of D^{*+} mesons counted and hence on the statistical error in the cross-section measurement. Because of this, a looser cut of

$$p_\perp > 100 \text{ MeV} \tag{6.5}$$

is applied to the π^+_{slow} candidate.

In order to protect against badly reconstructed tracks, it is also required that each track starts in the inner part of the tracker (CJC1) and has a radial length in the $r\phi$ projection of

$$R_{track} > 10 \text{ cm}. \tag{6.6}$$

This has the effect of rejecting 'broken' tracks, where a single charged particle has been reconstructed as two separate tracks – typically one in CJC1 and another in CJC2.

Those accepted tracks passing the higher $p_\perp$ cut 6.4 are combined to form all possible oppositely charged pairs. No particle identification is used; each track is taken to be a K and a π in turn. If a pair has a reconstructed invariant mass within 80 MeV of the D^0 mass, it is counted as a D^0 candidate. Each D^0 candidate is combined in turn with all remaining accepted tracks passing the lower $p_\perp$ cut 6.5 and having the appropriate charge to form D^{*+} candidates. After cuts on the direction

and transverse momentum of the reconstructed D^{*+}

$$|\eta| < 1.25 \tag{6.7}$$

$$p_\perp > 1 \text{ GeV} \tag{6.8}$$

the mass difference ΔM is plotted as a histogram (figure 6.2). The equivalent plot for 'wrong-sign' combinations (where the K and π have the same charge and the π_{slow} the opposite charge) is also shown. The right-sign data shows a peak around the expected position at $\Delta M = 145$ MeV; as expected, there is no evidence for a peak in this region in the wrong-sign histogram. The $K\pi$ mass distribution for $D^{*\pm}$ candidates falling within 2 MeV of the nominal value of ΔM is shown in figure 6.3. A clear peak is seen in the region of the D^0 mass of 1.865 GeV. An example of an event containing a D^{*+} candidate within the region of the ΔM peak is shown in figure 6.1.

The distribution of η_{max} for $D^{*\pm}$ candidates is shown in figure 6.4. A cut

$$|\Delta M - \Delta M_0| < 2 \text{ MeV}, \tag{6.9}$$

where $\Delta M_0 = M_{D^{*+}} - M_{D^0} = 145.4$ MeV, is applied in order to select events in the region of the peak, as well as all the selection cuts described in chapter 5 (apart from that on η_{max}). The histogram clearly shows the low-η plateau characteristic of diffractive events (cf. figure 3.5). The contribution expected from non-diffractive DIS has been calculated using the heavy-flavour Monte Carlo generator AROMA [82] and is also shown. Even without the cut on η_{max} used in the cross-section measurement, most of the AROMA events are rejected by the cuts on activity in the forward detectors.

6.2 Calculation of the Cross Section

The cross section is defined as

$$\sigma = \frac{\mathrm{d}N_D}{\mathcal{L}\mathrm{d}t} \tag{6.10}$$

where $\frac{\mathrm{d}N_D}{\mathrm{d}t}$ is the mean rate of production of $D^{*\pm}$ mesons in a given kinematic region and $\mathcal{L}$ is the instantaneous luminosity. Of the $D^{*\pm}$ mesons produced, only a small fraction are reconstructed. This is due to the small branching fraction for the decay chain used, and to the imperfect acceptance of the detector and of the criteria used to select diffractive deep-inelastic events and $D^{*\pm}$ candidates. The cross section is

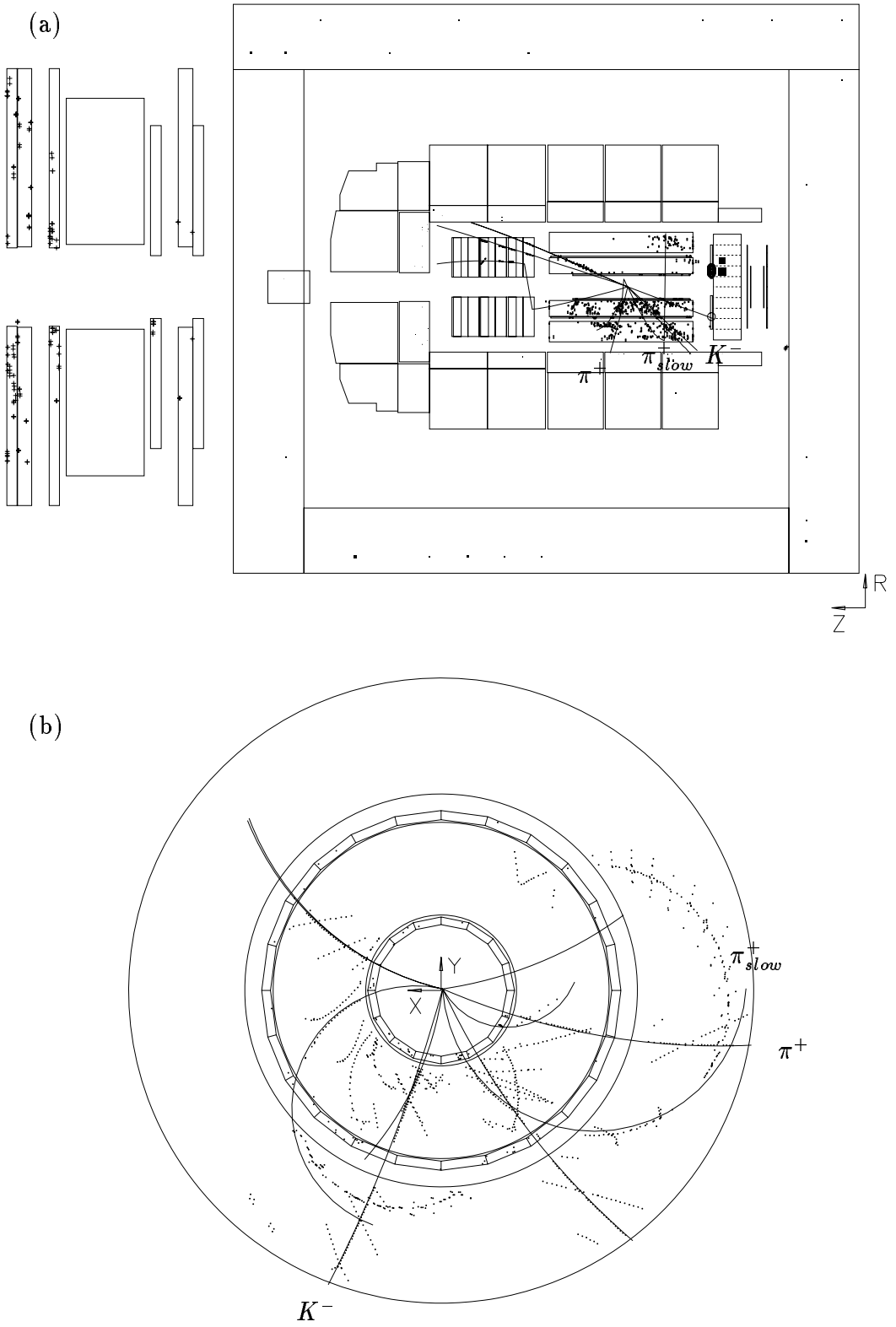

Figure 6.1: A diffractive DIS event containing a D^{*+} candidate: (a) rz projection; (b) xy projection of the central tracker.

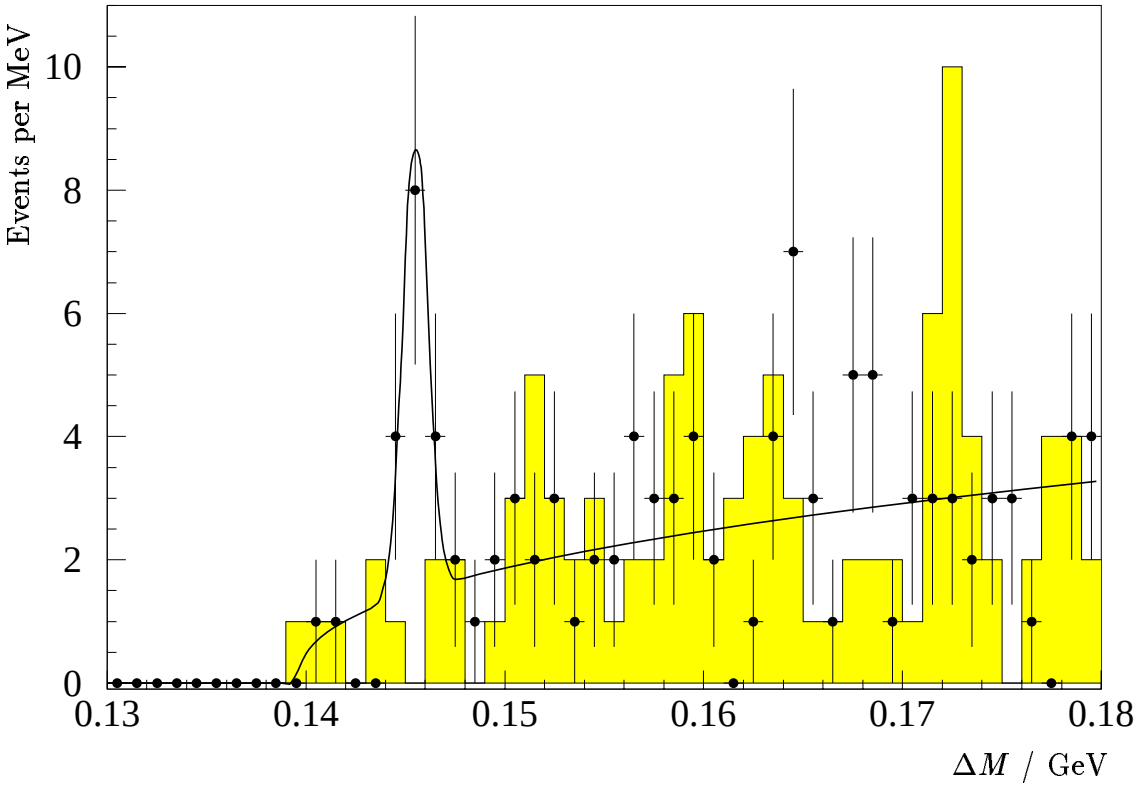

Figure 6.2: Distribution of the mass difference $\Delta M = M(K\pi\pi) - M(K\pi)$. The points with error bars show the right-sign combinations $(K^-\pi^+)\pi^+_{slow}$, and the shaded histogram shows the wrong-sign combinations $(K^+\pi^+)\pi^-_{slow}$. The curve is a fit of the form $a(\Delta M - M_{\pi^+})^b + Gaussian$ to the right-sign data. A peak is seen in the right-sign data at the expected position, $\Delta M = 145$ MeV.

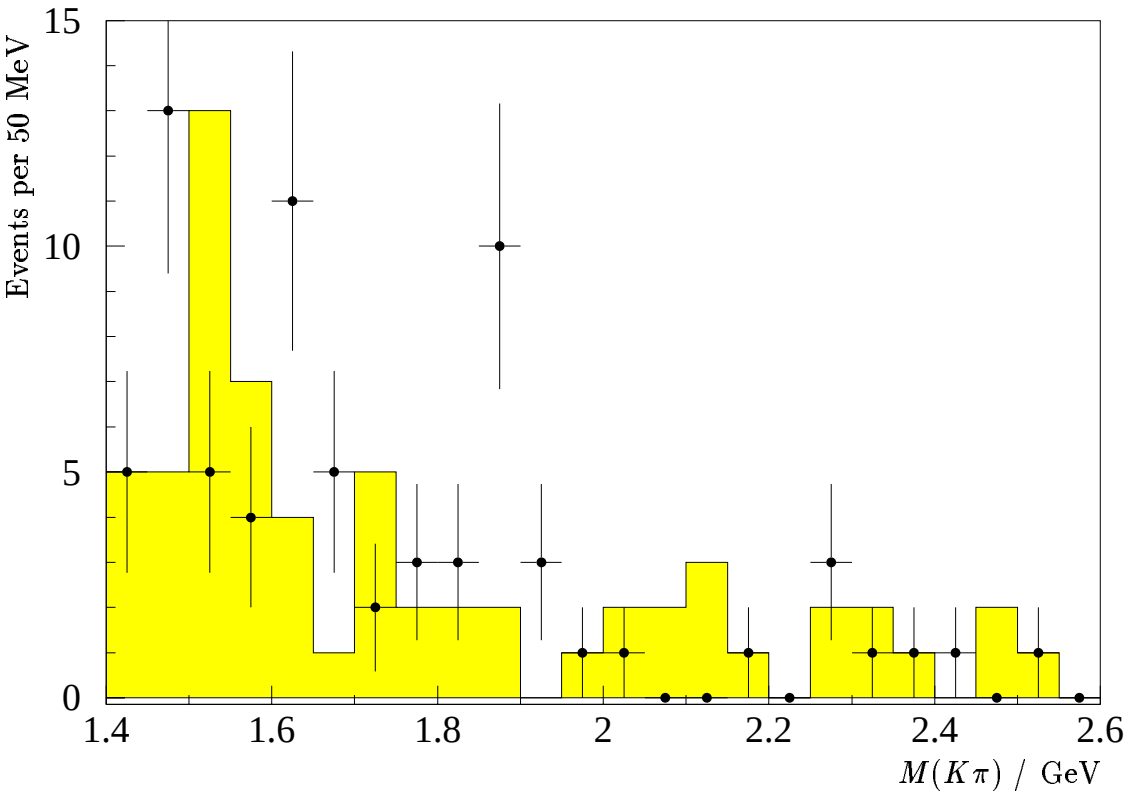

Figure 6.3: Distribution of the invariant mass of D^0 candidates from the signal region of the ΔM distribution, $|\Delta M - \Delta M_0| < 2$ MeV. The points with error bars show the right-sign combinations, and the shaded histogram shows the wrong-sign combinations. A peak is seen around the D^0 mass, 1.865 GeV.

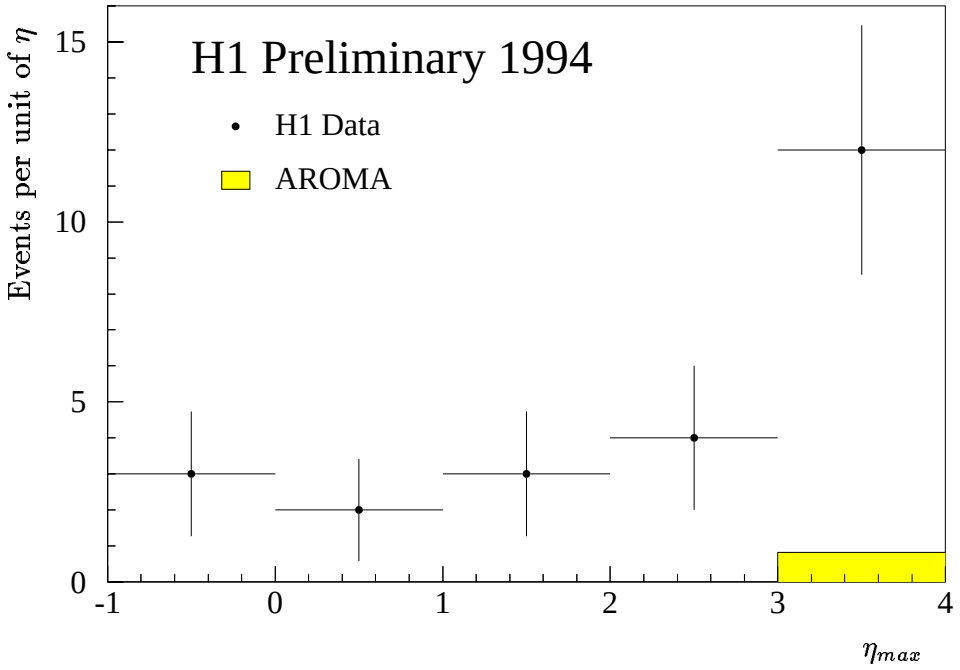

Figure 6.4: Distribution of η_{max} for diffractive $D^{*\pm}$ candidates in the region $|\Delta M - \Delta M_0| < 2.0$ MeV, with the expectation from the non-diffractive Monte Carlo generator AROMA.

estimated using the formula

$$\sigma = \frac{N_{obs}(1-\xi)}{ATP\epsilon\nu B\mathcal{L}_{int}} \tag{6.11}$$

where

- N_{obs} = number of entries in ΔM peak;
- ξ = fraction of events in peak that are due to background;
- A = smeared acceptance calculated using Monte Carlo simulation;
- T = ratio of data and Monte Carlo efficiencies for detection of all three tracks;
- P = correction for the effect of proton dissociation;
- ϵ = trigger efficiency;
- ν = correction for effect of noise in forward detectors on event selection;
- B = branching fraction for decay channel used;
- $\mathcal{L}_{int}$ = integrated luminosity $\int \mathcal{L}\, dt$.

These factors are discussed individually in the following sections.

6.2.1 N_{obs} – Observed Number of $D^{*\pm}$ Mesons

The number of $D^{*\pm}$ mesons observed, i.e. the number of entries in the ΔM peak, is estimated by fitting the histogram (figure 6.2) with the sum of a Gaussian – modelling the signal – and a background function

$$a(\Delta M - m_{\pi^+})^b. \tag{6.12}$$

The fitting package MINUIT [83] is used to perform the fit using a maximum-likelihood method. The area, position and width of the Gaussian and the parameters a and b of the background curve are allowed to vary. The area of the Gaussian peak is found to be $N_{obs} = 11.6^{+4.6}_{-3.9}$.

Statistical Error

The statistical error, taken to be the total error calculated by MINUIT, is somewhat larger then $\sqrt{N_{obs}}$. This is because all parameters describing the shape, as well as the normalization, of the fitted curve are determined by the fit to the ΔM histogram. Thus the error contains a contribution from the uncertainty in the background shape and in the position and width of the peak, as well as from the number of events in the peak and in the underlying background.

6.2.2 A – Smeared Monte Carlo Acceptance

Monte Carlo simulation

The H1 detector-simulation program H1SIM (see section 4.10) is used to estimate the smeared acceptance – the fraction of $D^{*\pm}$ mesons produced in the given kinematic range that are reconstructed and pass all cuts on the reconstructed kinematic variables. This method takes into account most geometrical and detector effects:

- the fraction of $D^{*\pm}$ mesons with all decay products within the required ranges of θ and $p_\perp$;

- the fraction of events in which the scattered positron satisfies the requirements on its direction and energy;
- the fraction of events that satisfy the requirements on activity in the forward direction;
- the energy, momentum and position resolution of the various components of the detector (*smearing*).

Some effects, however, are not simulated: the effect of proton dissociation on the acceptance is estimated separately (see section 6.2.4). The effect of detector and readout noise is also estimated separately (see section 6.2.6), and a correction is made for the tracking efficiency, which is not accurately simulated at low $p_\perp$ (see section 6.2.3).

The Monte Carlo generator RAPGAP [79] (see also section 6.4) was used to generate 10000 diffractive events in which charm quarks were produced. All D^{*+} mesons produced were constrained to decay via the channel $D^0\pi^+ \rightarrow (K^-\pi^+)\pi^+$. The 5022 events containing $D^{*\pm}$ mesons were then passed through the H1 detector simulation package H1SIM and the reconstruction package H1REC. The same program used for finding $D^{*\pm}$ mesons in the data was run on these simulated events and the number of entries in the ΔM peak was counted.

Reweighting the $p_\perp$ Spectrum

In order to reproduce better the $p_\perp$ spectrum of $D^{*\pm}$ candidates observed in the data, the Monte Carlo events are weighted with a function $(p_\perp)^\alpha$, where $p_\perp$ is the generated transverse momentum of the $D^{*\pm}$ and α is a constant. The $p_\perp$ spectrum of the $D^{*\pm}$ mesons produced has a significant effect on the acceptance because of its correlation with the $p_\perp$ of the slow pion. The spectrum may depend on the mechanism for charm production in diffractive DIS, so if the cross section is to be measured without making unnecessary assumptions about the mechanism, the spectrum must be determined from the data, although the low statistics available limit the precision with which this can be achieved. The Monte Carlo generator predicts a 'harder' spectrum – one peaked at larger $p_\perp$ – than is observed, so a negative value of the constant α is used to make the spectrum softer.

To simulate the effect of background, a contribution at low $p_\perp$ is added to the reconstructed spectrum after reweighting. The shape of this background distribution is taken from the RAPGAP Monte Carlo generator, and the normalization

is calculated using the signal-to-background ratio from the fit to the ΔM histogram from the data. The reconstructed $p_\perp$ spectrum including background is then compared to the spectrum from the data. The central value chosen for the reweighting parameter, $\alpha = -1.2$, is that giving the maximum likelihood for the comparison. The generated $p_\perp$ spectrum after reweighting is shown in figure 6.5. Figure 6.6 shows the Monte Carlo spectrum after reconstruction and addition of background, as well as the spectrum for the data.

The Acceptance

The smeared acceptance A is defined as N_{rec}/N_{gen}, where N_{gen} is the number of $D^{*\pm}$ mesons in the Monte Carlo sample satisfying all relevant cuts at the generator level

$$10 \text{ GeV}^2 < Q^2 < 100 \text{ GeV}^2 \tag{6.13}$$

$$0.06 < y < 0.6 \tag{6.14}$$

$$x_{I\!P} < 0.05 \tag{6.15}$$

$$|t| < 1 \text{ GeV}^2 \tag{6.16}$$

$$|\eta(D^*)| < 1.25 \tag{6.17}$$

$$p_\perp(D^*) > 1 \text{ GeV} \tag{6.18}$$

and N_{rec} is the number of reconstructed $D^{*\pm}$ mesons (entries in the ΔM peak) satisfying all the cuts applied to the reconstructed event and $D^{*\pm}$ quantities in the data, regardless of the generated values. Thus both losses (where a $D^{*\pm}$ is not reconstructed or the event is rejected) and migrations (where a $D^{*\pm}$ is generated outside the required kinematic region but because of smearing is reconstructed inside this region) are taken into account.

Figures 6.7 and 6.8 show the variation of the acceptance with the transverse momentum and direction of the $D^{*\pm}$. The acceptance is very nearly zero below $p_\perp = 1$ GeV and is low for $|\eta| > 1.25$, so no measurement is made in these regions; the cross section is quoted for the range $p_\perp > 1$ GeV and $|\eta| < 1.25$. In principle, an extrapolation could be made to obtain the total cross section for production of $D^{*\pm}$ mesons and hence of charm. However, the result would be sensitive to the distributions assumed for $p_\perp$ and η, and would therefore be dependent on the model used to describe diffractive deep-inelastic charm production.

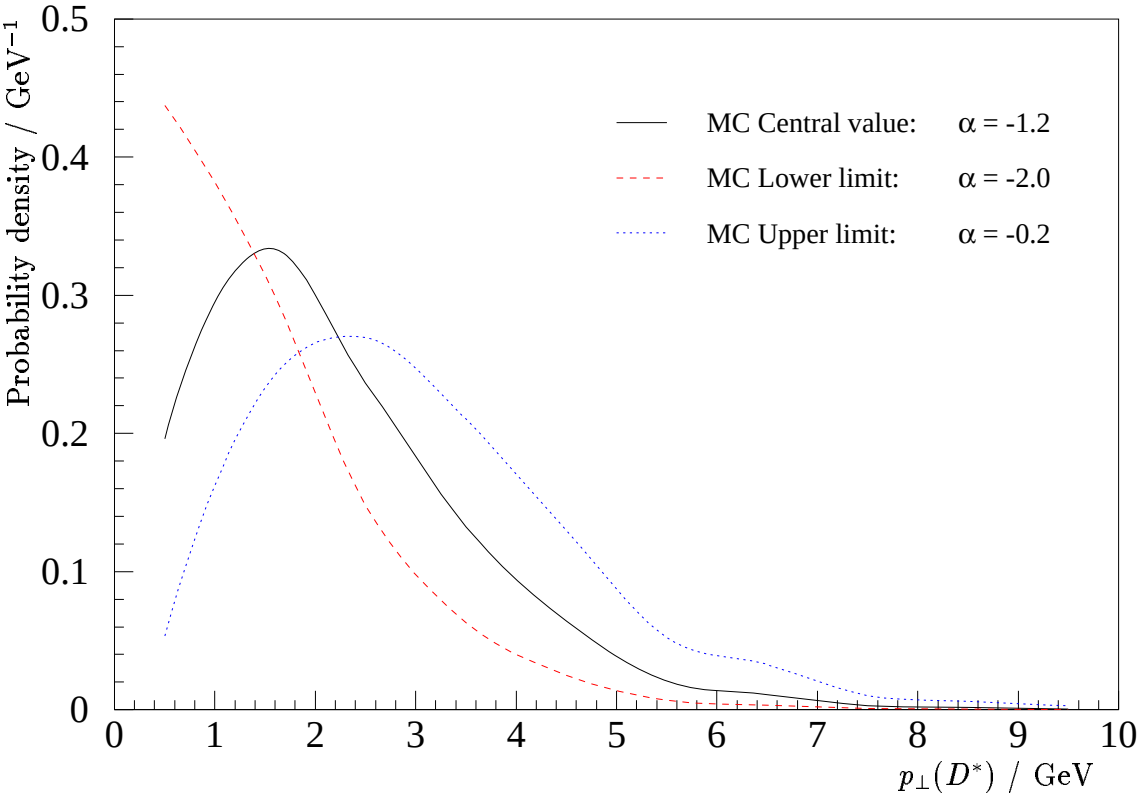

Figure 6.5: The generated $p_\perp$ spectrum after reweighting to match the data. The central value and one-standard-deviation limits of α are taken from a maximum-likelihood fit of the reconstructed spectrum to that from the data.

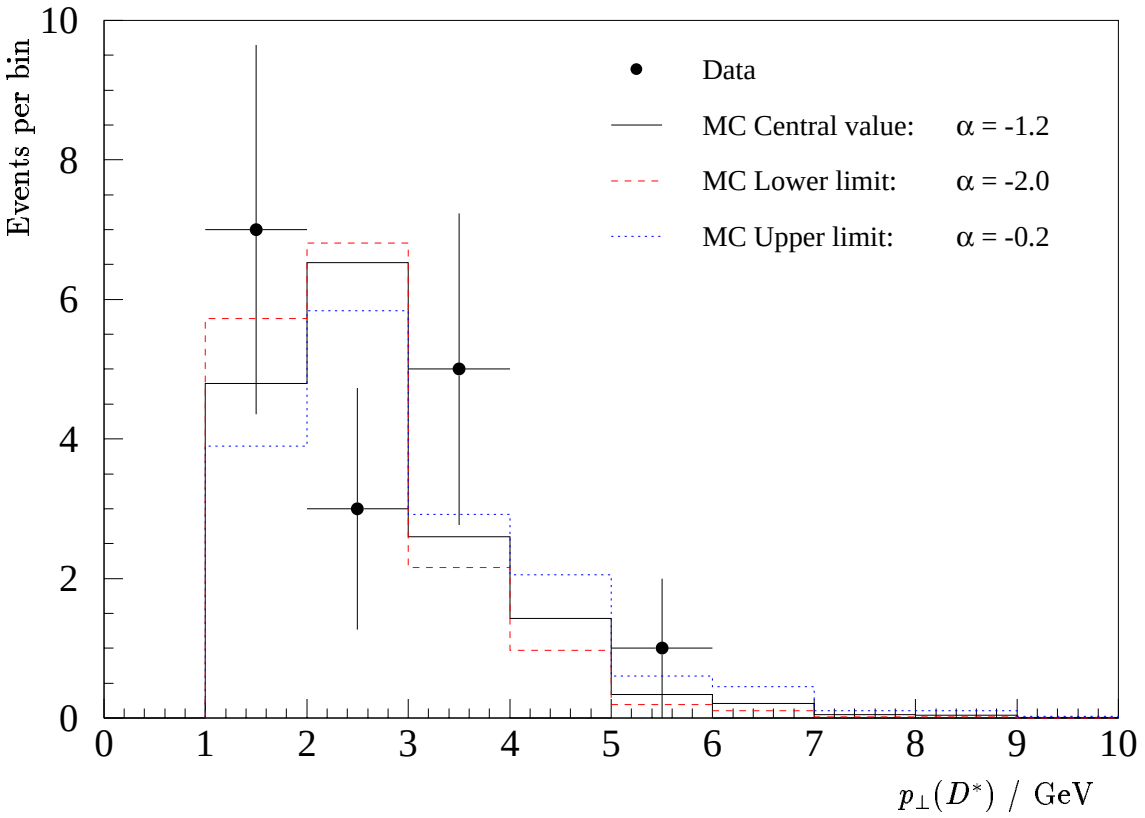

Figure 6.6: The $p_\perp$ spectrum from the data compared with the reweighted Monte Carlo. The Monte Carlo histograms show the $p_\perp$ after reconstruction and addition of background. The range of α illustrated corresponds to the central value and one-standard-deviation limits from a binned maximum-likelihood fit.

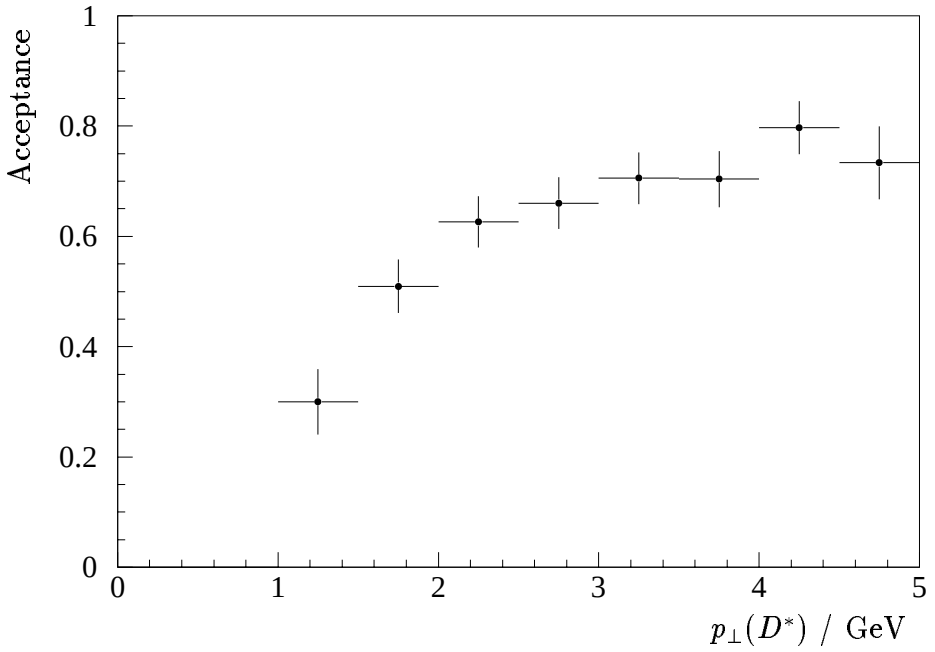

Figure 6.7: The acceptance for $D^{*\pm}$ mesons in the range 10 GeV^2 $< Q^2 <$ 100 GeV^2, $0.06 < y < 0.6$, $x_{I\!P} < 0.05$, $|t| < 1$ GeV^2 and $|\eta(D^*)| < 1.25$, plotted against $p_\perp(D^*)$.

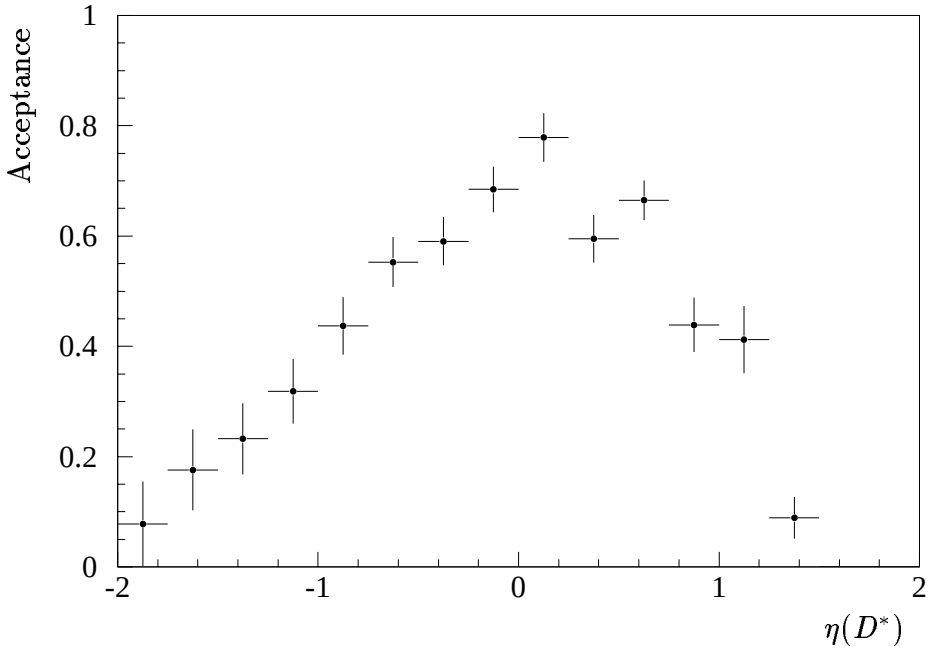

Figure 6.8: The acceptance for $D^{*\pm}$ mesons in the range 10 GeV^2 $< Q^2 <$ 100 GeV^2, $0.06 < y < 0.6$, $x_{I\!P} < 0.05$, $|t| < 1$ GeV^2 and $p_\perp(D^*) > 1$ GeV, plotted against $\eta(D^*)$.

Errors

The largest source of uncertainty in the acceptance comes from the reweighting of the $p_\perp$ spectrum. Because of the small number of $D^{*\pm}$ candidates in the data, the shape of the spectrum is not very well constrained (see figure 6.5). The upper and lower limits on the reweighting parameter α are taken to be the values where $-\ln(\mathcal{L})$ is 0.5 above its minimum value, where $\mathcal{L}$ is the likelihood for the comparison between data and Monte Carlo. The difference of 0.5 corresponds to errors of one standard deviation in the Gaussian case. The allowed range is then $-2.0 < \alpha < -0.2$. This gives an error of $^{+17}_{-19}\%$ on the acceptance, and hence $^{+23}_{-14}\%$ on the cross section.

Another source of uncertainty is the β distribution of the Monte Carlo generated events, which depends on the structure function assumed for the pomeron. The Monte Carlo events used in calculating the acceptance were generated using a pomeron structure that is dominated by gluons and is flat in β at the starting scale for QCD evolution, whereas experimental results – such as the diffractive structure function $F_2^{D(3)}$ [56] – support a structure with a greater contribution at larger values of β. The acceptance is recalculated after reweighting the β distribution to match the distribution in each of two different samples of Monte Carlo events, generated using different hard gluon-dominated pomeron structure functions. The acceptance changes by $^{+1}_{-3}\%$.

The other important source of uncertainty is the statistical error due to the finite number of Monte Carlo events used to estimate the acceptance. The error from this source is $\pm 3\%$.

The acceptance A, with combined errors, is therefore $0.416^{+0.071}_{-0.080}$.

6.2.3 T – Tracking Efficiency

The efficiency for detecting high-$p_\perp$ tracks in the CJC has been estimated using cosmic rays [84]. The efficiency at low $p_\perp$ has been studied [85] using K^0_s decays into $\pi^+\pi^-$; the fact that these decays occur isotropically in the K^0_s rest frame, together with the observed $p_\perp$ spectrum of reconstructed K^0_s mesons producing at least one comparatively fast pion ($p_\perp > 400$ MeV), is used to find the shape of the graph of efficiency against $p_\perp$. The efficiency is found to rise from zero to its maximum value between 90 and 140 MeV and remain constant above this.

The Monte Carlo detector simulation does not accurately reproduce this behaviour, remaining high down to lower values of $p_\perp$ [86]. For tracks at $\theta = 90°$, the simulated efficiency is still above 90% for $p_\perp$ as low as 80 MeV.

The mean efficiency for detecting the slow pion π^+_{slow} is estimated using the approximation

$$\epsilon_{avg} = \epsilon_{low} F + \epsilon_{high}(1 - F) \tag{6.19}$$

where

- ϵ_{low} is the efficiency for detecting tracks in the range 100 MeV $< p_\perp <$ 140 MeV;
- ϵ_{high} is the efficiency for detecting tracks with $p_\perp > 140$ MeV
- F is the fraction

$$\frac{\text{No. of } \pi_{slow} \text{ with } 100 \text{ MeV} < p_\perp < 140 \text{ MeV}}{\text{No. of } \pi_{slow} \text{ with } p_\perp > 100 \text{ MeV}}.$$

The value of F is estimated using Monte Carlo events to be 0.26 ± 0.10. The efficiencies ϵ_{low} and ϵ_{high} are taken to be 0.85 ± 0.10 and 0.98 ± 0.02 respectively, based on the results of [84, 85]. The mean efficiency for detection of the slow pion is thus 0.95 ± 0.03, and for each of the other two tracks it is 0.98 ± 0.02.

Each reconstructed track must also be linked to the primary vertex of the event. The efficiency for this linking is known to be at least 0.97 [84], and is therefore taken to be $1.00^{+0.00}_{-0.03}$. Taking both tracking and vertex-fitting efficiencies into account, the correction factor is $T = 0.91^{+0.06}_{-0.10}$.

The fraction F depends on the reweighting parameter α used to calculate A, so there is a correlation between A and T, which must be taken into account. The effect on the product AT of varying α and F simultaneously, with F increasing as α decreases, is used to estimate the uncertainty from this source. When this is done, and combined with the other (uncorrelated) sources of error described above, the result is $AT = 0.378^{+0.075}_{-0.087}$.

6.2.4 P – Correction for Proton Dissociation

The Monte Carlo events used to calculate the acceptance A are purely proton-elastic. The acceptance calculated in this way does not take into account

the loss of those low-mass ($M_Y < 1.6$ GeV) dissociative events that cause activity in the forward detectors (particularly the proton-remnant tagger) and are thus rejected, or the opposing effect of higher-mass dissociative events passing the cuts on forward activity. The correction factor for these effects has been estimated separately [87] by using the Monte Carlo generator DIFFVM [88] to generate proton-dissociative events with a range of values of M_Y, and passing these events through the detector simulation program. The result is $P = 0.987 \pm 0.027 \pm 0.025$, where the first error is that due to the dependence of the result on the model used to describe proton dissociation, and the second is that due to the uncertainty in the efficiency of the forward detectors.

6.2.5 ϵ – Trigger Efficiency

The efficiency of the low-Q^2 DIS subtrigger has been found using data to be more than 0.99 [21] for events lying in the kinematic range studied here and having a scattered positron with energy $E'_e > 10$ GeV. When the prescaling mentioned in section 5.2.3 is taken into account, the mean efficiency falls slightly to $\epsilon = 0.98 \pm 0.01$.

6.2.6 ν – Correction for Noise in Forward Detectors

The amount of activity in the forward detectors is used to distinguish diffractive events from non-diffractive ones. However, even if the event has a rapidity gap, there is some chance that noise in the forward detectors will lead to energy being 'detected' where none really exists and the event will be rejected by the forward cuts. Noise is not added to events in the detector simulation, so this effect leads to a reduction in the acceptance relative to that calculated using the Monte Carlo. The size of the resulting change has been estimated [89] using events selected by the random trigger. Most of these have no real activity in the detector, so the fraction of them that fail the forward cuts is a measure of the effect of noise. The fraction of events lost in this way is found to be $(7 \pm 3)\%$, where the error is estimated from the variation of the number over the period when the data was taken. The correction factor is thus $\nu = 0.93 \pm 0.03$.

6.2.7 ξ – Background Correction

The significant sources of background in this analysis are reflections (i.e. contributions from D^0 decay modes other than $K^-\pi^+$), non-diffractive DIS (meaning events with $x_{I\!P} > 0.05$), and high-t events (those with $|t| > 1$ GeV^2). There is also a small amount of contamination from photoproduction events in which a scattered positron is faked.

The contribution from reflections is estimated using RAPGAP. Generated events containing $D^{*\pm}$ mesons decaying via channels other than the one used for the cross-section measurement are passed through the detector simulation and the analysis program. The size of the resulting peak in ΔM is used to estimate the fraction of the data peak that is due to such background (see figures 6.9 and 6.10). This fraction is estimated to be $(20 \pm 15)\%$, with the error being dominated by the limited Monte Carlo statistics available to estimate this correction.

Non-diffractive DIS background is simulated using RAPGAP to generate events in the range $0.05 < x_{I\!P} < 0.2$, and the heavy-flavour generator AROMA [82] to generate events in the range[2] $x_{I\!P} > 0.2$. The relative normalization of the AROMA sample is calculated from the measured cross section for production of $D^{*\pm}$ mesons in DIS [25]. The error is conservatively estimated to be equal to 100% of the size of the correction. This source of background is estimated to contribute $(5 \pm 5)\%$ to the signal.

The background from high-t events is estimated by using RAPGAP to generate events with a t distribution extending out to 20 GeV^2, where the acceptance is low and the number of events is small. Of those events passing the selection cuts applied to the reconstructed events, 7% have a generated value $|t| > 1$ GeV^2. The error is taken to be 100% of the size of the correction, so this source of background is estimated to contribute $(7 \pm 7)\%$ to the observed signal.

The background from photoproduction is investigated by using RAPGAP to generate diffractive photoproduction events and PHOJET [90] to generate inclusive photoproduction events. These events are passed through the detector simulation and the same cuts used on the data to select diffractive deep-inelastic events are applied. An upper limit of 3% can be placed on contamination from this source.

These four contributions are combined to give a total background fraction

[2] $x_{I\!P}$ is defined for both diffractive and non-diffractive Monte Carlo generated events by taking the diffracted hadronic state Y to be the stable final-state particle with the largest momentum component p_z in the direction of the proton beam.

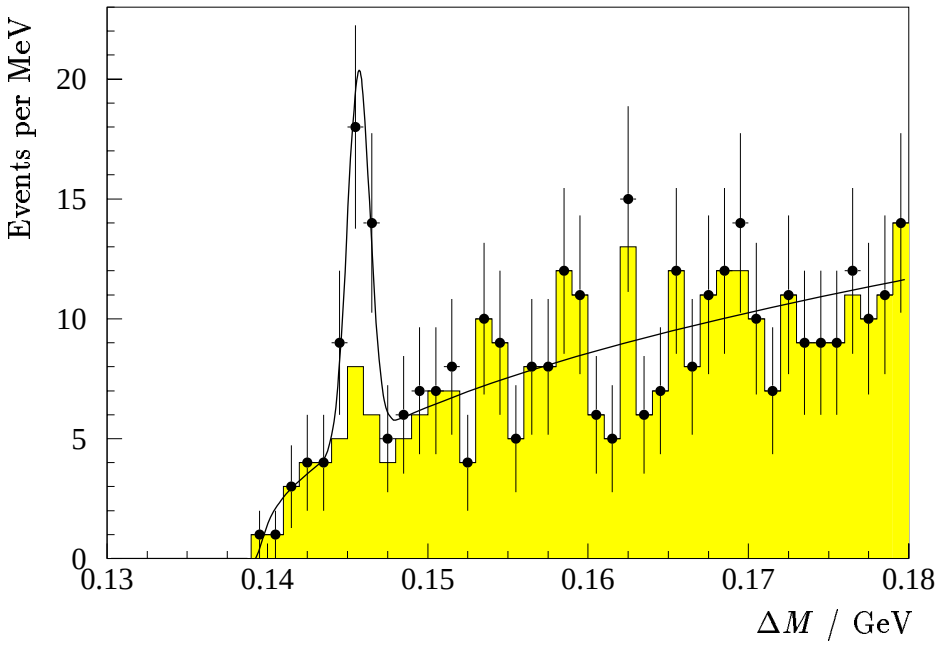

Figure 6.9: Distribution of the mass difference ΔM for Monte Carlo events. The points show the signal when all Monte Carlo events are used. The shaded area shows the signal for all background events, i.e. those without a $D^{*\pm}$ decaying via the required chain.

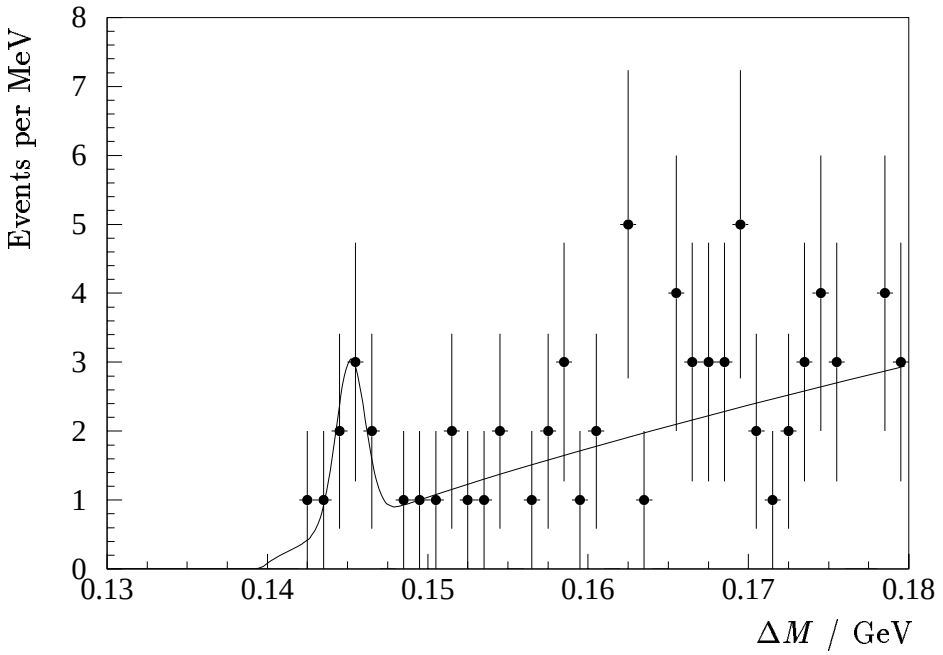

Figure 6.10: Distribution of the mass difference ΔM for Monte Carlo events with a generated $D^{*\pm}$ decaying via a chain other than that assumed in the reconstruction.

of $\xi = 0.29 \pm 0.15$.

6.2.8 B – Branching Fraction

The branching fractions for the processes $D^{*+} \to D^0\pi^+$ and $D^0 \to K^-\pi^+$, and the corresponding errors, are taken from [91] and combined to find the overall fraction of D^{*+} mesons that decay via this chain, $B = 0.0262 \pm 0.0010$.

6.2.9 $\mathcal{L}_{int}$ – Integrated Luminosity

The time-integrated luminosity corresponding to the data used is calculated using information from the luminosity system. A correction is made for the time during which any of the detector components necessary for this analysis were not operational. Further corrections are made for the fraction of luminosity due to satellite bunches and to interactions which occur outside the region -25 cm $< z <$ 35 cm. The result is $\mathcal{L}_{int} = 2.23$ pb^{-1}.

The systematic error on the luminosity estimate for 1994 nominal-vertex data is estimated in [21] to be $\pm 1.5\%$.

Acceptance and efficiency:	$p_\perp$ spectrum	$^{+25}_{-16}\%$
	β spectrum	$^{+3}_{-1}\%$
	Monte Carlo statistics	$\pm 3\%$
	Proton dissociation	$\pm 4\%$
	Trigger efficiency	$\pm 1\%$
	Noise correction	$\pm 3\%$
	Branching fraction	$\pm 4\%$
	Tracking efficiency	$^{+7}_{-6}\%$
	Vertex fitting	$^{+10}_{-0}\%$
Background subtraction:	Reflections	$\pm 19\%$
	Non-diffractive DIS	$\pm 5\%$
	High-t	$^{+7}_{-8}\%$
	Photoproduction	$^{+0}_{-3}\%$
Luminosity		$\pm 1.5\%$
Total systematic error		$^{+35}_{-28}\%$
Statistical error		$^{+40}_{-34}\%$
Total error		$^{+53}_{-44}\%$

Table 6.1: Sources of error in the calculated cross section.

6.3 Result

The cross section calculated for the region

- $10\ \text{GeV}^2 < Q^2 < 100\ \text{GeV}^2$,
- $0.06 < y < 0.6$,
- $x_{I\!P} < 0.05$,
- $|t| < 1\ \text{GeV}^2$,
- $M_Y < 1.6$ GeV,
- $|\eta(D^*)| < 1.25$, and
- $p_\perp(D^*) > 1.0$ GeV,

where η and $p_\perp$ are measured in the H1 laboratory frame, is

$$\sigma(e^+p \to e^+D^{*\pm}XY) = (410^{+160+150}_{-140-120})\ \text{pb} \tag{6.20}$$

where the errors quoted are the statistical and systematic uncertainties respectively.

6.4 Monte Carlo Prediction

A prediction for the cross section can be obtained using the Monte Carlo generator RAPGAP [79], in which diffractive events are modelled as the collision of a virtual photon with a partonic pomeron, emitted from the proton according to a flux factor $f_{I\!P/p} \sim x_{I\!P}^{-n}$. The structure function of the pomeron is an input to the generator, so predictions can be made using various hypotheses for the pomeron structure.

Predictions have been made using two different pomeron structure functions. One structure function was obtained from a QCD analysis of the diffractive structure function $F_2^{D(3)}$ [56] and is dominated by a hard gluon structure: at low Q^2 ($\sim 2.5\ \text{GeV}^2$) there is a large peak at $\beta \approx 1$, which evolves to lower β with increasing Q^2 (see section 3.3 and figure 3.7). The other structure function consists entirely of quarks at low Q^2, and is also evolved in Q^2.

Using the hard gluon structure function for the pomeron, 160000 events were produced, corresponding to an integrated luminosity of 9.65 pb^{-1}. After application of the cuts 10 GeV^2 $< Q^2 <$ 100 GeV^2, $0.06 < y < 0.6$, $x_{I\!P} < 0.05$ and $|t| < 1$ GeV^2 on the generated events and the cuts $|\eta| < 1.25$ and $p_\perp > 1$ GeV on the generated $D^{*\pm}$ mesons, the number of $D^{*\pm}$ mesons remaining is 1569. This leads to a prediction for the cross section measured above of

$$\sigma(e^+p \rightarrow e^+D^{*\pm}XY) = 163 \text{ pb}. \tag{6.21}$$

Using the quark-based structure function for the pomeron, a similar calculation [92] gives:

$$\sigma(e^+p \rightarrow e^+D^{*\pm}XY) = 5 \text{ pb}. \tag{6.22}$$

The prediction of the model with the hard gluon structure function for the pomeron is larger by a factor of about 30 than that of the model with the quark-dominated pomeron. The hard-gluon prediction is significantly closer to the measured cross section, although it still falls short by about 1.4 standard deviations, neglecting any uncertainty in the RAPGAP prediction.

Of the 160000 events generated using the hard gluon pomeron, 90000 were produced using the colour-dipole model (CDM) to model the hadronization of the final state, while parton showering (MEPS) was used for the remaining 70000. When a histogram of ΔM is produced from the simulated data, using the same technique as was used for the data, there is a clear difference between the results from the two hadronization models. The number of events in the peak is approximately equal (i.e. the acceptance is unaffected), but there is much less combinatorial background in the MEPS histogram than in the CDM one. The CDM results conform more closely to the data, and are shown in figure 6.11 superimposed on the data histogram.

6.5 Conclusions

The cross section for production of the charmed meson $D^{*\pm}$ in deep-inelastic proton diffraction has been measured for the first time. The result clearly favours a model of diffraction in which the pomeron is a gluon-dominated object over one in which it is quark-dominated. This conclusion is consistent with measurements made in inclusive deep-inelastic diffraction, including $F_2^{D(3)}$ and energy flow in the hadronic final state.

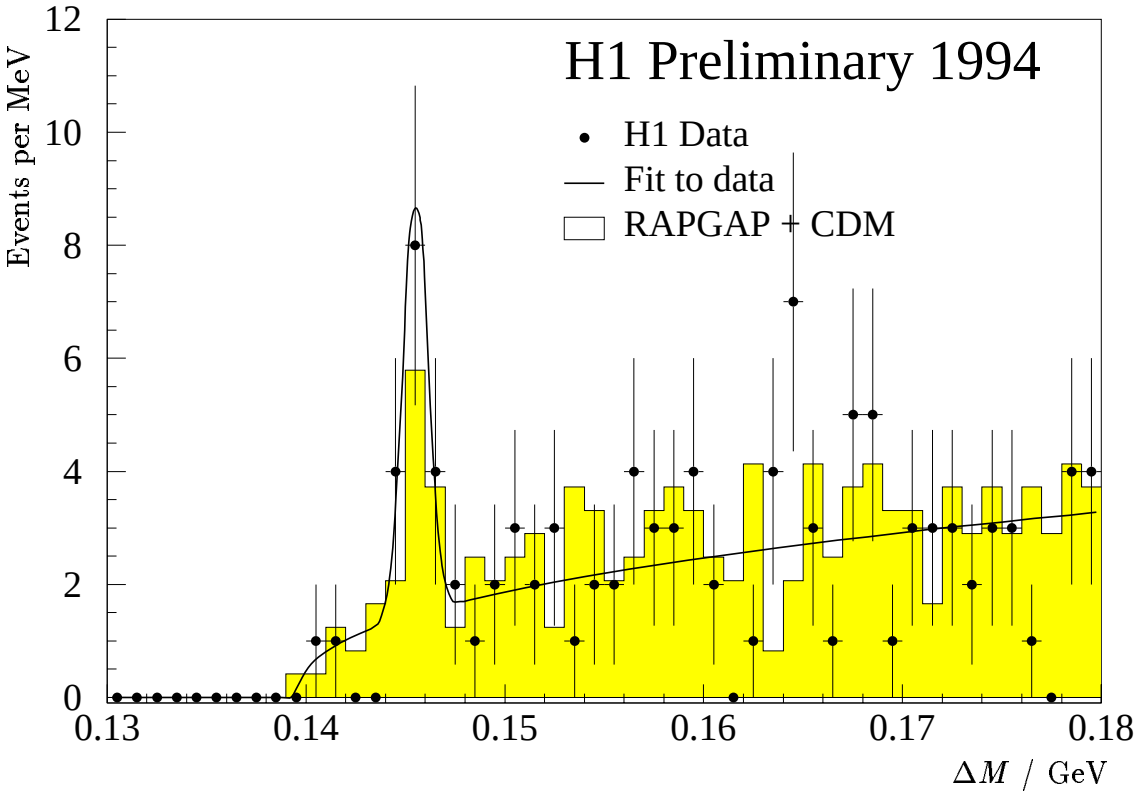

Figure 6.11: Distribution of the mass difference $\Delta M = M(K^-\pi^+\pi^+_{slow}) - M(K^-\pi^+)$, with a fitted curve of the form $a(\Delta M - M_{\pi^+})^b + Gaussian$ and a prediction from RAPGAP with the hard-gluon pomeron structure extracted from $F_2^{D(3)}$.

More detailed investigations of diffractive charm production, and hence of the gluon content of the diffractive exchange, will become possible in the future with increased luminosity and detector upgrades. This is the subject of chapter 7.

Chapter 7

Future Measurements

The luminosity achieved by HERA will increase greatly over the next few years, enabling much more precise measurements of diffractive deep-inelastic charm production. It will become practicable to measure the cross section in several bins of Q^2, $x_{I\!P}$ and β, and thus to find the contribution $F_2^{D(3)c}$ of charm production to the diffractive proton structure function $F_2^{D(3)}$. This is a powerful technique for discriminating between rival models of diffractive processes, which differ significantly not only in the overall contribution of charm to the diffractive cross section, but also in its distribution in Q^2, $x_{I\!P}$ and β. Models in which the pomeron is a gluon-rich object predict a large charm cross section, with a strong contribution at large Q^2 and β if there is a leading-gluon or point-like component to the pomeron [60]. This contrasts with some perturbative QCD-based models, such as that of Genovese, Nikolaev and Zakharov [93], which predict much less charm production, but with a strong rise at low $x_{I\!P}$, breaking Regge factorization. Several predictions for $F_2^{D(3)c}$, as well as other diffractive structure functions, are compared in [94]. The prospects for future measurements of diffractive structure functions at HERA are discussed in [95].

In this chapter, the relevant changes to the future operation of H1 and HERA are summarized. Then a Monte Carlo method is used to investigate the precision that can be achieved in measuring the differential cross section for charm production using the method of chapter 6, and other methods of tagging charm in the upgraded H1 detector are considered.

7.1 The Future Operation of H1 and HERA

7.1.1 H1 Detector Upgrades

A number of changes have been made to the H1 detector since the data used in chapter 6 was taken in 1994, and more are planned. The most important of these for charm physics is the installation of the central silicon tracker (CST) [96], which is now in place, though not yet fully operational. The CST will enable weakly decaying charmed (and bottom) hadrons to be tagged by reconstructing their decay vertices, increasing the overall efficiency for detection of charm quarks by up to an order of magnitude (see section 7.3). It will be capable of reconstructing secondary vertices down to about 50 μm from the primary interaction point.

The BEMC was replaced at the end of 1994 by the SpaCal (spaghetti calorimeter) [97], and the BPC by a backward drift chamber (BDC). This extends the angular coverage for detection of the scattered lepton up to $\theta \approx 177.5°$, so the accessible range in Q^2 and x is extended downwards. Events at even lower Q^2 will be covered by the very-low-Q^2 calorimeter (VLQ), to be installed in 1998–1999.

The forward proton spectrometer (FPS) [88], housed in a series of 'Roman pots' along the proton beam pipe in the forward direction, enables the scattered proton in diffractive events to be detected directly. This is essential for obtaining a sample of truly proton-elastic events uncontaminated by proton dissociation, and with sufficient luminosity it will enable the measurement of the fully differential diffractive structure function $F_2^{D(4)}(x, Q^2, x_{I\!P}, t)$. The contribution of charge-exchange interactions $ep \to enX$ to rapidity-gap events will be measured using the forward neutron counter (FNC).

7.1.2 HERA Luminosity

The integrated luminosity delivered by HERA in 1994 was 5 pb^{-1}. In 1996 the figure was 14 pb^{-1}, and this is expected to continue to rise towards the design figure of 40–50 pb^{-1} per year as the operational efficiency is improved and the beam currents increase towards their design values.

Even greater integrated luminosities are desirable in order to make precise measurements of rare processes, such as charged-current scattering and neutral-current scattering at Q^2 close to the kinematic limit. This can be achieved by

changing the beam optics so as to focus the beams to a smaller area at the interaction point (IP).

To do this, the final focussing quadrupole magnets for the proton beam must be brought closer to the IP. The proximity of these magnets to the IP is limited by the requirement that the beams are well separated where they pass through the quadrupoles. By positioning dipole magnets within the H1 and ZEUS detectors, the beams can be separated earlier and new quadrupoles can be installed only 11 m from the IP [98], compared to 22 m in the current arrangement. In this way, the luminosity can be increased by a factor of 3–4. It is proposed to carry out this upgrade during a shutdown of at least six months in the year 2000.

The disadvantages of the proposed upgrade, apart from the luminosity lost during the long shutdown and subsequent tuning of the accelerator (which will be made up in the ensuing high-luminosity running) are an increased level of synchrotron radiation from the electron beam and a loss of detector acceptance close to the beam direction. The detector can be screened adequately from synchrotron radiation by a suitable arrangement of collimators and absorbers. However, the loss of acceptance in the extreme forward and backward regions will make some measurements impossible, in particular those involving low-Q^2 processes and studies of the proton remnant. It has therefore been proposed to accumulate an integrated luminosity of at least 100 pb^{-1} before the upgrade takes place [99].

7.2 Monte Carlo Simulation

The potential for future high-luminosity measurements of charm production in diffractive deep-inelastic interactions is investigated here using Monte Carlo events. As in the measurement described in chapter 6, charm quarks are tagged using the decay channel

$$D^{*+} \rightarrow D^0 \pi^+_{slow} \rightarrow (K^- \pi^+) \pi^+_{slow}.$$

The Monte Carlo generator RAPGAP 2.1 [79], with a pomeron structure function based on a QCD fit to $F_2^{D(3)}$ (dominated by a hard gluon component), was used to generate 30000 diffractive charm events in the range $Q^2 > 10$ GeV^2 and $0.01 < y < 0.99$, corresponding to an integrated luminosity of 20.35 pb^{-1}. All $D^{*\pm}$ mesons produced were forced to decay by the decay chain of interest, so the number of $D^{*\pm}$ mesons in this channel is that expected in 780 pb^{-1}.

The acceptance of the detector is simulated by applying cuts on the generated direction (θ) and transverse momentum ($p_\perp$) of the decay products and on the energy (E'_e) and angle (θ'_e) of the scattered lepton. This method enables the investigation of variations in acceptance as the tracking region and range of E'_e covered are changed, while avoiding the computation-intensive task of passing the events through a full detector simulation.

The $p_\perp$ threshold is fixed at 120 MeV – where the track efficiency is already quite high – for the slow pion, and at 200 MeV for the other two decay products. The tracker is initially assumed to cover the angular range $25° < \theta < 155°$, corresponding to the coverage of the H1 central tracker. The effect of extending this coverage in the forward region (down to $\theta = 8°$, approximately the limit of the H1 forward tracker) and in the backward region (up to $\theta = 170°$, a region covered only by the BDC and SpaCal) is then investigated.

The acceptance region for scattered leptons is taken to extend up to $\theta = 173°$. No lower limit is placed on θ'_e, since at high Q^2 the lepton will be detected in the liquid argon calorimeter rather than the SpaCal. The E'_e threshold is initially taken to be 10 GeV, giving a high detection efficiency and a low level of photoproduction background. This corresponds to an upper limit on y of 0.6 with the present HERA beam energies. The effect of reducing this threshold to 5 GeV ($y = 0.8$) is investigated.

Figure 7.1 shows the expected number of reconstructed $D^{*\pm}$ mesons – assuming that only the central tracker is used and a cut $E'_e > 10$ GeV is applied – binned in Q^2, β and $x_{I\!P}$. The bins are chosen to be similar in size to those used in the first measurement by H1 of the diffractive structure function $F_2^{D(3)}$ [55], with four bins per decade in $x_{I\!P}$ and four bins in total in each of the variables Q^2 and β. The number of entries per bin is sufficient for a measurement of the diffractive charm structure function $F_2^{D(3)c}$ with a statistical precision similar to that of the inclusive measurement in [55].

Figures 7.2(a) and 7.2(b) show the dependence on $x_{I\!P}$ of the acceptance for $D^{*\pm}$ mesons in the low-Q^2 (10–25 GeV^2) and high-Q^2 (50–100 GeV^2) regions respectively. The effects of extending tracking coverage into the forward region and of lowering the cut on E'_e are shown. The acceptance is calculated for generated $D^{*\pm}$ mesons with $p_\perp > 2$ GeV, but no restriction is placed on θ, y or β; thus the effect of the fixed cut on track $p_\perp$ is minimized, while the effects of changing the tracking coverage and the energy threshold for the scattered lepton can be seen clearly. The use of forward tracking has a significant effect at comparatively large values of $x_{I\!P}$,

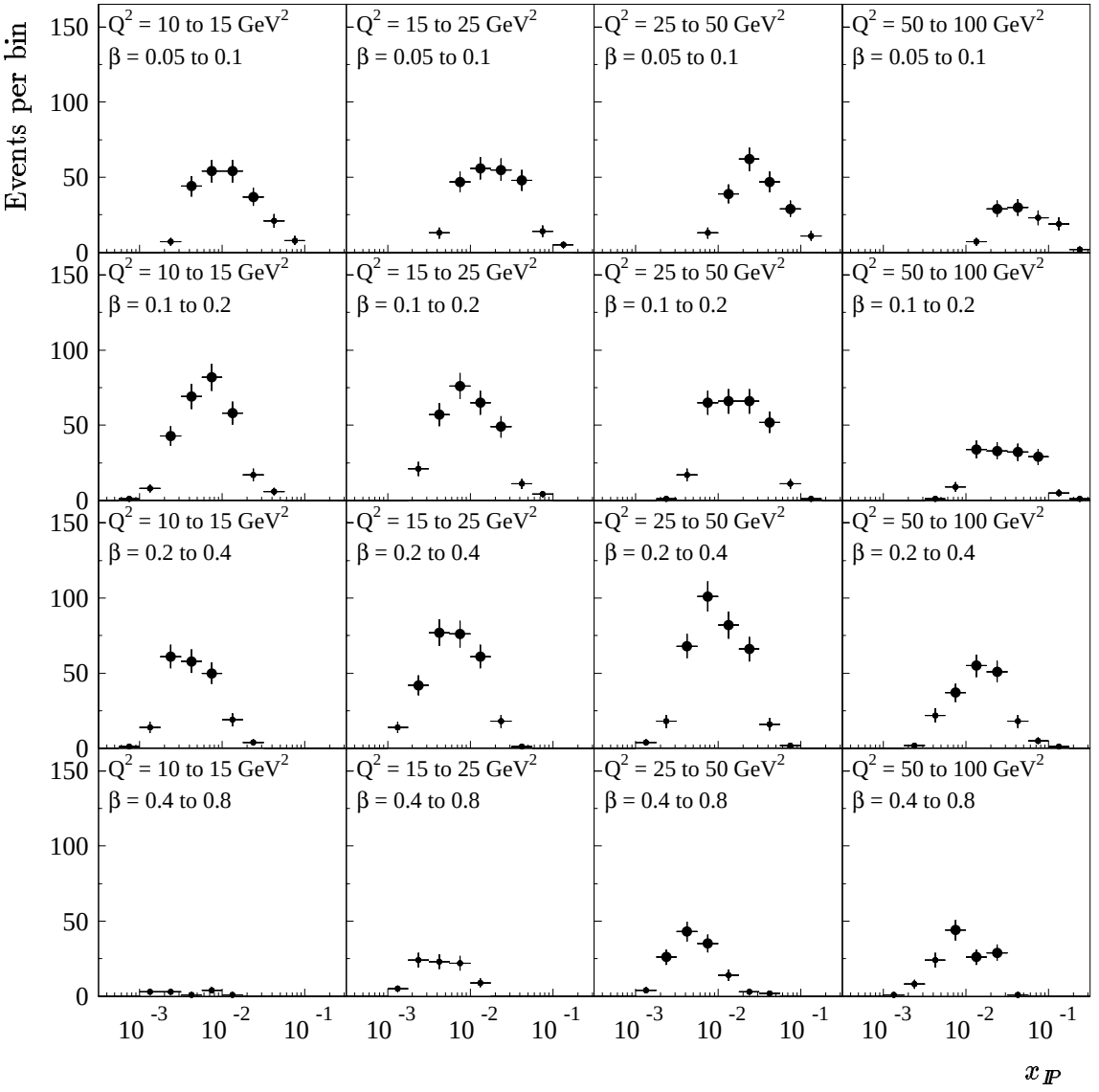

Figure 7.1: Number of reconstructed $D^{*\pm}$ mesons expected in each bin in an integrated luminosity of 780 pb^{-1}. The larger points mark bins containing at least 25 entries, giving a statistical error of about 20% or less.

but makes very little difference in the more interesting small-$x_{I\!P}$ region (below about 0.01). Lowering the E'_e cut has little effect at any value of $x_{I\!P}$.

Figures 7.3(a) and 7.3(b) show the same quantity as the previous two figures, but now with extended tracking in the backward region. This clearly has a much greater effect in the small-$x_{I\!P}$ region, and this effect is enhanced by lowering the E'_e cut. Figures 7.4(a) and 7.4(b) show the expected number of $D^{*\pm}$ mesons reconstructed using the same cuts (apart from that on the $p_\perp$ of the generated $D^{*\pm}$), divided into ten bins per decade of $x_{I\!P}$ in the low-Q^2 region and five bins per decade in the high-Q^2 region. The combination of backward tracking and a lower E'_e cut pushes down the lowest attainable value of $x_{I\!P}$ by a factor of about two.

Useful (though less detailed) studies can be made with much less than 780 pb^{-1} by using larger bins. With 100 pb^{-1}, without any improvement on the current acceptance, 200 reconstructed $D^{*\pm}$ mesons are expected in the low-$x_{I\!P}$ region $x_{I\!P} < 0.01$, and 20 in the high-Q^2, high-β region $Q^2 > 50$ GeV^2 and $\beta > 0.5$.

The 'expected numbers' quoted here are predictions of only one model, but one that predicts a value slightly smaller than the measured $D^{*\pm}$ cross section and describes other aspects of deep-inelastic diffraction well. If the observed numbers are much smaller than these predictions, this too is of course a significant result in its own right.

7.3 Using the Central Silicon Tracker

7.3.1 Background Reduction

When the central silicon tracker (CST), which has already partly been installed, is fully operational, it will be possible to reconstruct the secondary vertex produced by the decay of the D^0. The D^0 cannot decay to a lighter charmed particle, so it decays via the weak interaction and has a decay length $c\tau = 124$ μm which is long enough to be tagged. A Monte Carlo study [100] using the decay chain $D^{*+} \to D^0\pi^+_{slow} \to (K^-\pi^+)\pi^+_{slow}$ has shown that, by requiring a χ^2 probability of less than 0.01 for a fit of the D^0 decay product candidates to the primary vertex, the light-quark background can be removed almost completely while keeping about 40% of the signal.

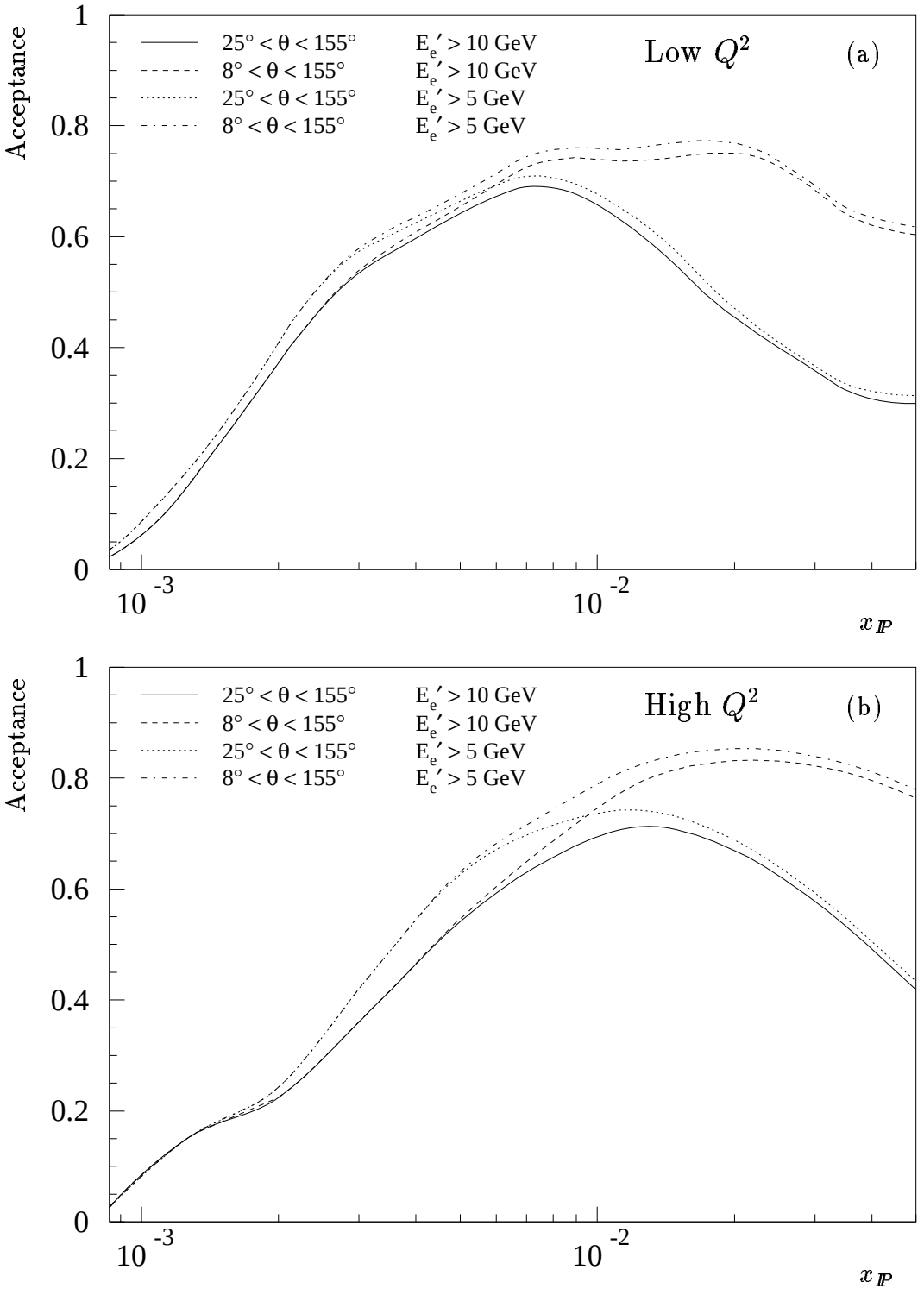

Figure 7.2: The acceptance for $D^{*\pm}$ mesons in the regions (a) 10 GeV^2 $< Q^2 <$ 25 GeV^2 and (b) 50 GeV^2 $< Q^2 <$ 100 GeV^2, plotted as a function of $x_{I\!P}$. The continuous line shows the results with central tracking only and a requirement $E'_e >$ 10 GeV. The other lines show the effect of extending tracking coverage in the forward direction and including E'_e down to 5 GeV.

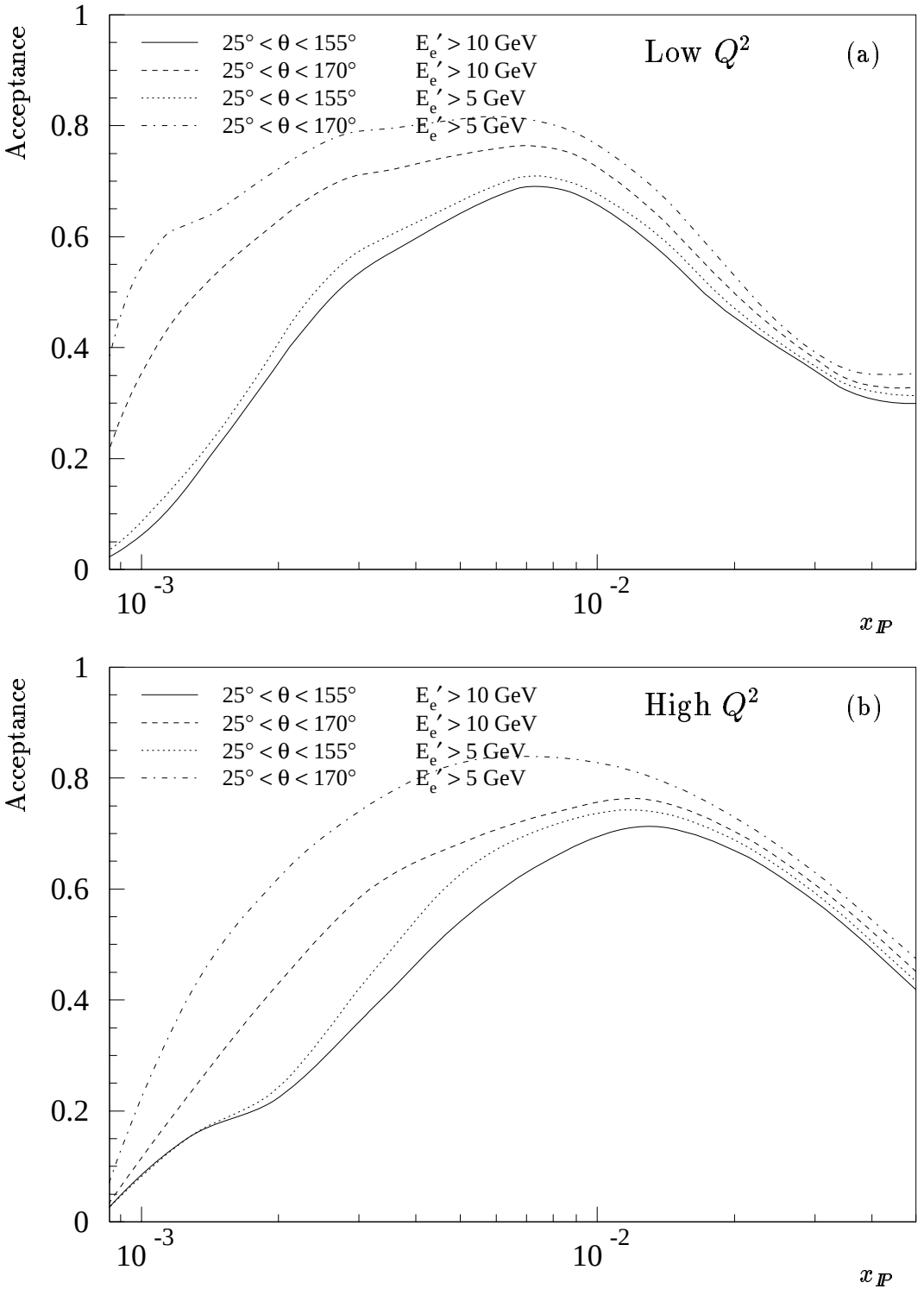

Figure 7.3: The acceptance for $D^{*\pm}$ mesons in the regions (a) 10 GeV^2 $< Q^2 <$ 25 GeV^2 and (b) 50 GeV^2 $< Q^2 <$ 100 GeV^2, plotted as a function of $x_{I\!P}$. The continuous line shows the results with central tracking only and a requirement $E'_e >$ 10 GeV. The other lines show the effect of extending tracking coverage in the backward direction and including E'_e down to 5 GeV.

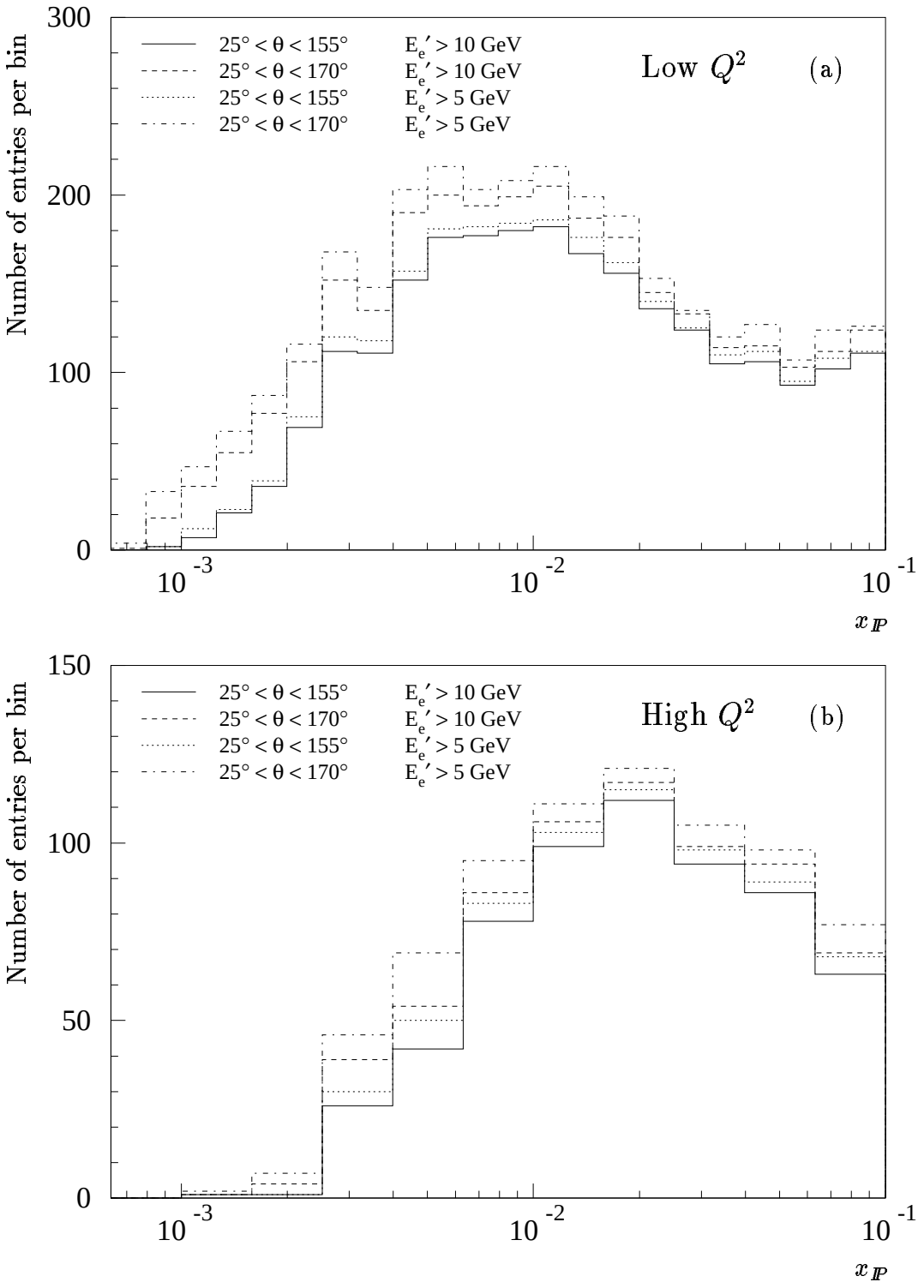

Figure 7.4: The expected number of reconstructed $D^{*\pm}$ mesons in bins of $x_{I\!P}$ in the regions (a) 10 GeV^2 $< Q^2 <$ 25 GeV^2 and (b) 50 GeV^2 $< Q^2 <$ 100 GeV^2. The continuous line shows the results with central tracking only and a requirement $E'_e > 10$ GeV. The other lines show the effect of extending tracking coverage in the backward direction and including E'_e down to 5 GeV.

7.3.2 Other Decay Channels

The D^{*+} decay to $D^0\pi^+_{slow}$ has a branching fraction of nearly 70% and is the only decay mode giving a charged track in addition to the D^0 decay products. However, the D^0 decay to $K^-\pi^+$ has a branching fraction of only $(3.83 \pm 0.12)\%$, so there is clearly room for a large improvement in statistics if other D^0 decay channels can be used.

The decay

$$D^0 \to \bar{K}^0\pi^+\pi^- \to K^0_s\pi^+\pi^- \to (\pi^+\pi^-)\pi^+\pi^-$$

can be tagged in the central tracker using the secondary vertex given by the K^0_s decay, and the final state includes only charged particles, allowing complete reconstruction of the D^0. However, the branching fraction is approximately half that of the decay chain used earlier. Compared to the method described above, this also has the disadvantage that the larger number of final-state particles (five instead of three) results in a smaller acceptance and a larger combinatorial background. This channel has, however, been used to measure the $D^{*\pm}$ production cross section in inclusive photoproduction [101], where the statistics are much greater.

There are many other D^0 decay channels with branching fractions of a few percent, but they are all significantly more difficult to use as tags of charm production with the current detector configuration. In the decay to $K^-\pi^+\pi^+\pi^-$, which has a branching fraction of $(7.5 \pm 0.5)\%$, the final state again contains only charged particles and can be completely reconstructed. However, the large multiplicity, without the helpful secondary vertex of the K^0_s channel as a signature, leads to a larger combinatorial background. The other significant hadronic decay modes are even harder to reconstruct, having π^0 mesons in the final state in addition to the charged pion and kaon tracks. About 15% of D^0 decays are semileptonic, with a neutrino in the final state, and therefore cannot be fully reconstructed.

A measurement of inclusive D^0 production has been made in DIS [25]. The results show that only about 25% of D^0 mesons produced come from D^{*+} decays, so an increase of a factor of four in statistics is possible in principle if one can dispense with the D^{*+} tagging method. However, without the kinematic constraint provided by the D^{*+} decay, there is a much larger background, and this method is not practical in diffractive DIS with the existing data.

This situation will be greatly improved by the arrival of the CST. By reconstructing the secondary vertex given by the D^0 decay, the CST will dramatically

reduce the background for the processes which are currently too difficult to use, making many more decay modes available. The CST allows the decay $D^0 \to K^-\pi^+$ to be tagged with an efficiency of about 40% [100]. If a similar efficiency can be attained for all other decay modes in which at least two charged tracks originate from the D^0 decay vertex, the expected number of tagged $D^{*\pm}$ mesons will increase from about 650 to around 6000. It may additionally be possible to measure inclusive production of the D^0 meson as well as the easier D^{*+}, resulting in a further gain in statistics.

7.4 Conclusions

Using the technique described in chapter 6, it will be possible with an integrated luminosity of $\sim 780\ pb^{-1}$ to measure the diffractive charm structure function $F_2^{D(3)c}$ with reasonable precision. The new silicon vertex detector is expected to extend the range of usable decay channels, thus increasing the acceptance for charm events by an order of magnitude. This will enable detailed investigation of diffractive deep-inelastic charm production using a significantly smaller integrated luminosity – around 100 pb^{-1}.

Chapter 8

Summary

A measurement has been made of the cross section for production of the charmed $D^{*\pm}$ meson in diffractive deep-inelastic interactions, using the decay $D^{*+} \to D^0\pi^+ \to (K^-\pi^+)\pi^+$. The result for the kinematic region 10 GeV$^2 < Q^2 <$ 100 GeV^2, $0.06 < y < 0.6$, $x_{I\!P} < 0.05$, $|t| < 1$ GeV^2, $M_Y < 1.6$ GeV, $|\eta(D^*)| < 1.25$ and $p_\perp(D^*) > 1$ GeV is

$$\sigma(e^+p \to e^+D^{*\pm}XY) = (410^{+160+150}_{-140-120})\ \text{pb}.$$

This result is significantly greater than the prediction of a model in which the pomeron is an object with a quark-based structure, and favours a significant gluon content in the pomeron. This conclusion is consistent with the results of other analyses, both of inclusive deep-inelastic diffraction and of other properties of the hadronic final state.

A Monte Carlo method has been used to demonstrate the feasibility of making more detailed studies of diffractive deep-inelastic charm production with the increased luminosity expected from HERA in the future. With an integrated luminosity of several hundred pb^{-1}, it will be possible to measure the diffractive charm structure function $F_2^{D(3)c}$. The addition of a silicon vertex detector to H1, already under way, will greatly increase the acceptance for tagging charm production, enabling a measurement of $F_2^{D(3)c}$ with an integrated luminosity of around 100 pb^{-1}.

References

[1] F. Halzen and A. D. Martin. *Quarks and Leptons.* Wiley, 1984.

[2] G. Wolf. *HERA physics.* DESY preprint 94–022 (1994).

[3] M. Gell-Mann. *A schematic model of baryons and mesons.* Phys. Lett. 8 (1964) 214–215.

[4] R. E. Taylor. *Deep inelastic scattering: The early years.* Rev. Mod. Phys. 63 (1991) 573–595.

[5] H. W. Kendall. *Deep inelastic scattering: Experiments on the proton and the observation of scaling.* Rev. Mod. Phys. 63 (1991) 597–614.

[6] J. I. Friedman. *Deep inelastic scattering: Comparisons with the quark model.* Rev. Mod. Phys. 63 (1991) 615–627.

[7] Bartel et al. *The transverse and longitudinal cross sections for electroproduction of pions near the* $\Delta(1236)$*-isobar.* Phys. Lett. B 27 (1968) 660–662.

[8] European Muon Collaboration. *A detailed study of the proton structure functions in deep inelastic muon-proton scattering.* Nucl. Phys. B 259 (1985) 189–265.

[9] European Muon Collaboration. *Measurements of the nucleon structure functions* F_2^N *in deep inelastic muon scattering from deuterium and comparison with those from hydrogen and iron.* Nucl. Phys. B 293 (1987) 740–786.

[10] BCDMS Collaboration. *A high statistics measurement of the proton structure functions* $F_2(x, Q^2)$ *and* R *from deep inelastic muon scattering at high* Q^2. Phys. Lett. B 223 (1989) 485–489.

[11] BCDMS Collaboration. *A comparison of the structure functions* F_2 *of the proton and neutron from deep inelastic muon scattering at high* Q^2. Phys. Lett. B 237 (1990) 599–604.

[12] New Muon Collaboration. *Proton and deuteron F_2 structure functions in deep inelastic muon scattering.* Phys. Lett. B 295 (1992) 159–168.

[13] T. J. Carroll. *Recent results from Fermilab experiment E665.* J. Phys. G 22 (1996) 769–773.

[14] M. Breidenbach et al. *Observed behaviour of highly inelastic electron-proton scattering.* Phys. Rev. Lett. 23 (1969) 935–939.

[15] J. D. Bjorken. *Asymptotic sum rules at infinite momentum.* Phys. Rev. 179 (1969) 1547–1553.

[16] J. D. Bjorken and E. A. Paschos. *Inelastic electron-proton and γ-proton scattering and the structure of the nucleon.* Phys. Rev. 185 (1969) 1975–1982.

[17] R. P. Feynman. *Photon-Hadron Interactions.* Benjamin, 1972.

[18] G. Altarelli and G. Parisi. *Asymptotic freedom in parton language.* Nucl. Phys. B 126 (1977) 298–318.

[19] Yu. L. Dokshitser. *Calculation of structure functions of deep-inelastic scattering and e^+e^- annihilation by perturbation theory in quantum chromodynamics.* Sov. Phys. JETP 46 (1977) 641–653.

[20] V. N. Gribov and L. N. Lipatov. Sov. J. Nucl. Phys. 15 (1972) 438, 675.

[21] H1 Collaboration. *A measurement and QCD analysis of the proton structure function $F_2(x, Q^2)$ at HERA.* Nucl. Phys. B 470 (1996) 3–38.

[22] H1 Collaboration. *Measurement of the Q^2 dependence of the charged and neutral current cross sections in $e^{\pm}p$ scattering at HERA.* Phys. Lett. B 379 (1996) 319–329.

[23] A. H. Mueller. *Parton distributions at very small x-values.* Nucl. Phys. B (Proc. Suppl.) 18C (1990) 125–132.

[24] H1 Collaboration. *Energy flow and charged particle spectra in deep inelastic scattering at HERA.* Z. Phys. C 63 (1994) 377–389.

[25] H1 Collaboration. *Inclusive D^0 and $D^{*\pm}$ production in deep inelastic ep scattering at HERA.* Z. Phys. C 72 (1996) 593–605.

[26] C. Weizsäcker. Z. Phys. 88 (1934) 612.

[27] E. Williams. Phys. Rev. 45 (1934) 729.

[28] J. J. Sakurai. Ann. Phys. 11 (1960) 1.

[29] J. J. Sakurai and D. Schildknecht. *Generalized vector dominance and inelastic electron-proton scattering.* Phys. Lett. B 40 (1972) 121–126.

[30] M. Greco. *Deep-inelastic processes.* Nucl. Phys. B 63 (1973) 398–412.

[31] H1 Collaboration. *Inclusive parton cross sections in photoproduction and photon structure.* Nucl. Phys. B 445 (1995) 195–215.

[32] S. J. Maxfield. *Some aspects of photoproduction at HERA.* J. Phys. G 22 (1996) 787–796.

[33] ZEUS Collaboration. *Measurement of total and partial photon proton cross sections at 180 GeV center of mass energy.* Z. Phys. C 63 (1994) 391–408.

[34] H1 Collaboration. *Observation of hard processes in rapidity gap events in γp interactions at HERA.* Nucl. Phys. B 435 (1995) 3–20.

[35] ZEUS Collaboration. *Observation of hard scattering in photoproduction events with a large rapidity gap at HERA.* Phys. Lett. B 346 (1995) 399–414.

[36] H1 Collaboration. *Diffractive dissociation in photoproduction at HERA.* Z. Phys. C 74 (1997) 221–235.

[37] ZEUS Collaboration. *Observation of events with a large rapidity gap in deep inelastic scattering at HERA.* Phys. Lett. B 315 (1993) 481–493.

[38] H1 Collaboration. *Deep inelastic scattering events with a large rapidity gap at HERA.* Nucl. Phys. B 429 (1994) 477–502.

[39] P. D. B. Collins and A. D. Martin. *Hadron Interactions.* Adam Hilger Ltd, 1984.

[40] P. D. B. Collins. *An Introduction to Regge Theory and High Energy Physics.* Cambridge University Press, 1977.

[41] G. F. Chew, S. C. Frautschi, and S. Mandelstam. *Regge poles in π-π scattering.* Phys. Rev. 126 (1962) 1202–1208.

[42] J. P. Burq et al. *Experimental results on pp forward elastic scattering and the possibility of universal shrinkage of the hadronic diffraction cone.* Phys. Lett. B 109 (1982) 124–128.

[43] I. I. Pomeranchuk. *Equality of the nucleon and antinucleon total interaction cross section at high energies.* Sov. Phys. JETP 7 (1958) 499–501.

[44] A. Donnachie and P. V. Landshoff. *Total cross sections.* Phys. Lett. B 296 (1992) 227–232.

[45] R608 Collaboration. *Evidence for pomeron single-quark interactions in proton diffraction at the ISR.* Phys. Lett. B 163 (1985) 267–272.

[46] R608 Collaboration. *Further evidence for pomeron-quark interactions: observation of large Λ^0 polarization in $pp \to (\Lambda^0 K^+)p$.* Phys. Lett. B 283 (1992) 155–160.

[47] WA91 Collaboration. *Observation of a narrow scalar meson at 1450 MeV in the reaction $pp \to p_f(\pi^+\pi^-\pi^+\pi^-)p_s$ using the CERN Omega Spectrometer.* Phys. Lett. B 324 (1994) 509–514.

[48] WA102 Collaboration. *A kinematical selection of glueball candidates in central production.* Phys. Lett B 397 (1997) 339–344.

[49] G. Ingelman and P. Schlein. *Jet structure in high mass diffractive scattering.* Phys. Lett. B 152 (1985) 256–260.

[50] UA8 Collaboration. *Evidence for transverse jets in high-mass diffraction.* Phys. Lett. B 211 (1988) 239–246.

[51] UA8 Collaboration. *Evidence for a super-hard pomeron structure.* Phys. Lett. B 297 (1992) 417–424.

[52] ZEUS Collaboration. *Measurement of the cross section for the reaction $\gamma p \to J/\psi p$ with the ZEUS detector at HERA.* Phys. Lett. B 350 (1995) 120–134.

[53] H1 Collaboration. *Elastic and inelastic photoproduction of J/ψ mesons at HERA.* Nucl. Phys. B 472 (1996) 3–31.

[54] H1 Collaboration. *Measurement of the total photon proton cross section and its decomposition at 200 GeV centre of mass energy.* Z. Phys. C 69 (1995) 27–38.

[55] H1 Collaboration. *First measurement of the deep-inelastic structure of proton diffraction.* Phys. Lett. B 348 (1995) 681–696.

[56] H1 Collaboration. *A measurement and QCD analysis of the diffractive structure function $F_2^{D(3)}$.* Paper pa02–061 contributed to the 28th International Conference on High Energy Physics, Warsaw, Poland, July 1996.

[57] ZEUS Collaboration. *Exclusive ρ^0 production in deep inelastic electron-proton scattering at HERA.* Phys. Lett. B 356 (1995) 601–616.

[58] H1 Collaboration. *Elastic electroproduction of ρ and J/ψ mesons at large Q^2 at HERA.* Nucl. Phys. B 468 (1996) 3–33.

[59] A. Donnachie and P. V. Landshoff. *Diffractive deep inelastic lepton scattering.* Phys. Lett. B 191 (1987) 309–312.

[60] T. Gehrmann and W. J. Stirling. *Deep inelastic electron-pomeron scattering at HERA.* Z. Phys. C 70 (1996) 89–102.

[61] B. A. Kniehl, H.-G. Kohrs, and G. Kramer. *Diffractive photoproduction of jets with a direct pomeron coupling at HERA.* Z. Phys. C 65 (1995) 657–666.

[62] F. E. Low. *Model of the bare Pomeron.* Phys. Rev. D 12 (1975) 163–173.

[63] S. Nussinov. *Perturbative recipe for quark-gluon theories and some of its applications.* Phys. Rev. D 14 (1976) 246–257.

[64] N. N. Nikolaev and B. G. Zakharov. *Pomeron structure function and diffraction dissociation of virtual photons in perturbative QCD.* Z. Phys. C 53 (1992) 331–345.

[65] E. A. Kuraev, L. N. Lipatov, and V. S. Fadin. *Multiregge processes in the Yang-Mills theory.* Sov. Phys. JETP 44 (1976) 443–451.

[66] Y. Y. Balitskiĭ and L. N. Lipatov. *The Pomeranchuk singularity in quantum chromodynamics.* Sov. J. Nucl. Phys. 28 (1978) 822–829.

[67] W. Buchmüller and A. Hebecker. *A parton model for diffractive processes in deep inelastic scattering.* Phys. Lett. B 355 (1995) 573–578.

[68] A. Edin, J. Rathsman, and G. Ingelman. *Soft colour interactions and the diffractive structure function.* J. Phys. G 22 (1996) 943–946.

[69] A. Edin, G. Ingelman, and J. Rathsman. *Unified description of rapidity gaps and energy flows in DIS final states.* DESY preprint 96–060 (1996).

[70] G. Ingelman, A. Edin, and J. Rathsman. *LEPTO 6.5 — A Monte Carlo generator for deep inelastic lepton-nucleon scattering.* Comp. Phys. Comm. 101 (1997) 108–134. See also WWW page at `<http://www3.tsl.uu.se/thep/lepto/>`.

[71] M. Düren and K. Rith. *Polarized electron nucleon scattering at HERA: The HERMES experiment.* In Proc. of the Workshop *Physics at HERA*, Hamburg, Germany, 1991. Volume 1.

[72] H1 Collaboration. *The H1 detector at HERA.* Nucl. Instr. and Meth. A 386 (1997) 310–347.

[73] H1 Collaboration. *The tracking, calorimeter and muon detectors of the H1 experiment at HERA.* Nucl. Instr. and Meth. A 386 (1997) 348–396.

[74] J. Bán et al. *The H1 backward calorimeter BEMC and its inclusive electron trigger.* Nucl. Instr. and Meth. A 372 (1996) 399–414.

[75] J. Heatherington et al. *Analysis of FToF TDC data.* H1 internal report H1 06/94-362.

[76] R. Prosi. *The 1994 L4 filter farm selection algorithm.* H1 internal report H1 03/95-433.

[77] *GEANT Detector Description and Simulation Tool.* CERN Program Library Long Writeup W5013, 1993.

[78] U. Bassler and G. Bernardi. *On the kinematic reconstruction of deep inelastic scattering at HERA: the* Σ *method.* Nucl. Instr. and Meth. A 361 (95) 197–208.

[79] H. Jung. *Hard diffractive scattering in high energy ep collisions and the Monte Carlo Generator RAPGAP.* Comp. Phys. Comm. 86 (1995) 147–161.

[80] A. Mehta. *Measurement of the Diffractive Proton Structure Function and Calibration of the Forward Muon Detector at H1.* PhD thesis, University of Manchester, 1994.

[81] G. J. Feldman et al. *Observation of the decay* $D^{*+} \to D^0\pi^+$. Phys. Rev. Lett. 38 (1977) 1313–1315.

[82] G. Ingelman, J. Rathsman, and G. A. Schuler. *AROMA 2.2 – A Monte Carlo generator for heavy flavour events in ep collisions.* Comp. Phys. Comm. 101 (1997) 135–142.

[83] F. James. *MINUIT: Function Minimization and Error Analysis.* CERN Program Library Long Writeup D506, 1994.

[84] H1 Collaboration. *Photoproduction of* $D^{*\pm}$ *mesons in electron-proton collisions at HERA.* Nucl. Phys. B 472 (1996) 32–51.

[85] W. Erdmann. *Untersuchung der Photoproduktion von D^*-Mesonen am ep-Speicherring HERA.* PhD thesis, ETH Zürich, 1996.

[86] T. Eckel. *Untersuchungen der Nachweiswahrscheinlichkeiten und Meßgenauigkeiten von Teilchenspuren in der zentralen Spurenkammer von H1.* Diploma thesis, Universität Hamburg, 1994.

[87] A. Mehta. Private communication.

[88] B. List. *Diffraktive J/ψ-Produktion in Elektron-Proton-Stössen am Speicherring HERA.* Diploma thesis, Technische Universität Berlin, 1993.

[89] A. Mehta. Private communication.

[90] R. Engel. In Proc. of the XXIXth Rencontre de Moriond, France, 1994. Page 321.

[91] Particle Data Group (R. M. Barnett et al.). *Review of Particle Properties.* Phys. Rev. D54 1 (1996).

[92] J. Phillips. Private communication.

[93] M. Genovese, N. N. Nikolaev, and B. G. Zakharov. *Excitation of open charm and factorization breaking in rapidity gap events at HERA.* Phys. Lett. B 378 (1996) 347–353.

[94] M. F. McDermott and G. Briskin. *Diffractive structure functions in DIS.* In Proc. of the Workshop *Future Physics at HERA*, Hamburg, Germany, 1996.

[95] A. Mehta, J. Phillips, and B. Waugh. *Future diffractive structure function measurements at HERA.* In Proc. of the Workshop *Future Physics at HERA*, Hamburg, Germany, 1996.

[96] J. Bürger et al. *Technical proposal to build silicon tracking detectors for H1.* H1 internal report H1 06/92-226. and DESY PRC 92/01.

[97] H1 SPACAL Group. *The H1 lead/scintillating-fibre calorimeter.* Nucl. Instr. and Meth. A 386 (1997) 397–408.

[98] W. Bartel et al. *HERA luminosity upgrade.* In Proc. of the Workshop *Future Physics at HERA*, Hamburg, Germany, 1996.

[99] H1 Collaboration. *H1 in a high luminosity interaction region at HERA.* H1 internal report.

[100] S. Egli. *Rare charm decays at HERA.* In Proc. of the Third Topical Seminar on Heavy Flavours, San Miniato, Italy, 1991.

[101] R. Bernet. *Production of $D^{*\pm}$ Mesons Measured with the H1 Detector at HERA.* PhD thesis, ETH Zürich, 1995.

Acknowledgments

Firstly, I would like to thank my supervisor, Mike Ibbotson, for providing advice and guidance while leaving me free to choose my own direction. I would also like to thank the following people for their invaluable assistance: Chris Hilton and Phill Biddulph, who showed me the ropes when I arrived at DESY and whose expertise has been indispensable; Andrew Mehta, who constructively criticized several chapters of this thesis; the rest of the diffractive working group, especially Julian Phillips, John Dainton and Hannes Jung; the heavy-flavour working group, especially Karin Daum. Thanks too to Paul Sutton, not least for persuading me to go to German lessons at the Linguothek, and to Jane Bromley, Martin Utley, Molly Anderson and the rest of the gang who helped to make those two years in Hamburg such an enjoyable experience. Finally, many thanks to my mother, father and sister for their love, support and encouragement.